Ultra-miniature long-wavelength infrared Fourier spectroscopy with high sensitivity and wavelength resolution for on-site component identification

Natsumi KAWASHIMA

January 2021
ISHIMARU Laboratory
Graduate School of Engineering, Kagawa University

Abstract

We aim to realize a society in which the passing of daily data contributes to solving social issues, such as achieving Sustainable Development Goals, by establishing highly sensitive and ultra-miniature spectroscopic systems mounted on wearable terminals. Presently, we obtain component data and identify a component using expensive and large equipment at laboratories and specialized institutions after samples are picked up on site. However, if a small and low-cost sensor that measures and identifies components of samples becomes common, the public can obtain component information on site and specialists can receive on-site information from them. An on-site temporal monitoring system of component information would thus be realized. Presently, small sensors mounted on wearable terminals can detect acceleration and illuminance but few other components. Attempts have been made to miniaturize spectroscopic imagers in the visible wavelength region and mount them on smartphones. However, infrared spectroscopic imagers that are appropriate to component analysis have not yet been mounted on smartphones. I establish the wide-field-stop and beam-expansion method, superimposing interferogram method, and point-one-shot Fourier spectroscopy to improve the detected light intensity, the interference definition, and the wavelength resolution of spatial-phase-shift interferometers that can be used as small infrared spectrometers mounted on wearable terminals. Point-one-shot Fourier spectroscopy, which uses only one lens and a camera and one spatial-phase-shift interferometer, detects two-dimensional fringe patterns using point-area information and thus achieves high wavelength resolution using a low-cost low-pixel camera. Conventionally, the sensitivity that is combined using the detected light intensity and interference definition of spatial-phase-shift interferometers is lacking because a field stop is inserted in the optical system and the wavelength resolution and sensitivity of interferometers have a trade-off relationship. However, by combining my three proposed methods, we realize ultra-miniature long-wavelength infrared Fourier spectroscopic imagers that have high sensitivity and wavelength resolution for on-site component identification.

Table of Contents

CHAPTER 1

General introduction

CHAPTER 2

Wide-field-stop and beam-expansion method to enhance the detected light intensity of spatial-phase-shift interferometers

CHAPTER 3

Superimposing interferogram method using a multi-slit array to enhance sensitivity and interference definition of spatial-phase-shift interferometers

CHAPTER 4

Point-one-shot Fourier spectroscopy for improved wavelength resolution, price reduction, and miniaturization

CHAPTER 1

Introduction

1.1 Background

In recent years, Internet of Things (IoT) technology that enables automatic recognition, automatic control, and remote measurement through the transmission, via the Internet, of information obtained from sensors has received attention globally. As examples, automated driving for the prevention of accidents, caregiving aid in hospitals and the home, and crop-spraying can be realized when automobiles, robots, and drones have small sensors and the ability to communicate via the Internet. These days, almost all people have a smartphone or smartwatch that connects to the Internet, and there is thus global research on the value of mounting small sensors on such devices.

Presently, small sensors mounted on wearable terminals can detect the Global Positioning System, magnetism, acceleration, orientation and angular velocity, ambient light, proximity, and fingerprints. In terms of health monitoring in daily-life environments, sensors are limited to heart rate monitors and pedometers and do not measure biomedical components (e.g., blood glucose and lactic acid). The development of small sensors that measure biomedical components would allow non-invasive health monitoring [1-8] at home and support case detection and the prevention of disease. Wearable terminals would thus be worthy healthcare sensors that detect biomedical components.

Spectroscopy can be adopted for the measurement and identification of a biomedical component from samples. As an example, attempts have been made to miniaturize a spectroscope operating in the visible-light region and incorporate it into a smartphone for color measurement and color monitoring [9]. However, no spectroscopic imaging apparatus in the infrared region, particularly in the long-wavelength infrared region suitable for component analysis, has been installed or put into practical use. Conventional long-wavelength infrared spectrometers are large and expensive and thus owned only by specialized institutions and facilities. Therefore, conventional component measurement is performed in the laboratory after collecting samples on site. As an example, when we measure the concentration of microplastics, which is a form of marine pollution, samples are collected and monitored only at dozens of specific measurement points. Therefore, the concentration of microplastics cannot be estimated and monitored nationwide through the concentration mapping of microplastics. However, the development of a small long-wavelength infrared spectroscope that can be mounted on a wearable terminal would allow the continuous measurement of the concentration of microplastics by fishing boats owned by individuals and the attachment of a small spectroscope to the bottom of a ship. It would then be possible to create a concentration map for the navigable sea area.

Thus, by establishing a small long-wavelength infrared spectrometer as a component sensor that can be mounted on wearable terminals, casual daily life data will contribute to social issues such as achieving Sustainable Development Goals. Furthermore, the realization of an on-site temporal monitoring system of component information will create a new academic field.

1.2 History and development of spectroscopy

As shown in Figure 1, the origin of spectroscopy is said to have begun in 1666 with Isaac Newton’s discovery of the spectral decomposition of sunlight using a prism. In his experiment, Newton discovered that light comprises various types of light from blue to red and established the concept of spectroscopy. It was in 1800 that Friedrich Wilhelm Herschel [10-13] discovered infrared rays at a wavelength longer than the visible-light region. The advent of diffraction gratings dramatically improved the performance of spectroscopic measurements. In 1814, Joseph von Fraunhofer created a diffraction grating with a structure similar to that currently in use and manufactured the first spectrometer in which the prism was replaced with a diffraction grating. He created a high-resolution grating spectrometer and found 570 dark areas in the spectrum of sunlight. These dark areas are called Fraunhofer lines and were later shown by Gustav Robert Kirchhoff and Robert Wilhelm Bunsen to be due to the molecular and atomic-specific absorption of constituents of the sun's surface layer, which became the basis of spectroscopy. André-Marie Ampère confirmed that the heat ray discovered by Herschel was the same ray as visible light and was only an extension of visible light on the long wavelength side, and he named this heat ray infrared in 1835. It was James Clerk Maxwell who theoretically revealed in 1864 that visible and infrared waves are both electromagnetic waves, and Heinrich Rudolf Hertz experimentally proved this in 1888. At the same time, spectral measurements in the visible, near infrared, and infrared regions commenced adopting, for example, photographic plates, and Samuel Langley invented a bolometer (a device that detects the energy of electromagnetic waves) in 1878. It then became possible to measure radiant energy with a device instead of a photographic plate, and the measurement of the molecular spectrum expanded dramatically. The measurement of infrared spectra was the first measurement of molecular spectra that became popular in the 20th century, and infrared spectrum charts were created at the beginning of the 20th century. Max Karl Ernst Ludwig

Planck described the spectral density of electromagnetic radiation emitted by a black body in 1901. In 1903, a pioneering study conducted by William Weber Coblentz showed that organic compounds with certain functional groups have infrared absorption spectra in almost certain wavelength regions. The basis of the absorption spectrum has been established. However, its use in analytical chemistry is untapped, and until the 1940s, infrared absorption spectra were studied by only a small number of researchers in the field of theoretical physical chemistry.

In 1930, the technical development of a (dispersion-type) infrared spectrophotometer [14-16] was successfully carried out in the United States, and the basis of infrared absorption spectrum analysis was established. Until this time, spectroscopy used only incoherent light from a spontaneous emission as a light source, but with the invention of the laser in the mid-20th century, modern spectroscopic research began.

Incidentally, the Michelson interferometer was invented by Albert Michelson in the 1880s. It is widely used in the field of modern infrared spectroscopy. However, because it requires a difficult numerical process called the Fourier transform, the practical use of the Fourier transform infrared (FTIR) spectrometer was delayed until the computer became available. The FTIR spectrometer has thus been used since the 1970s [17,18]. Although the FTIR spectrometer can measure with higher sensitivity (brightness) and resolution than the dispersive spectrometer, it is large and expensive even in modern times owing to its vulnerability to mechanical vibration, and only specialized facilities own one. On-site component monitoring is not possible. However, the research results of this paper allow the development of a small and low-cost infrared Fourier spectroscopic imager with high sensitivity and wavelength resolution that can be mounted on a wearable terminal and can be owned by the general public.

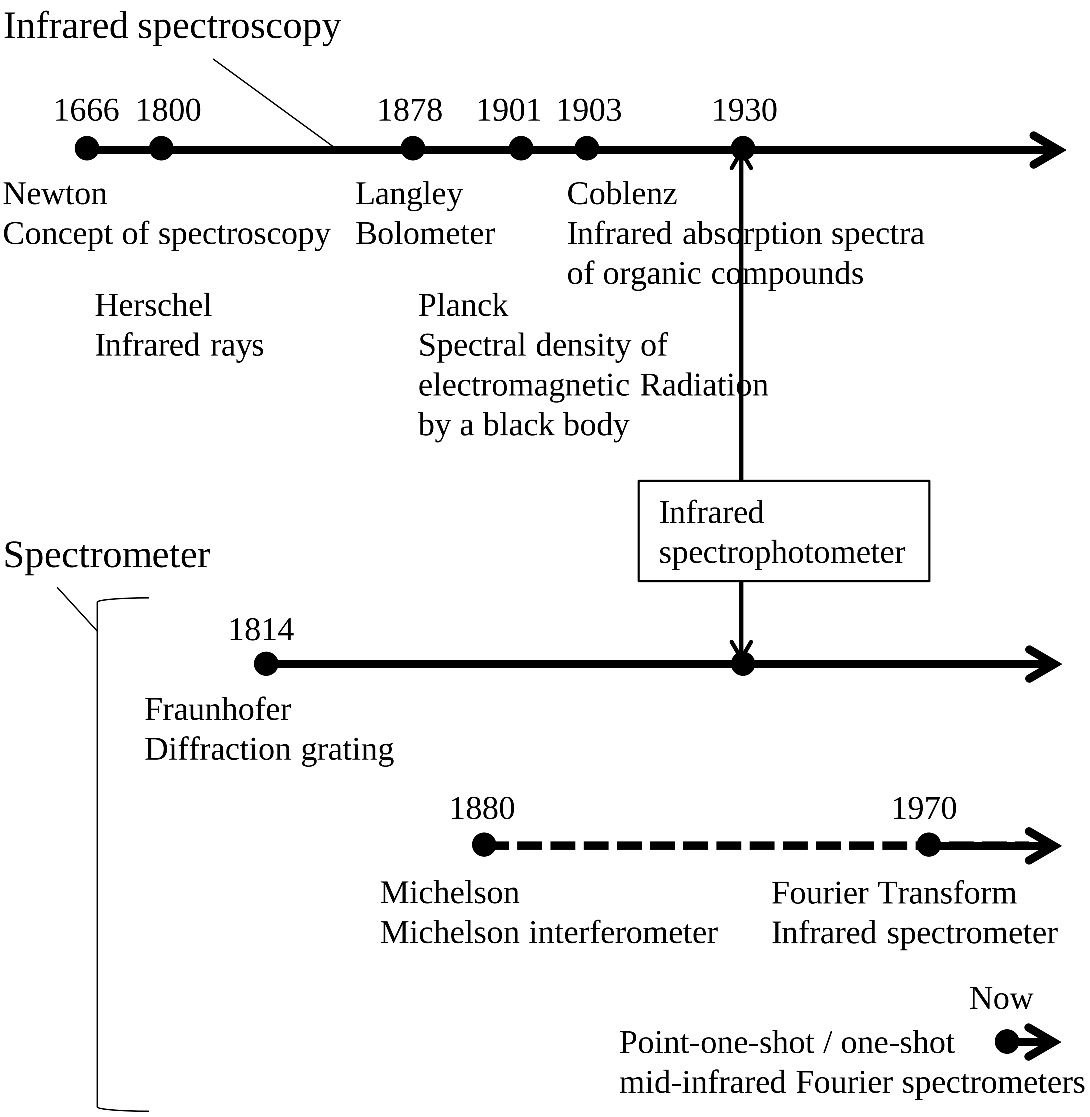

Figure 1 History of infrared spectroscopy and the spectrometer

1.3 Introduction of the conventional method

1.3.1 Wavelength-dispersive spectrometer

Wavelength-dispersive spectroscopy [19-29] is a method in which light having traveled through a measurement object is dispersed for each wavelength using a diffraction grating or prism, and the spectrum is obtained from the intensity. As shown in Fig. 2, light emitted from the light source passes through the sample and then through the diffraction grating or prism. At that time, the light is dispersed because the light is separated under the effect of the refractive index and the diffraction angle that differ for each wavelength. This dispersed light is acquired by a detector, and the spectral characteristics are acquired from the intensity of each wavelength. A white-light source in the visible-light region is a sum of multiple waves, and the refractive index is different at each wavelength. Therefore, when the white-light source is applied to the diffraction grating or prism, the light is dispersed for each wavelength.

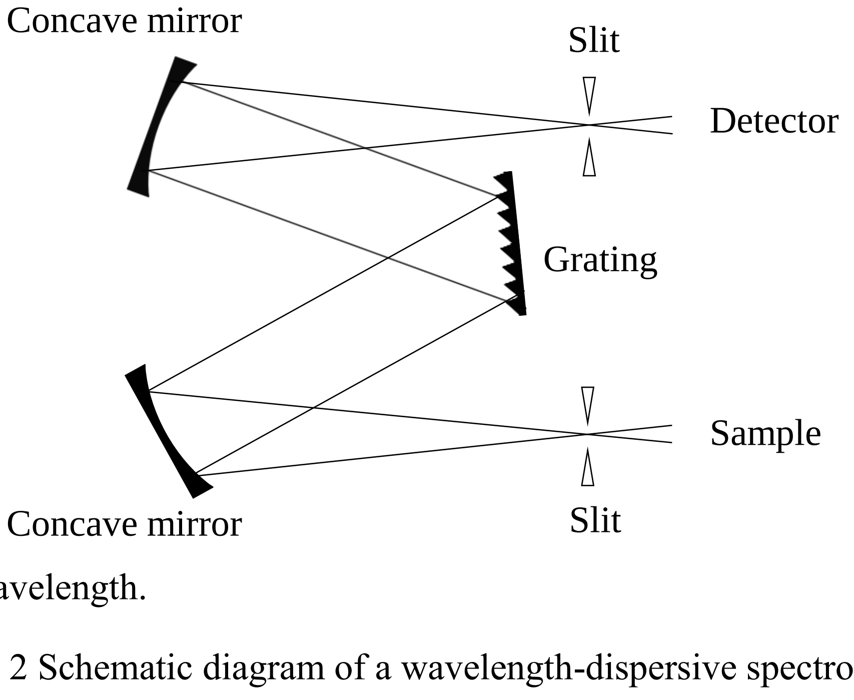

Figure 2 Schematic diagram of a wavelength-dispersive spectrometer

1.3.2 FTIR spectrometer (Michelson interferometer)

An FTIR spectrometer [30-36], which is well known as a component analyzer, is adopted in FTIR spectroscopy. The spectral characteristics are analytically determined by the Fourier transform at the same time as using a Michelson interferometer, instead of separating each wavelength using wavelength-dependent diffraction angles and refraction angles as in wavelength-dispersive spectroscopy. The signal utilization efficiency is high because light from a light source or sample with a large area and wide radiation angle can be used efficiently, and all wavelengths can be detected at the same time. In addition, it is possible to make a measurement with high-wavenumber accuracy and high resolution.

Figure 3 is a schematic diagram of the Michelson interferometer. The group of light rays emitted from the light source is collimated by the objective lens and falls incident on the beam splitter. The incident light is split into two objective beams, which are reflected light and transmitted light, by the beam splitter, and the reflected light is incident on the fixed mirror side and the transmitted light is incident on the movable mirror side. At that time, a change in interference intensity depending on the difference between the separation of the fixed mirror and beam splitter and the separation of the movable mirror and beam splitter is confirmed on the observation surface. The difference in separation at this time is called the optical path length difference. The light source contains components of various wavelengths, and it is thus possible to measure the interferogram, which is the sum of all wavelengths on the observation surface. Fourier transform spectroscopy is a method of obtaining spectral characteristics through the Fourier transformation of this interferogram.

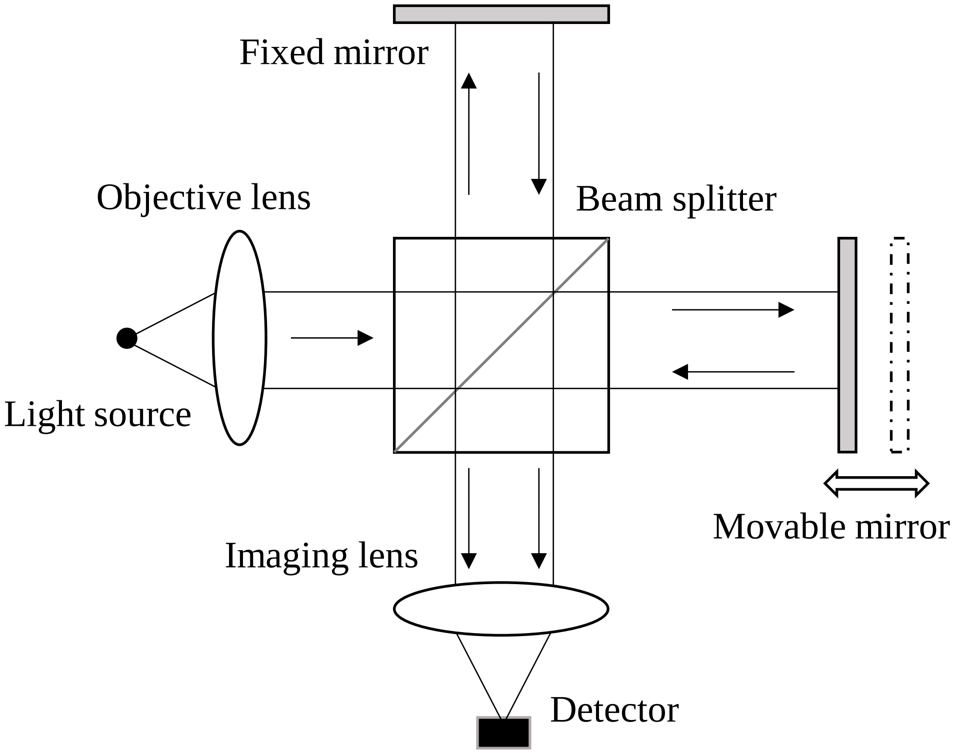

Figure 3 Schematic diagram of the Michelson interferometer

1.3.3 Attenuated Total Reflectance (ATR)

Owing to the extremely large absorption of long-wavelength infrared light by moisture, it is difficult to detect transmitted light unless the liquid sample (moisture: 100%) is made into a thin film (optical path length: thickness ≤ 100 μm). Conventionally, when applying long-wavelength infrared spectroscopy to a biological sample, the ATR method [37,38] has been used.

As shown in Fig. 4, the absorption spectrum of the sample surface layer is obtained by bringing the sample into close contact with a medium having a high refractive index (i.e., prism) that is transparent in the infrared region and measuring the total reflected light from the prism that slightly penetrated the sample and reflected. At this time, the infrared light penetrates into a relatively deep region of several microns from the sample surface, and the depth of penetration depends on the wavelength (λ) and incident angle (θ) of the infrared light in the air and the refractive index n_1 of the prism and refractive index n_2 of the sample.

The depth of penetration d_p is defined as the distance at which the light intensity becomes $\frac{1}{e}$ the intensity on the surface. To adjust the depth of penetration, the angle of incident light should be changed or prisms with different refractive indexes should be used. As an example, in making the depth of penetration shallower, the angle of incidence is increased and a prism with a large refractive index is used. In addition, the depth of penetration depends on the wavelength, and the absorption intensity of the ATR spectrum increases toward the longer wavelength side (i.e., lower wavenumber side). Therefore, the baseline of the ATR spectrum tends to fall to the right, but the ATR spectrum can be corrected using the reciprocal of the wavelength ($\frac{1}{\lambda}$) to a spectrum with a peak intensity ratio similar to that of the transmission spectrum.

However, when adopting the ATR method, it is difficult for light to reach the dermis layer containing blood glucose because the evanescent exudation (i.e., the depth of penetration into the sample) on the prism surface was at most 10 µm.

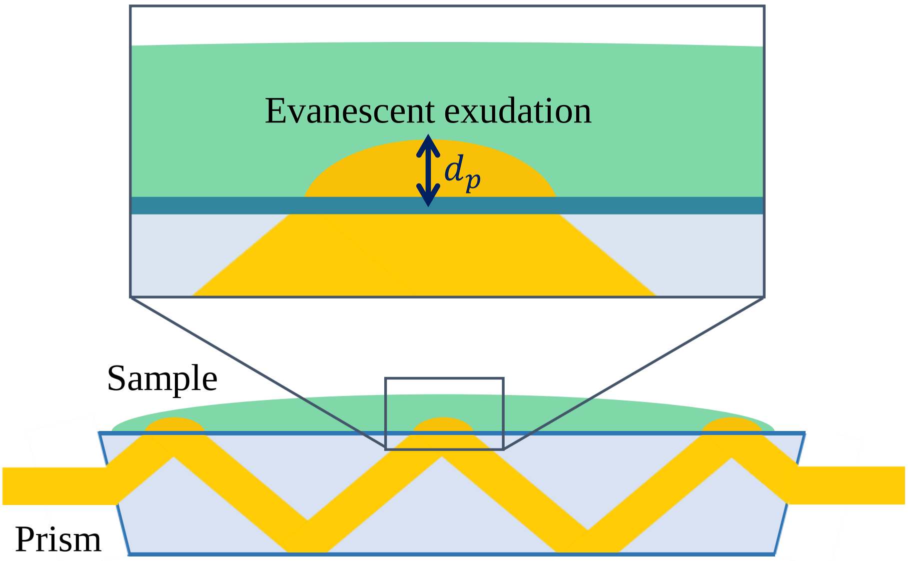

Figure 4 Schematic diagram of ATR

1.4 Introduction of the proposed method

1.4.1 Imaging-type two-dimensional (2D) Fourier spectroscopy

Figure 5 illustrates the principle of the proposed method [39-41]. The figure shows the ordinary imaging optics. From an optical point of view, the surface of the object is covered by many bright points. From a single bright point, rays are emitted in multiple directions. These emitted rays are collimated by an objective lens and are concentrated into a single bright point on the imaging plane by the imaging lens. Therefore, the substantial bright point on the focal plane is optically formed as the conjugate bright-point image. We introduce new optics that we call the variable-phase filter. This variable-phase filter provides an arbitrary phase difference to the half flux of objective rays. This allows a phase-shift interferometer to be placed between object beams without a reference beam. In the initial state, the phases of the object rays are the same. These object rays interfere and form a bright point as the interference figure as for the ordinary imaging optics. If a half-wavelength phase difference is applied to the lower rays, the intensity of interfering light decreases. If a single-wavelength phase difference is generated, the two beams strengthen each other and form a bright point as in the case of no phase difference. In this way, if the phase is shifted sequentially, the imaging intensity changes periodically with the phase shift. As the graph shows, if monochromatic light is used as the light source, the changes in imaging intensity form a simple cyclic cosine wave. However, polychromatic light is used for spectroscopy. In the case of a long wavelength, the cycle of this imaging intensity has low frequency. If the wavelength is short, the imaging intensity changes at high frequency. On the imaging plane, the sum of these cyclic imaging intensity changes of multiple wavelengths is detected using a charge-coupled device camera. The result is called an interferogram in the field of Fourier spectroscopy. As previously stated, this interferogram is formed of multiple cyclic sine waves. Therefore, spectral characteristics can be obtained analytically by adopting a mathematical Fourier transform, such as the fast Fourier transform. In this method, rays that out of focus do not contribute to the interferogram. The initial phases of rays are different and the proposed imaging-type 2D Fourier spectroscopy thus limits the depth into the focal plane. We acquire three-dimensional spectral characteristics by scanning the focal plane mechanically in the depth direction.

Figure 6 is a configuration diagram of imaging-type 2D Fourier spectroscopy. For ease of explanation, the previous conceptual diagram is drawn as the transparent optical system. As the real optical system, the variable-phase filter is configured with a movable mirror and fixed mirror as reflective optics. This variable-phase filter is installed at an angle of 45 degrees on the optical Fourier transform plane. The phase difference is given to the half flux of the objective rays.

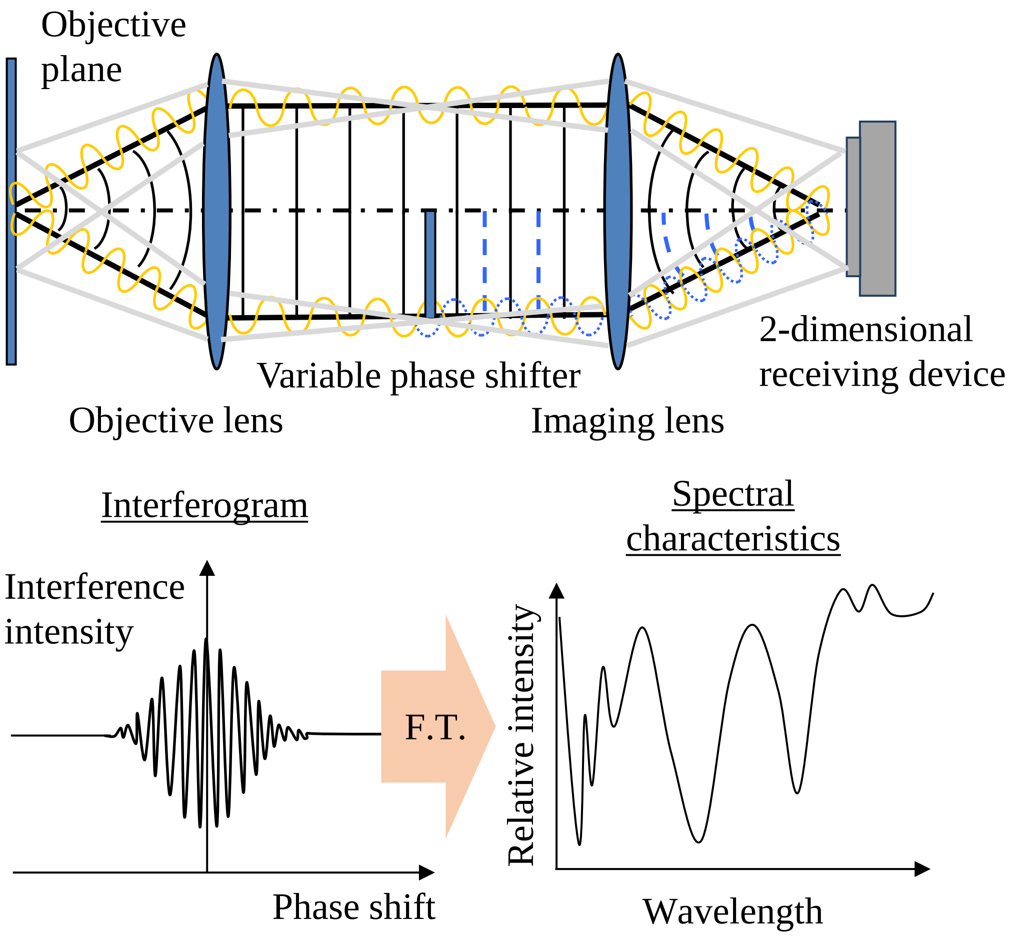

Figure 5 Schematic diagram of imaging-type Fourier spectroscopy

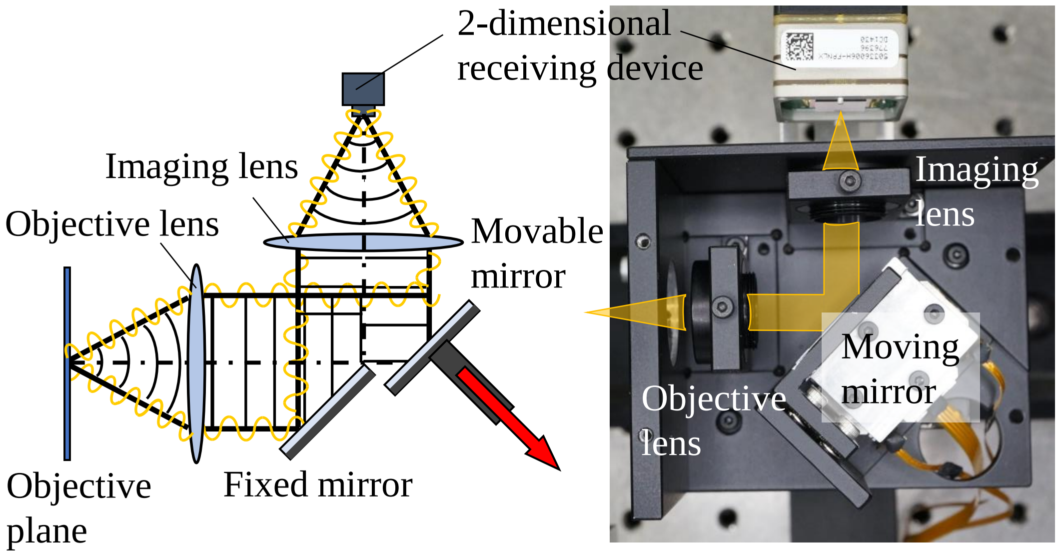

Figure 6 Configuration diagram of imaging-type 2D Fourier spectroscopy

1.4.2 One-shot Fourier spectroscopy

The proposed one-shot Fourier spectroscopy [42] obtains the one-dimensional spectroscopic image from one-frame data using a transmission-type relative-inclined phase-shifter without a mechanical phase-shift operation. The transmission-type relative-inclined phase-shifter, which provides a continuous spatial phase difference between objective beams, is configured with a glass wedge and glass cuboid. As shown in Fig. 7, the horizontal axis on the imaging device is assigned to the phase shift value. The vertical axis is assigned to the image formation line. Distributions of light intensity at each pixel on a horizontal line thus form an interferogram. Spectral characteristics can be obtained analytically adopting a mathematical Fourier transform, such as the fast Fourier transform. The two beams transmitted through the glass cuboid and wedge interfere on the imaging device from a relatively inclined angle. The coordinate value in the horizontal direction of the light-receiving device corresponds to the temporal phase shift. In addition, the proposed method can realize a one-dimensional spectroscopic measurement because interferograms can be obtained simultaneously at each line on the light-receiving device.

We then attempt to improve the time resolution with the spatial phase shift method. We refer to this technology as one-shot spectroscopic imaging. In this method, the relative inclination phase shifter is installed at the optical Fourier transform plane. Therefore, the phase-shift value is spatially different at each reflecting point. In this method, the horizontal line on the imaging plane is assigned for the phase-shift value. The intensity at each pixel is thus determined as the interfered intensity in accordance with the phase shift. The intensity distribution at each horizontal line, the interference fringe, corresponds to the interferogram. The spectrum is calculated from the interference fringe. We cannot measure the 2D spectrum using this method. As shown by the blue line in the figure, the image is formed on a line using the cylindrical imaging lens. We can thus conduct line spectral imaging.

If the wedge prism is made from thin glass (with thickness around 0.3 mm) and inserted into a smartphone’s imaging optics, a bean-sized line-spectroscopic imager can be realized. The proposed method obtains the spectroscopic line-tomography as fringe patterns from minute optical path differences of relative-inclined beams. Ultra-compact spectroscopic tomography is thus realized. Conventional wavelength-dispersive spectrometers need a long optical path to secure wavelength resolutions and cannot specify the measuring depth.

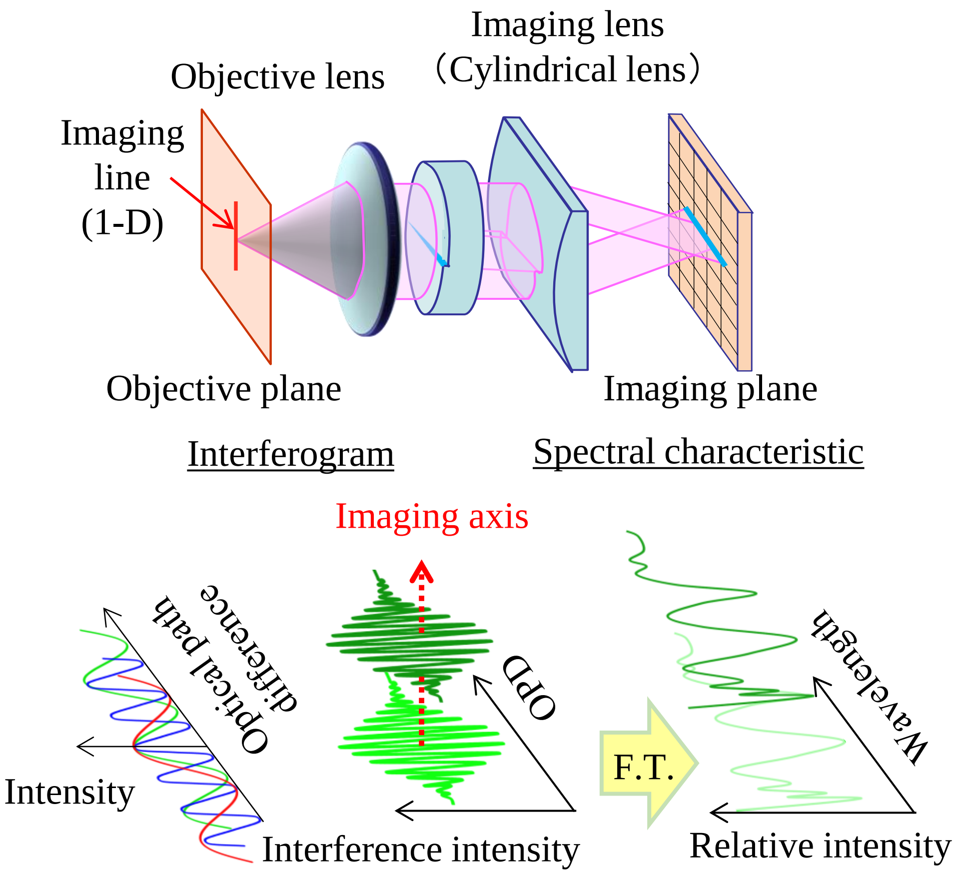

Figure 7 Schematic diagram of one-shot Fourier spectroscopy

1.4.3 Ultrasonically assisted liquid cell and parametric standing wave

The ultrasonic standing wave can generate refractive index boundaries inside samples. If the interior of a sample is homogeneous, incident light is reflected only from the sample surface because the ultrasonic standing wave is a longitudinal wave. The ultrasonic standing wave is equivalent to a compressional wave, and a periodic refractive index distribution thus forms inside uniform samples. Incident light is reflected from nodes of the ultrasonic standing wave [43-48].

If the interior of an agar sample is homogeneous, then incident light is only reflected from the sample surface. However, because the ultrasonic standing wave is equivalent to a compressional wave, a periodic refractive index distribution forms inside the agar. Incident light is then reflected from the nodes of the ultrasonic standing wave. If a shallow reflection plane is generated near the bio-membrane surface at a depth of less than 100 μm, the ultrasonic frequency used must be more than 10 MHz. However, results obtained using an ultrasonograph reveal that higher frequencies suffer from heavy damping. We therefore subjected agar samples (with thickness of 3 mm) to vibrations generated using an ultrasonic transducer (TDSE 28, Tamura; frequency: 1 MHz; applied voltage: 7 Vrms). It was thus confirmed that the desired ultrasonic standing wave was generated inside the agar sample after ultrasonic vibration. However, while the theoretical reflection plane depth of the ultrasonic standing wave was 0.375 mm, the actual measured reflection plane depth for this ultrasonic standing wave was 0.15 mm. This difference is attributed to higher-order harmonics that occur because of the parametric effect on the incident sound waves, which means that ultrasonic standing waves with shallow depths are then generated.

The parametric effect [49] is a nonlinear phenomenon that distorts the waveform when an incident sound wave propagates inside a sample. As shown in Figure 1, a sinusoidal wave incident on a nonrigid sample generates a higher harmonic wave that distorts to look like a sawtooth wave as the waveform propagates because the nonrigid sample has high compressibility. The sawtooth wave can then be analyzed by resolving it into integer multiple higher harmonics via a Fourier transform. We therefore consider that these harmonic standing waves form for each frequency component. The waveform that is obtained by adding these standing waves is called a parametric standing wave. In the case of ultrasonic vibration in agar, because reflection planes with depths of approximately one-third of the theoretical value were observed, it is proposed that these are reflection planes generated at the nodes of the third harmonic.

Additionally, if the ultrasonically assisted spectrometer that combines an ultrasonic liquid cell and one-shot Fourier spectroscopy is attached to earlobes, we will be able to measure blood glucose concentrations inside the bio-membrane. This is a new approach of designing a non-invasive blood glucose sensor.

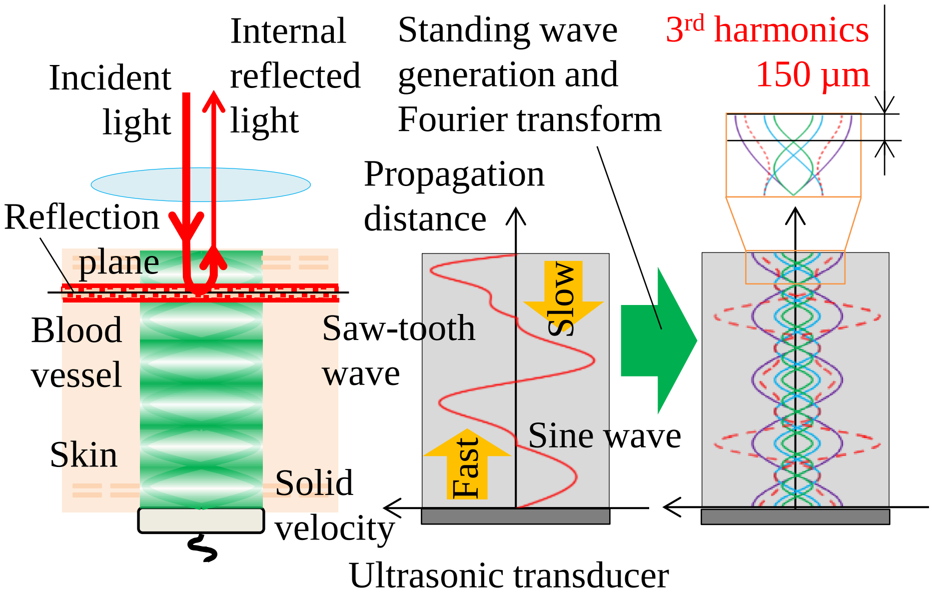

Figure 8 Schematic diagram of an ultrasonic liquid cell and parametric standing waves

1.5 *Verification experiment of a on-site long-wavelength infrared spectroscopic measurement*

To demonstrate the feasibility [50] of on-site measurement with a Fourier infrared spectrophotometer for realizing a non-invasive blood glucose level sensor in a daily-life environment, we performed a animal experiment in which we measured blood glucose non-invasively for a mouse using an imaging-type 2D Fourier spectroscopic imager and ultrasonic liquid cell.

First, adopting optical coherence tomography (OCT) (model: IVS-2000, manufacturer: Santec) [51-53], we confirmed the generation of ultrasonic standing waves inside the skin of a mouse (model: C57BL / 6JJcl *, manufacturer: CLEA Japan Inc.) as shown in Fig. 9. The thickness of the mouse ear was 0.33 mm, which was small compared with the wavelength of ultrasonic waves of 1.5 mm, and the thickness was thus supplemented by inserting agar, which was used as a biological simulation sample. The frequency was set to 1 MHz and the voltage was set to 5 V. As shown in Fig. 6, we confirmed that an ultrasonic standing wave was generated at a depth of about 0.1 mm as the reflection surface by OCT. In addition, when a 10-MHz ultrasonic wave is applied to the glucose solution, a standing wave is generated at almost the same position as the standing wave generated at a depth of about 0.1 mm from the surface. Therefore, the inside of the living body is generated from the ultrasonic vibrator. It is judged that there is a parametric effect where sound waves of different frequencies are generated as the sound waves progress.

As shown in Fig. 10, blood glucose was measured on the skin (measurement site: ear) of mice using an imaging-type 2D long-wavelength infrared Fourier spectroscopic imager and an ultrasonic liquid cell. The optical system comprised a wideband infrared camera (model: WBIRCam-640, manufacturer: Vision Sensing) as a receiver, Kantal infrared light source (model: EK8620, manufacturer:

HELIOWORKS) as a light source, and short-pass filter (model: SP-10300nm, manufacturer: Spectrogon). The field of view was about 10 mm × 10 mm. The mouse was a healthy individual with a blood glucose level of about 169 mg/dl. A 0.2-ml quantity of 0.1-g/dl sugar water was injected into the abdominal cavity of the mouse, and the blood glucose concentration was measured as about 379 mg/dl with a puncture-type blood glucose sensor (model: GT-1840, manufacturer: Arkray) after 15 minutes. The blood glucose level was about 399 mg/dl when measured after 30 minutes. At the same time, adopting ultrasonic waves with a frequency of 1 MHz and a voltage of 7 V, absorption peaks [54,55] were obtained at glucose absorption wavelengths of 9.25 and 9.65 μm.

However, quantitative measurement [56-60] was not possible owing to three issues. First, the level of incident light was low owing to distance attenuation due to the long optical axis. The measurement sensitivity was thus insufficient. Second, because a temporal-phase-shift interferometer [61-65] such as the Michelson interferometer or imaging-type Fourier spectrometer requires movement of a mirror, it is difficult to remove stray light resulting from fluctuation of the atmosphere and humidity and the body temperature of the experimenter because the time resolution is low. Third, the signal-to-noise ratio of the interferogram and spectroscopic characteristics are poor because of the first two issues.

The realization of a Fourier infrared spectrophotometer capable of on-site measurement therefore requires the use of a spatial-phase-shift interferometer [66-77] such as a one-shot Fourier spectrometer having a short optical axis and high time resolution. A spatial-phase-shift interferometer that does not have a mechanical drive and comprises only a lens and an inclining prism can be miniaturized, allowing spectroscopic measurement in close proximity to the sample and in real time. It is therefore possible to remove disturbance components such as fluctuations in the atmosphere and humidity. It is necessary to provide a field aperture in principle, and the measurement sensitivity of the spatial-phase-shift interferometer is thus an issue. However, in the work described in this paper, the sensitivity and signal-to-noise ratio of the spatial-phase-shift interferometer is improved. Furthermore, a new spectroscopy method with high wavelength resolution is established.

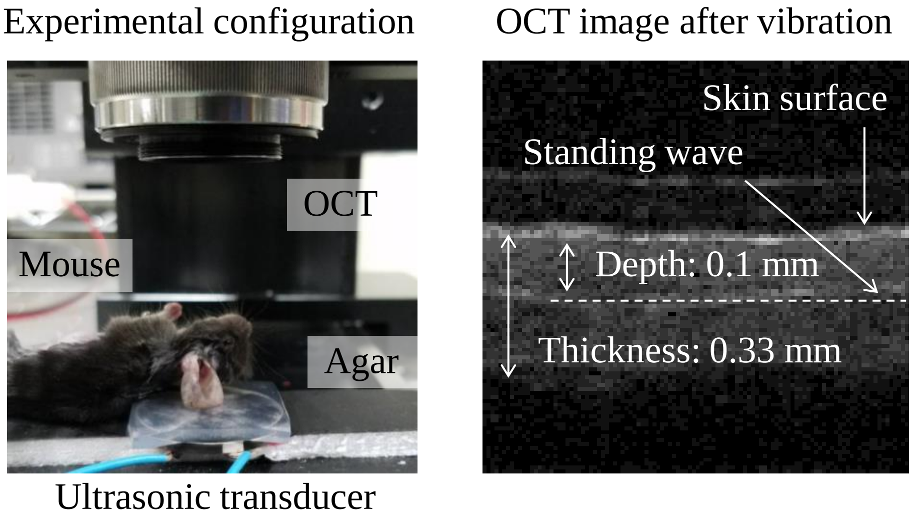

Figure 9 Generation of the reflection plane by the ultrasonic standing wave inside the ear of a mouse

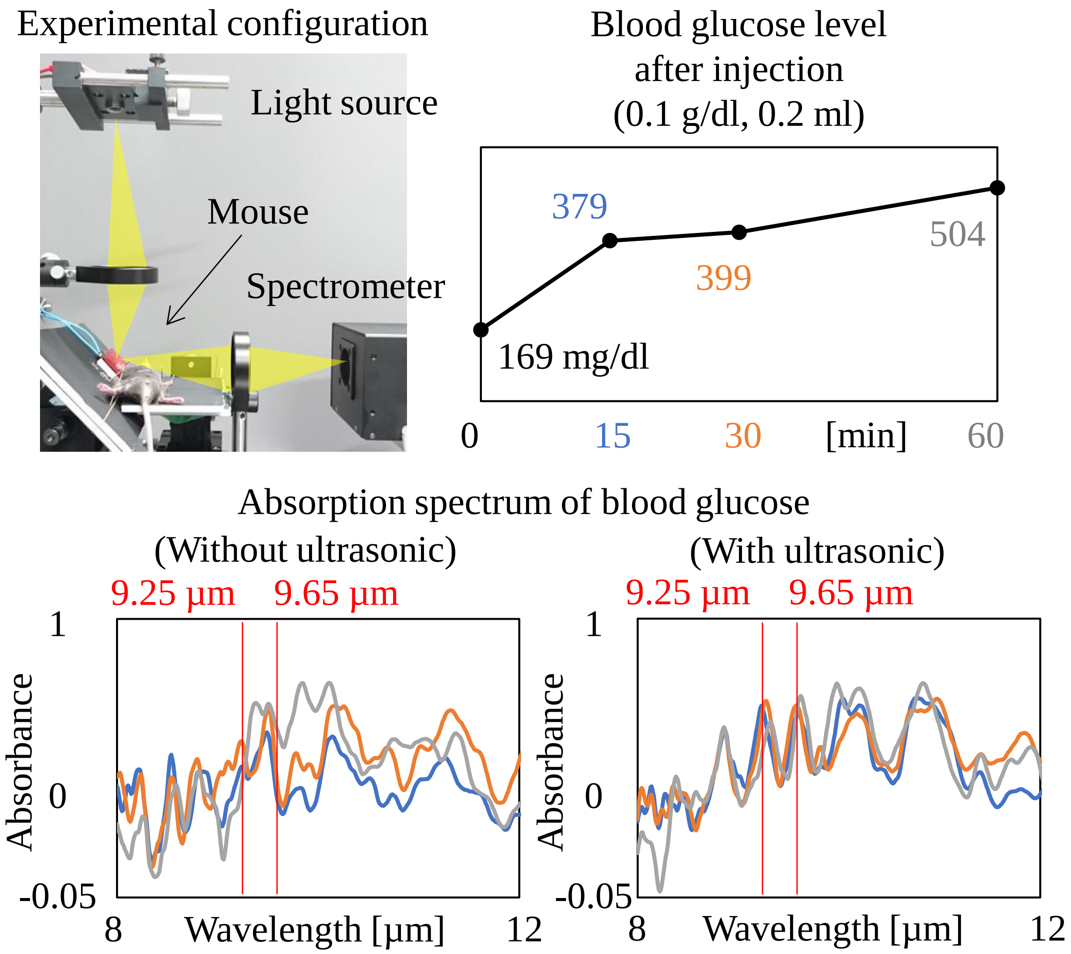

Figure 10 Non-invasive blood glucose measurement of a mouse using an imaging-type 2D Fourier spectroscopic imager

1.6 Outline of the thesis

The ultra-miniature long-wavelength infrared Fourier spectroscopy with high wavelength resolution and high sensitivity for realizing on-site component measurement is explained in the following four chapters. Each chapter is outlined as follows.

Chapter 1 explained that, by establishing a small infrared spectroscope as a component sensor that can be mounted on wearable terminals, infrared spectroscopy can help realize a society in which casual daily-life data acquired by the general public contributes to solving social problems. The research background, research purpose, and position of the research are described. The chapter also explains the principles of conventional spectroscopy and proposed spectroscopy, such as one-shot Fourier spectroscopy, which uses a spatial-phase-shift interferometer that can be miniaturized to the scale of a bean.

Chapter 2 proposes the wide-field-stop and beam-expansion method [78] focusing on the aperture area and diffraction angle of the field stop existing on the object surface of the spatial-phase-shift interferometer and describes results of a verification experiment. The amount of incident light increases as the aperture area increases, which improves the intensity of light detected on the spectroscopic imager. A decrease in the diffraction angle due to an increase in the aperture width is improved by inserting a plano-concave cylindrical lens between the objective lens and field stop. “Letter: Sensitivity improvement of one-shot Fourier spectroscopic imager for realization of noninvasive blood glucose sensors in smartphones”

Chapter 3 proposes the superimposing interferogram method [79] for the purpose of increasing the sensitivity of the spatial-phase-shift interferometer and improving the interference definition. In clarifying the maximum aperture width of the field stop, we find that the interference sharpness depends on the aperture width. By hypothesizing this optical phenomenon with a physical model and demonstrating it through experiments, we establish a method of designing multi-slits used on the object conjugate plane of the optical system. We also propose a wideband multi-slit that solves the band narrowing phenomenon of the detected wavelength region, which is a problem facing the superimposing interferogram method. We propose a wavelength-splitting-type multi-slit array that pseudo-improves the wavelength resolution of the spectroscopic imager. Light around the central wavelength used in the design of multi-slits is mainly extracted to form interference fringes, and only a specific narrow band wavelength can thus be used for spectroscopic measurement. The band narrowing phenomenon is hypothesized using a physical model and clarified experimentally. “Journal Article: Superimposing method using a multi-slit array to enhance sensitivity and interference definition of spatial-phase-shift interferometers”

Chapter 4 proposes point-one-shot Fourier spectroscopy [80] having the features of high wavelength resolution, small size (i.e., bean size), and low price (100,000 yen or less). This method is positioned as spatial-phase-shift interferometry and can be realized with a simple optical configuration comprising only one objective lens, where the back surface has the shape of a wedge prism and inclination around two axes, and a low-resolution camera. In addition, because the interference fringes develop two-dimensionally, the optical path length difference can be secured using the entire light receiving surface, which provides high wavelength resolution. “Proceeding: Ultra-miniature (diameter: 6 mm, thickness: 5 mm) low-cost (price: 1,000 EUR) point-one-shot long-wavelength infrared Fourier spectroscopic imager for ear clip type non-invasive blood glucose sensors”

Finally, a summary of the thesis is presented.

CHAPTER 2

Wide-field-stop and beam-expansion method to enhance the detected light intensity of spatial-phase-shift interferometers

2.1 Abstract

The use of the wide-field-stop and beam-expansion method for sensitivity enhancement of one-shot Fourier spectroscopy is proposed to realize health care sensors installed in smartphones for daily monitoring. When measuring the spectral components of human bodies non-invasively, diffuse reflected light from biological membranes is too weak for detection using conventional hyper-spectral cameras. One-shot Fourier spectroscopy is a spatial phase-shift-type interferometer that can determine the one-dimensional spectral characteristics [81-88] from a single frame. However, this method has low sensitivity, so that only the spectral characteristics of light sources with direct illumination can be obtained, because a single slit is used as a field stop. The sensitivity of the proposed spectroscopic method is improved by using the wide-field-stop and beam-expansion method. The use of a wider field stop slit width increases the detected light intensity; however, this simultaneously narrows the diffraction angle. The narrower collimated objective beam diameter degrades the visibility of interferograms. Therefore, a plane-concave cylindrical lens between the objective plane and the single slit is introduced to expand the beam diameter. The resulting sensitivity improvement achieved when using the wide-field-stop and beam-expansion method allows the spectral characteristics of hemoglobin to be obtained non-invasively from a human palm using a midget lamp.

2.2 Principle

2.2.1 Galilean and Keplerian beam expander

When we construct the optical system, we need to expand or diminish the beam size midway along the optical axis occasionally. As an example, we should make a thick collimated beam to obtain the light intensity efficiently or observe the fringe pattern over a wide area. We usually use two lenses to expand the diameter of the beam. The lens on the incident side spreads and expands the collimated beam. The lens on the outgoing side collimates the beam again. The optical system of the beam expander [89-93] expands or diminishes the collimated beam size by a certain magnification. The Galilean beam expander uses concave and convex lenses. The Keplerian beam expander uses only convex lenses.

The Galilean beam expander has three characteristics. First, we can decrease the length of the optical axis. Second, we can obtain high efficiency using only a few lenses. Third, the beam expander can be used for a high output laser. As shown in Fig. 11(a), the focal lengths of concave and convex lenses are f_N and f_P. Additionally, the diameters of incident and outgoing beams are C_1 and C_2. We then calculate the magnification (B_1) of the beam expansion using Equation (1).

$$B_1 = \frac{f_P}{f_N} = \frac{C_2}{C_1} \tag{1}$$

The Keplerian beam expander has two characteristics. First, we can insert a pinhole midway along the optical system of the beam expander. Second, we can then obtain the outgoing beam whose intensity follows a clear Gaussian distribution utilizing the spatial filter effect of the pinhole. We cannot use a high-output laser in the optical system because the transmitted wave front is broken up by the spark at the light focus point. As shown in Fig. 11(b), the focal lengths of convex lenses are f_1 and f_2. Additionally, the diameters of incident and outgoing beams are C_3 and C_4. We then calculate the magnification (B_2) of the beam expansion using Eq. (2).

$$B_2 = \frac{f_2}{f_1} = \frac{C_4}{C_3} \tag{2}$$

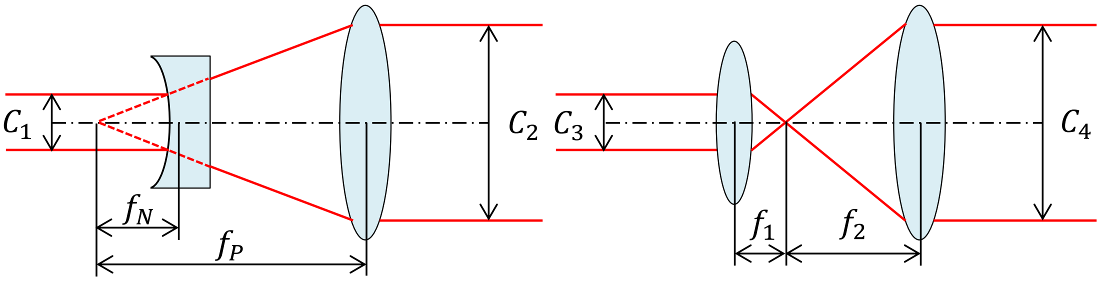

(a) (b)

Figure 11 Principle of the beam expander

2.2.2 Design guideline of the field stop

I introduce the proposed multi-slit optical superposition method [94] that prevents the deterioration of interference definition using side-by-side bright points. This method superimposes the conjugate image of the objective plane on the amplitude grating to remove side-by-side bright points. The distribution of the interference intensity on the imaging plane changes greatly unless we design the most suitable field stop, which is an amplitude grating.

The main purpose of the method is to prevent images of airy discs of side-by-side bright points from overlapping on the imaging plane. However, when the distance between bright points is too great, there are areas that cannot be measured between bright points and unevenness of the interference intensity on the imaging plane. Then, when we design the field stop to divide an airy disc into 3 pixels on the imaging plane as shown in Fig. 12, we obtain a uniform distribution of the interference intensity. When we divide the center of a bright point's airy disc and the first dark ring of the adjacent bright point's airy disc before the first diffraction ring, with their phases differing by π, we confirm the change in the interference intensity most clearly. Therefore, the image of the aperture area that has a width corresponding to 2 pixels should be set on the center of 3 pixels (constraint condition 1). The interference intensity deteriorates too much if the airy disc is divided smaller than 3 pixels.

Additionally, the aperture distance should be the same as the diameter of the airy disc (constraint condition 2) for separating off the center of the bright point's airy disc and the first dark ring of the adjacent bright point's airy disc before the first diffraction ring. When the first dark rings having a phase difference of π are bordering, the interference intensity is well defined by the high independence of phase changes in a pixel.

The width of the aperture area is denoted D. There are several bright points inside the aperture area, and their convolution produces an airy disc on the imaging plane. The diameter L of the airy disc is calculated using Eq. (3).

$$L = D \times m + a \tag{3}$$

Here, m is the optical magnification and a is the radius of the first dark ring made by bright points inside the aperture. Because a is almost the same as D, we can replace Eq. (3) with Eq. (4).

$$L = D \times m + D \tag{4}$$

When m is equal to 1, we calculate the length of the aperture area and the width of the aperture as shown in Fig. 13.

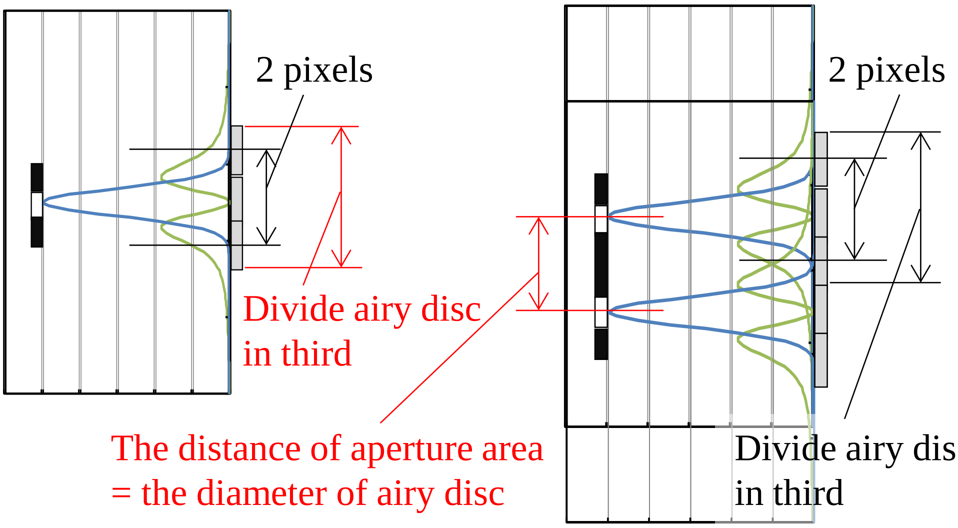

Figure 12 Constraint conditions 1 (left) and 2 (right)

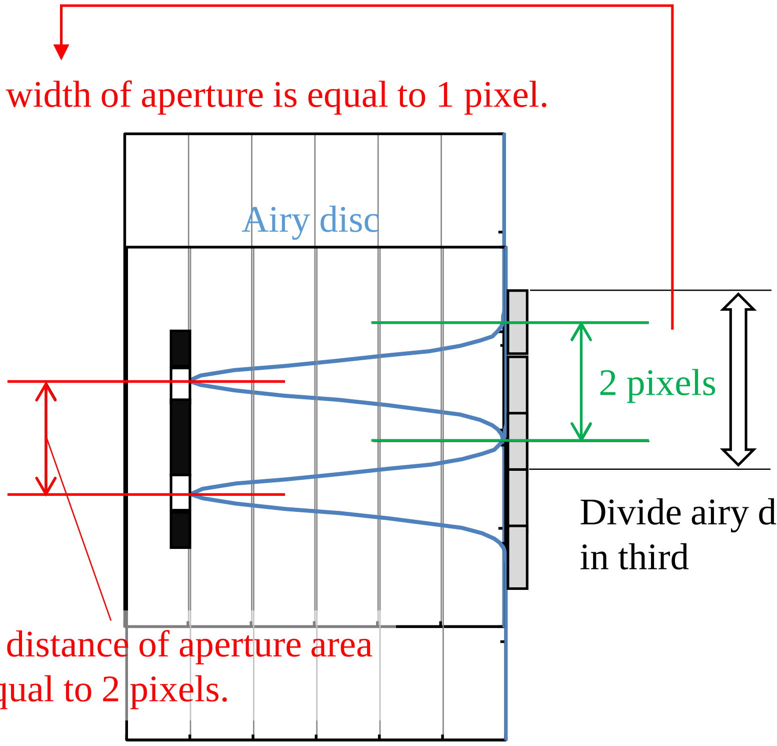

Figure 13 Design guideline of the aperture area for the field stop when using the multi-slit optical superposition method

2.2.3 Optical system of the proposal beam-expansion method

We explain the principle of the wide-field-stop and beam-expansion method for the sensitivity enhancement of a spatial-phase-shift interferometer, such as that used in one-shot Fourier spectroscopy. The spectroscope is a simple optical system that comprises three lenses: an objective lens, a cylindrical lens, which is the imaging lens, and a transmission-type relative-inclined phase-shifter, which is configured using a glass wedge and cuboid. The spectroscopic system has low sensitivity because a slit, which acts as a field stop, is introduced into the optical system.

We made a prototype field stop that has several different horizontal widths of the aperture area as shown in Fig. 14. The vertical width of the aperture of the field stop is calculated as 6 μm according to the multi-slit optical superposition method and pixel size of the complementary metal–oxide–semiconductor (CMOS) camera. In increasing the detected light intensity and clarifying the maximum width of the aperture area, using a wider slit in the field stop would obviously produce higher light intensity. However, because our method is based on wavefront-division interferometry, a problem arises where the use of a wider single slit makes the diffraction angle narrower, as shown in Fig. 15 and by Eq. (5). This means that narrower diameters of the collimated objective beams deteriorate the clarity of the interferograms, as shown in Fig. 16(a) and 16(b). The width of the aperture area before expansion is denoted A, that of the aperture area after expansion is denoted $B,$ and the wavelength and diffraction angles are denoted λ, θ_A, and θ_B as shown in Fig. 15.

$$A = \frac{\lambda}{\sin\theta_A}, \quad B = \frac{\lambda}{\sin\theta_B}$$

$$\frac{B}{A} = \frac{\dfrac{\lambda}{\sin\theta_A}}{\dfrac{\lambda}{\sin\theta_B}} = \frac{\sin\theta_A}{\sin\theta_B}$$

$$\frac{B}{A} = \frac{\sin\theta_A}{\sin\theta_B} > 1 \quad (\because B > A, \theta_A > \theta_B) \tag{5}$$

Therefore, by reducing the diffraction angle and the diameters of objective beams that penetrate through the glass cuboid and wedge, these objective beams cannot undergo interference on the imaging plane and create an interferogram.

By installing a relative-inclined phase-shifter on the optical Fourier transform plane of an infinity-corrected optical system, the collimated half flux of the objective beams that originate from single bright points on the objective surface penetrate through the wedge prism and glass cuboid. The two beams then interfere with each other and form an interferogram in the form of spatial fringe patterns. We thus installed a plano-concave cylindrical lens between the wider slit and the objective lens to act as a beam expander.

Two main configurations are available for beam expanders: Keplerian and Galilean. In the proposed method, we install a Galilean beam expander so that the spectrometer may be introduced into a smartphone, as the Galilean beam expander requires a shorter optical path length than the Keplerian device. A Galilean beam expander requires a plano-concave lens, but when we used a plano-concave lens as the Galilean beam expander, the optical path lengths are extended not only along the horizontal axis but also along the vertical axis. We then used a plano-concave cylindrical lens rather than a plano-concave lens to extend the optical path length on the horizontal axis only, as shown in Fig. 16(c), because this avoids cancellation of the adjacent bright spots that prevents us from obtaining the interferogram. As a result, the continuous spatial-phase-difference objective beams coincide with each other on the imaging plane and can interfere. We have therefore improved the sensitivity of the proposed one-shot Fourier spectroscopy method using the wide-field-stop and beam-expansion method.

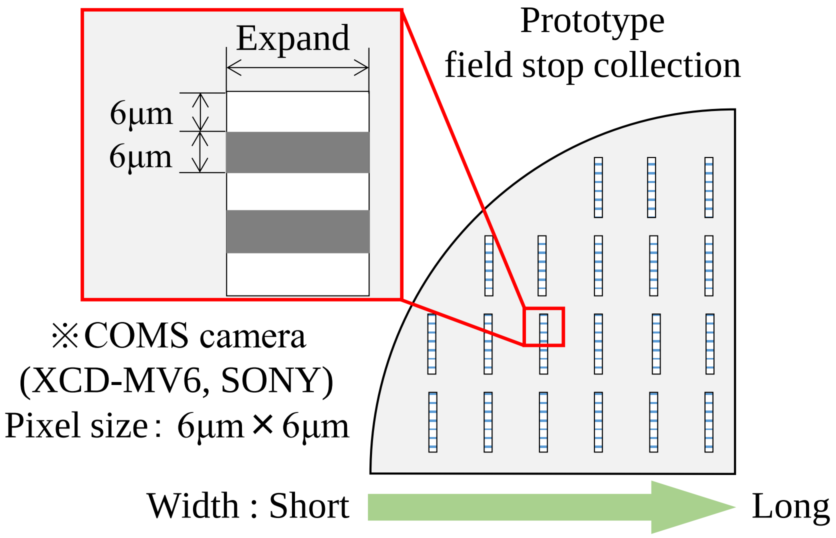

Figure 14 Prototype field stop for clarifying the maximum width of the aperture and the limited improvement of light intensity

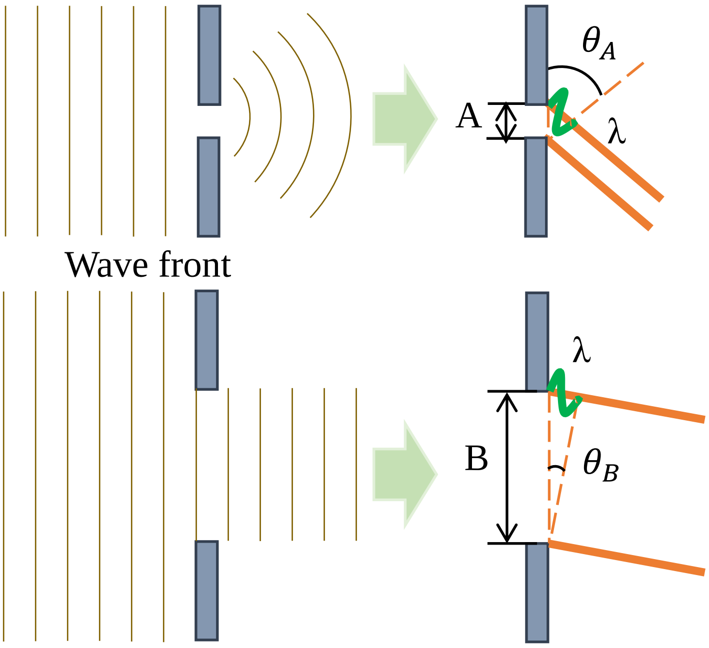

Figure 15 Deterioration of diffraction angles at apertures from width A to B

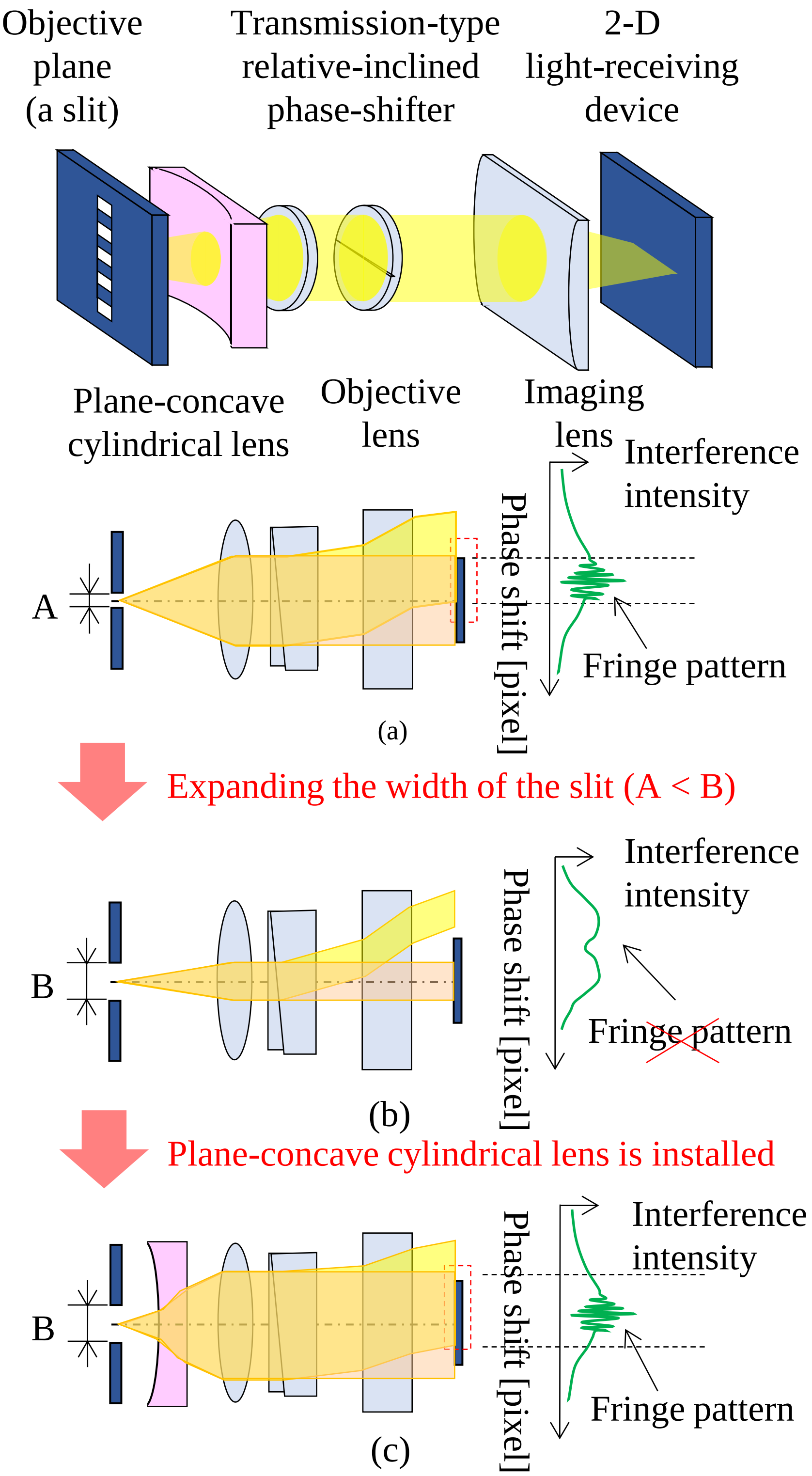

Figure 16 Principle of the wide-field-stop and beam-expansion method

2.3 Verification experiment

We confirmed the results of the wide-field-stop and beam-expansion method through verification experiments, as shown in Fig. 17. In the experiments, the one-shot Fourier spectroscopic imager consisted of an objective lens (focal length of 50 mm), an imaging lens (cylindrical lens, focal length of 50 mm) and a transmission-type relative-inclined phase shifter. We then structured the Koehler illumination to average the distribution of the light source. We also introduced a plano-concave cylindrical lens (focal length of −25 mm) into the optical system to act as a Galilean beam expander. We used a CMOS camera (XCD-MV6, Sony Corporation) on the imaging plane, the slit (horizontal pattern length of 54 μm; vertical pattern length of 6 μm) on the object plane, and a white light-emitting diode (LED) (OSW54L5111P, OptoSupply). The objective beams that were collimated by the objective lens formed on the imaging plane but did not interfere because the beam diameter was short and the beams coincided with each other without the Galilean beam expander. We did not obtain the interferogram and the spectral characteristics of the light source, as shown in Fig. 18(a). However, the objective beams that were collimated by the objective lens formed on the imaging plane and interfered with each other when using the Galilean beam expander. We could therefore obtain the required interferogram and the spectral characteristics of the light source because of the expansion of the length of the beams by the beam expander, as shown in Fig. 18(b). Therefore, we demonstrated the sensitivity enhancement required for the one-shot Fourier spectroscopic imager when using the wide-field-stop and beam-expansion method by confirming the target spectral characteristics and acquiring the interferogram after the amount of light available was increased by expanding the slit width.

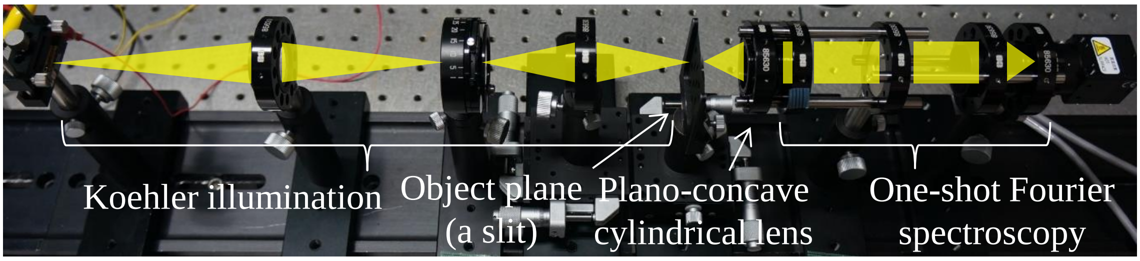

Figure 17 The optical system used for the verification experiments

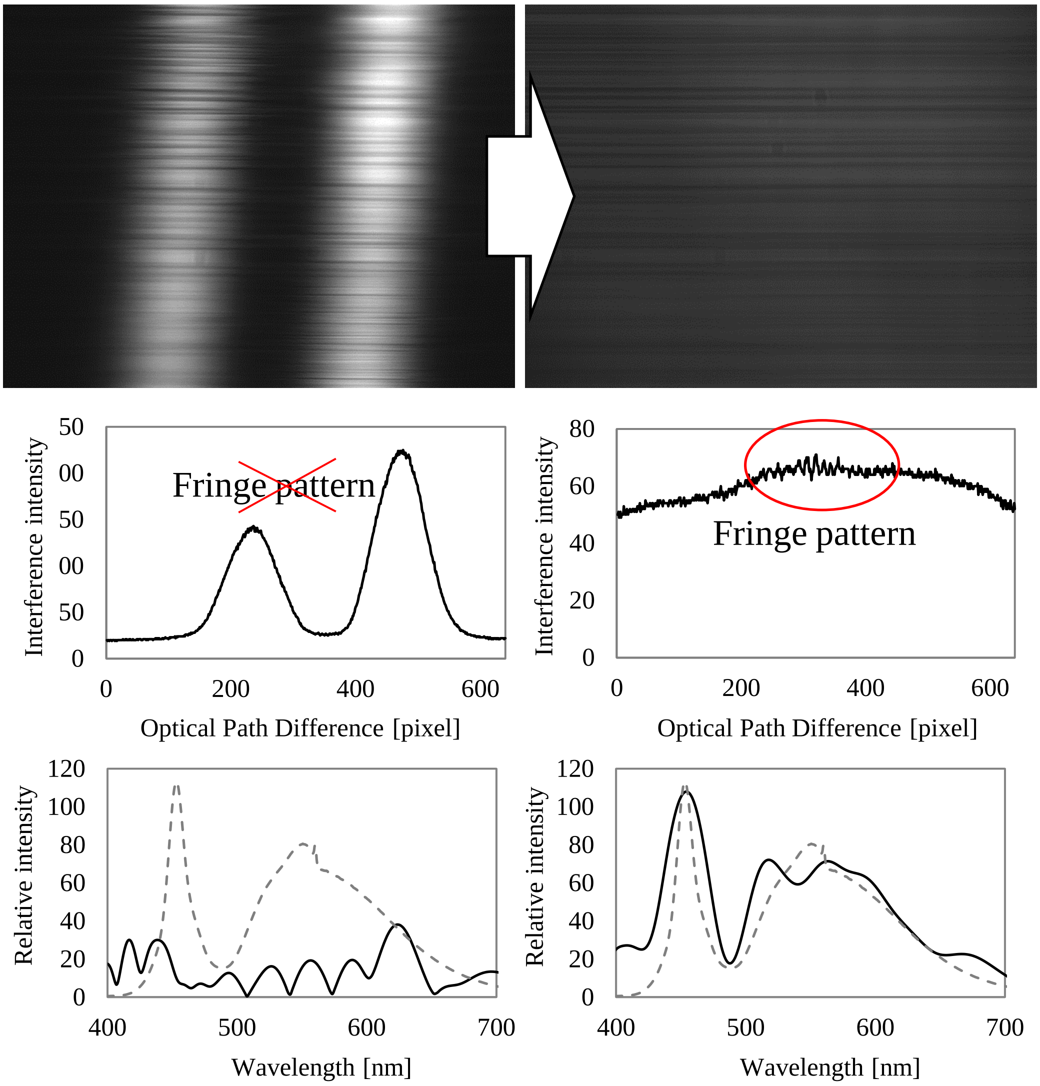

(a) (b)

Figure 18 Results from the verification experiments (a) without and (b) with a Galilean beam expander

2.4 Biomedical measurement

We measured the absorbance of rat blood using a dispersive spectrometer (SolidSpec-3700, Shimadzu) and the absorbance of a human hand using the proposed one-shot Fourier spectroscopic imager with enhanced sensitivity. In this experiment, a halogen lamp (JR12V50WLN/NZ/EZ-IR, Ushio) was used as the light source, as shown in Fig. 19. Then we obtained the image and the interferogram as shown in Fig. 20(a) and Fig. 20(b), respectively. The two samples show similar absorption characteristics for hemoglobin, with a decrease from 600 nm to 700 nm and increase from 700 nm to 900 nm, as shown in Fig. 20(c) and Fig. 20(d). We have therefore confirmed the diffuse reflection of light from human skin [95] and have demonstrated the feasibility of performing non-invasive biomedical measurements using the one-shot Fourier spectroscopic imager after the proposed sensitivity enhancement.

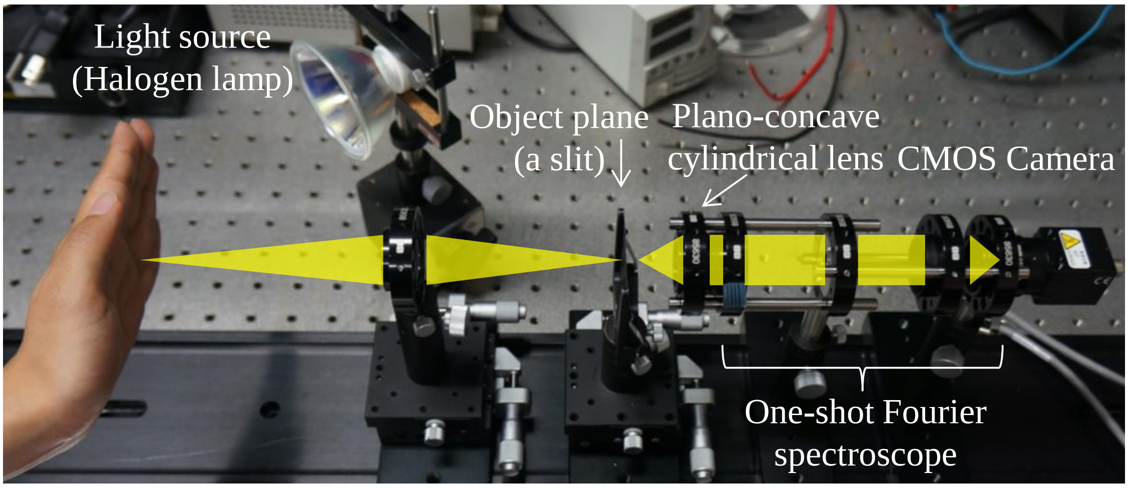

Figure 19 Optical system used for the biomedical measurements

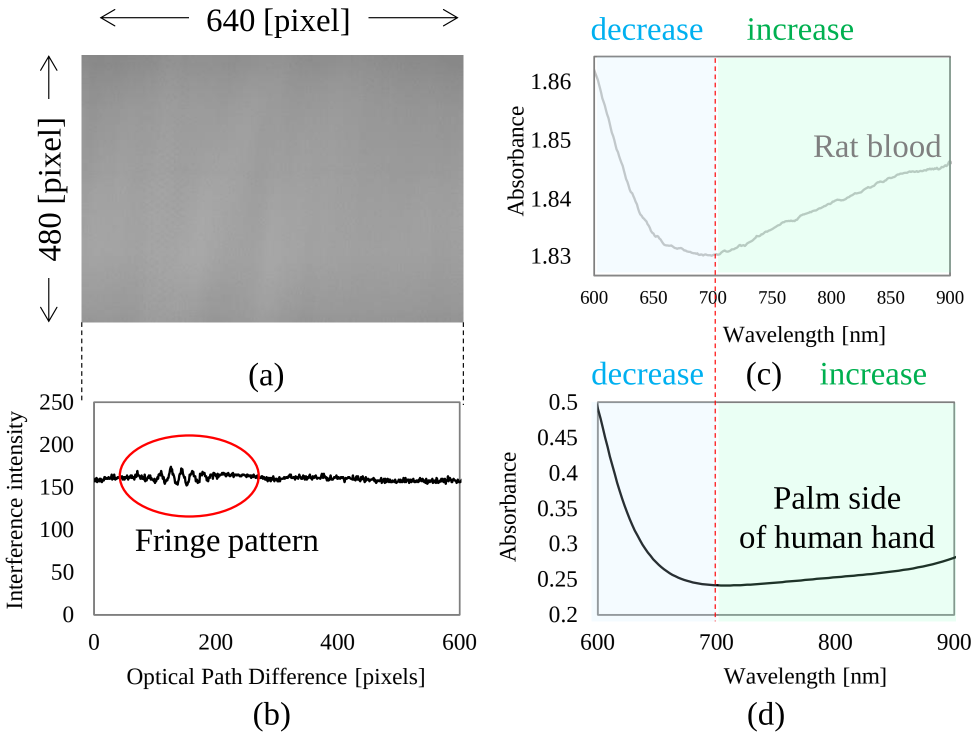

Figure 20 (a) The image and (b) the interferogram from the biomedical measurements. Absorption characteristics of (c) rat blood and (d) the human hand

2.5 Summary

We proposed the use of the wide-field-stop and beam-expansion method for sensitivity enhancement of the one-shot Fourier spectroscopy method. We discussed the principles of the sensitivity improvement method, which supports both the sensitivity and wavelength resolution requirements of this spectroscopic method. Additionally, we confirmed the suitability of the method through verification experiments and biomedical experiments.

CHAPTER 3

Superimposing interferogram method using a multi-slit array to enhance sensitivity and interference definition of spatial-phase-shift interferometers

3.1 Abstract

We propose a superimposing interferogram method to enhance the sensitivity and interference definition of spatial-phase-shift interferometers. The proposed method uses a multi-slit array as a redesigned field stop for the spatial-phase-shift interferometer. The widths of the apertural and blocked areas correspond to half the wavelength of the fringe pattern on the imaging plane and determine the wavelength that improves the interference definition while eliminating those wavelengths that worsen it, thus improving the interference definition of the interferogram. Additionally, to improve the interferometer's sensitivity, several apertural areas were aligned to increase the amount of incident light. We performed spectroscopic measurements and confirmed improvements in both the sensitivity and the interference definition using a prototype of a bean-sized long-wavelength infrared spectroscopic imager based on a one-shot Fourier spectroscope and a prototype multi-slit array. Although long-wavelength infrared light is absorbed well by water and its intensity is thus weak for detection using the array sensors of cameras, long-wavelength infrared spectroscopic imagers that incorporate our proposed method can be used for biomedical measurements of samples containing water.

3.2 Principle

For our superimposing interferogram method, a multi-slit-array was designed based on a conventional field stop to have more than one aperture area running periodically along the horizontal axis. The conventional field stop of a spatial-phase-shift interferometer uses only the incident coherent light. However, these field stops yield low sensitivities because the aperture area of the incident light is small. As shown in Fig. 21, using one-shot Fourier spectroscopy, which uses one type of spatial-phase-shift interferometer, we tried to extend the width of the aperture area horizontally to increase the amount of incident light. We do not have to consider the height of the field stop because the height is determined by the optical superposition method . As shown in Eqs. (6) and (7), the sensitivity (I_s) represents the median detected light intensity and the interference definition (I_d) is expressed expediently using the difference between the maximum (I_{max}) and minimum (I_{min}) values of the interferogram intensity because we wish to consider this definition separately from that of the detected light intensity.

$$I_s = \frac{I_{max} + I_{min}}{2} \tag{6}$$

$$I_d = I_{max} - I_{min} \tag{7}$$

The field stop width is L and the detected light intensity is 1 before the width is broadened. When the aperture area increases from 1L to 5L, the sensitivity increases in tandem from 1 to 5. However, we simultaneously discovered a phenomenon where the interference definition alternately improves and worsens. Because we developed an expression for the most appropriate width of the aperture area (L) and lined up the aperture area and the shielded area periodically by analyzing this phenomenon, the sensitivity and the definition can be increased at the same time by increasing the number of aperture areas. To explain this phenomenon and illustrate the principle of our proposed method, we present the schematic image shown in Fig. 22.

Note that in Fig. 21 and Fig. 22, fringe patterns of white light are shown because their waveforms are easily viewable when they are superimposed on each other. First, as shown in Fig. 22(A), the aperture area can be regarded as a bright point group on the field stop. The interference definition of the black interferogram formed by the light of the zero-point (center) bright point degrades when the blue interferograms, in which the phase is half the wavelength ($\frac{\lambda}{2}$) in the horizontal direction, are superimposed on it. Conversely, the interference definition of the red interferogram formed when the phase is one whole wavelength (λ) in the horizontal direction improves. As shown in Fig. 22(B), the multi-slit array removes the bright points that form the blue interferogram (fringe pattern (b) in Fig. 22) by the shielded area when the phase is half the wavelength and uses the bright points to form the red interferogram (fringe pattern (a) in Fig. 22) when the phase is one whole wavelength to improve the sensitivity and the interference definition simultaneously (Fig. 21, right panel and Fig. 22, bottom panel). When the width of the bright point in Fig. 22 is equal to L, which is the width of the aperture area in Fig. 1, the total width of the aperture area in Fig. 22(B) is 3L. Therefore, if the aperture areas are lined up periodically and the number of aperture areas is n, the sensitivity and the interference definition are both improved n-fold with use of monochromatic light. We call this method the multi-slit superimposing interferogram method.

We now describe how to calculate the width of the aperture and the blocked area on the multi-slit using the interference condition of the phase-shift operation. First, we introduce the optical path difference per pixel $\Delta\lambda$. When using monochromatic light of wavelength λ, the image width of the aperture area (L') on the imaging plane is set to

$$L' = \frac{\lambda}{2} \tag{8}$$

to stop the interferogram from cancelling the zero-point interferogram through the blocked area of the multi-slit array. The image width (L') on the imaging plane is then converted into a pixel count (L'') using

$$L'' = \frac{\lambda}{2\Delta\lambda} \tag{9}$$

Next, we calculate the projection ratio of the grating, which is dependent on the positions of the objective plane and the imaging plane. We introduce the pitch P of a camera pixel, the focal length f_1 of the objective lens, the focal length f_2 of the imaging lens, the altitude x of the object, and the altitude x' of the image. As shown in Fig. 23, the incident light of the zero-point on the objective plane forms an interferogram at the same phase position as the interferogram of the incident light that passes through the principal point of the objective lens. Therefore, when using a one-shot Fourier spectrometer, which projects the collimated light beam onto the imaging plane, the projection ratio of the grating is

$$x' = 2\frac{f_2}{f_1}x \tag{10}$$

Then, the width of the aperture area on the multi-slit array (L) at the objective plane is

$$L = \frac{\lambda}{4\Delta\lambda\frac{f_2}{f_1}} \times P \tag{11}$$

Figure 24(a) presents a fringe pattern of monochromatic light on the imaging plane. The width of the aperture area on the imaging plane is denoted by $\Delta\theta$ and the amplitude of the fringe pattern is denoted by A. The intensity $I(\theta)$ of the interferogram formed by adding all interferograms of the bright points from θ_a to $\theta_a + \Delta\theta$ in the horizontal direction is calculated from

$$I(\theta_a) = A\int_{\theta_a}^{\theta_a+\Delta\theta} (\sin\theta + 1)\,d\theta = 2A\sin\left(\theta_a + \frac{\Delta\theta}{2}\right) + A\Delta\theta \tag{12}$$

As shown in Fig. 24(b), (1) is the amplitude of the interferogram (Fig. 25), (2) is the phase difference and (3) is the offset. Therefore, we can demonstrate the phenomena shown in Fig. 21 and Fig. 22 via simulations with calculations based on Eq. (12) and Fig. 24. For example, when $\Delta\theta$ is 180°, the amplitude is at a maximum of 2A. When $\Delta\theta$ is 360°, the amplitude is at a minimum of 0. The amplitude changes periodically from 0 to 2A (from 0 to 2π) and the offset increases as the width of the aperture area increases. We evaluate the sensitivity based on the intensity of the central interferogram on the vertical axis and the interference definition, i.e., the difference between I_{max} and I_{min}.

When n aperture areas for which the phases are the same are aligned to form a multi-slit array, the amplitude and offset increase n-fold, as shown by:

$$nI(\theta_a) = nA\int_{\theta_a}^{\theta_a+\Delta\theta} (\sin\theta + 1)\, d\theta = 2nA\sin\left(\theta_a + \frac{\Delta\theta}{2}\right) + nA\Delta\theta \quad (13)$$

That is, the sensitivity and the interference definition are improved by the multi-slit array.

When white light is also used, the width of the aperture can be calculated using its central wavelength λ_c. The sensitivity increases n-fold with the aperture area. However, the intensity of the interference does not conform because the negative part, which is out of phase with the base interferogram by $\frac{\lambda_m}{2}$, degrades the interference definition because the bright point that made the interferogram cannot be removed accurately (m is assigned a counting number). When the amplitude of the fringe pattern for the central wavelength is 1, the amplitude of the fringe pattern for each wavelength can then be calculated using

$$A_m = \left|\sin\frac{\lambda_c}{2\lambda_m}\pi\right| \quad (14)$$

(see Fig. 25).

When a bright point (i.e., an aperture area) on the side forms a fringe pattern, a stretched fringe pattern is then formed by the field angle of the incident light on the imaging plane. Consequently, the spectral peak is shifted to longer wavelengths. This shift can be corrected using Fig. 23 (plane view) and

$$\theta = \tan^{-1}\frac{L}{f_1}, \quad \frac{D}{d} = \frac{1}{\cos\theta} \tag{15}$$

where the length of the real fringe pattern is denoted by d and the length of the stretched fringe pattern on the imaging plane is denoted by D. We can calculate the required value for correction of the spectral peak using Eq. (15), which gives the magnification of the expansion. For example, the width L of the aperture area, which is calculated using λ_c=10 μm, is 43 μm, the number of aperture areas is 5, and we use an objective lens (focal length: 3 mm). The spectral peak then shifts by 0.1% of the wavelength.

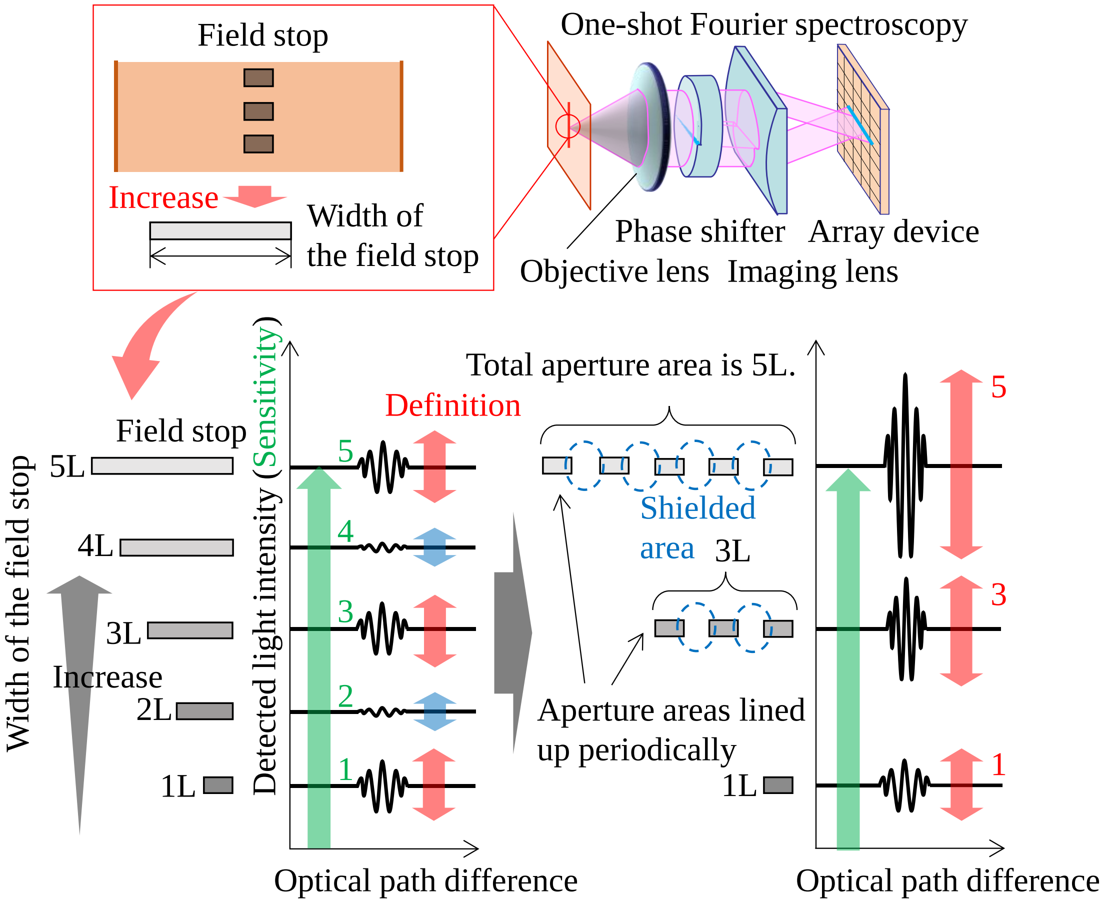

Figure 21 Dependence of the sensitivity and the interference definition on the width of the field stop

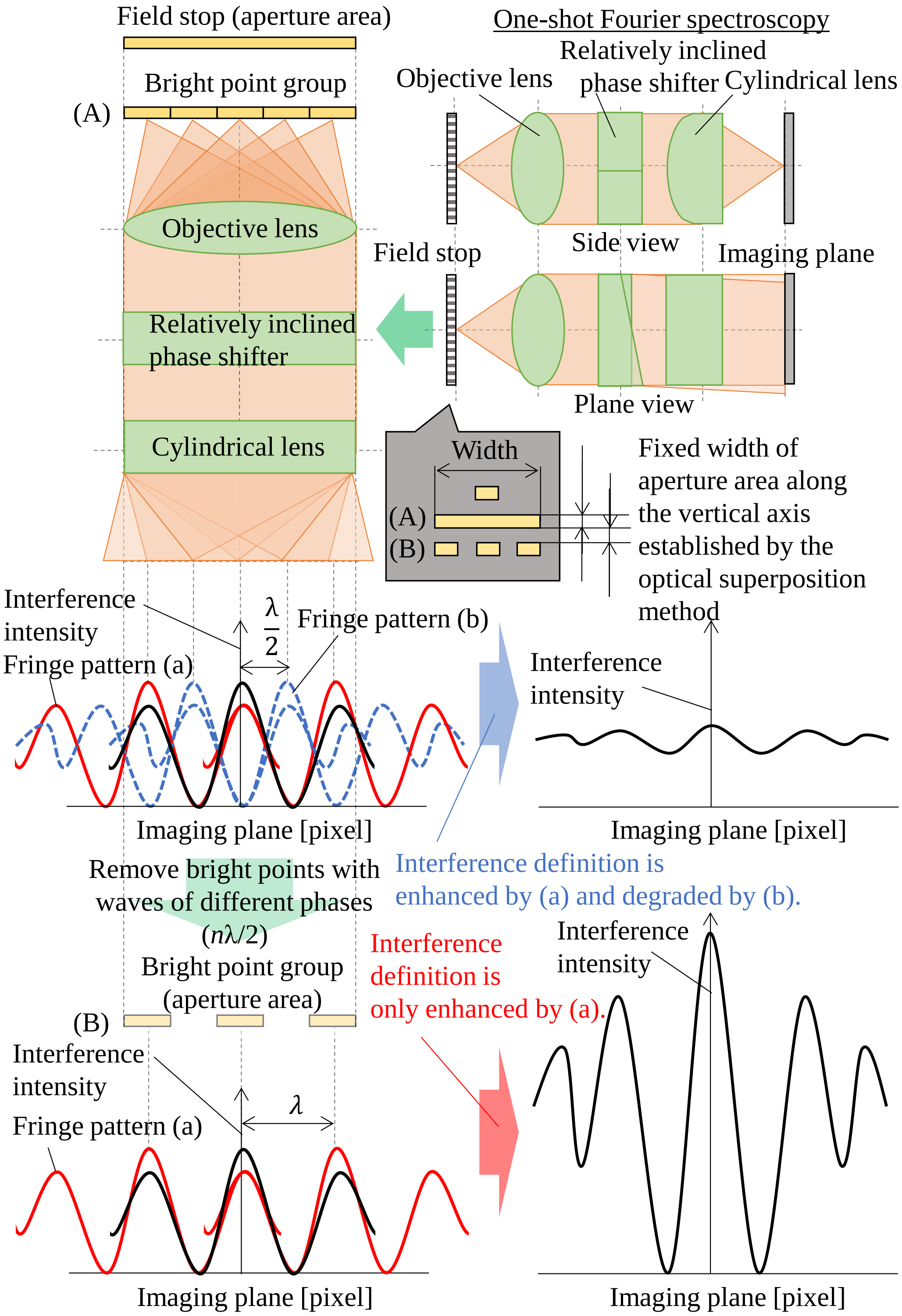

Figure 22 Schematics showing the principle of the superimposing interferogram method using the multi-slit array, related interferograms, and the interference definition at the aperture of each bright point of the multi-slit array

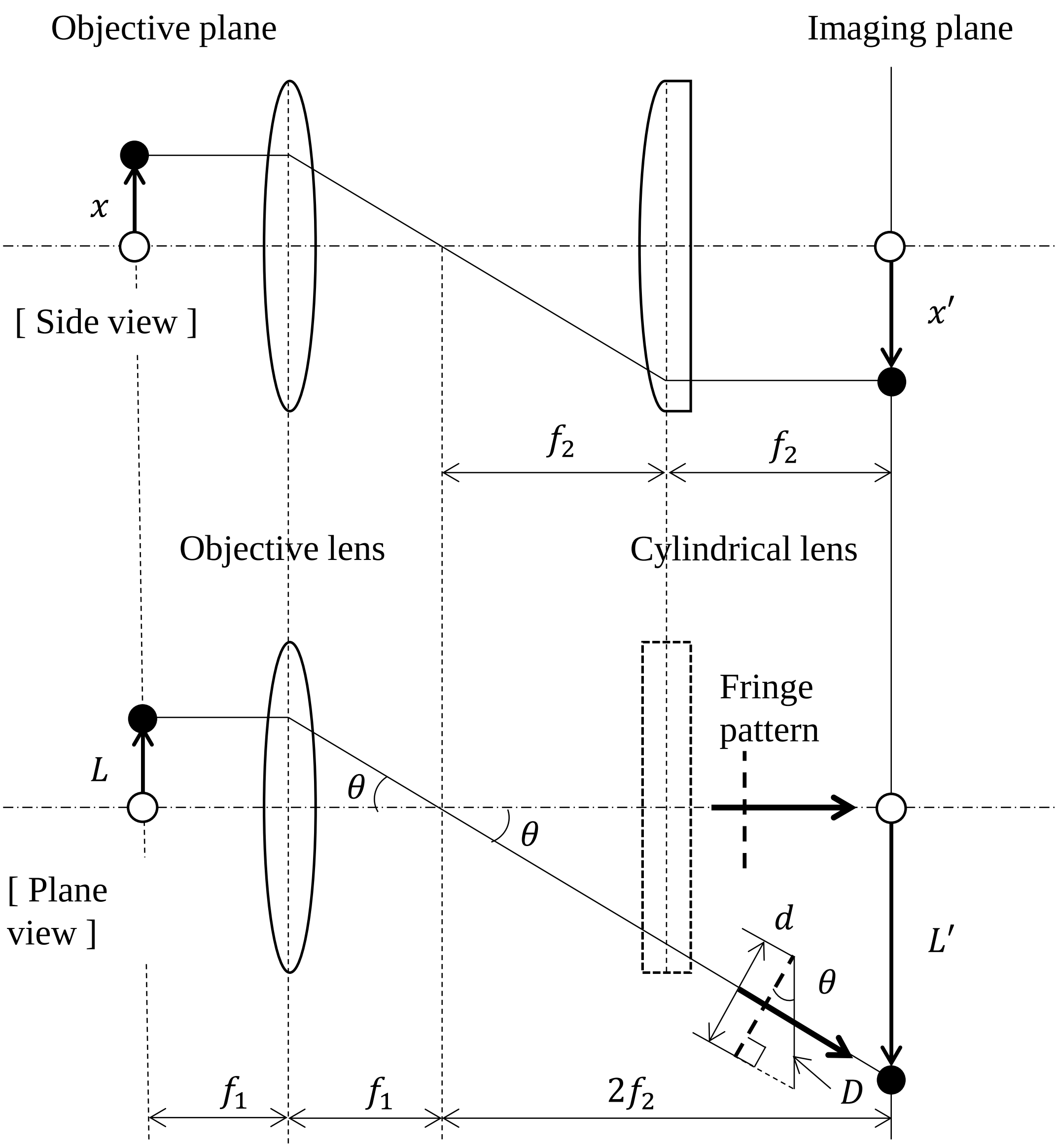

Figure 23 Schematic of the optical system for one-shot Fourier spectroscopy (using a spatial-phase-shift interferometer) to calculate the projection ratio of the grating

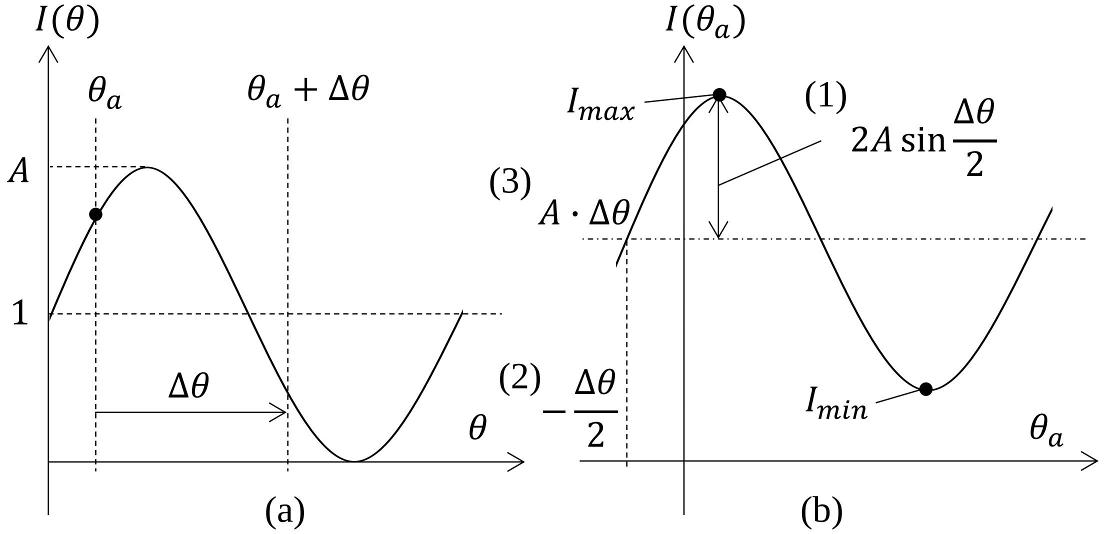

Figure 24 (a) Waveform of the interferogram and (b) superimposed interferogram obtained using the proposed multi-slit array

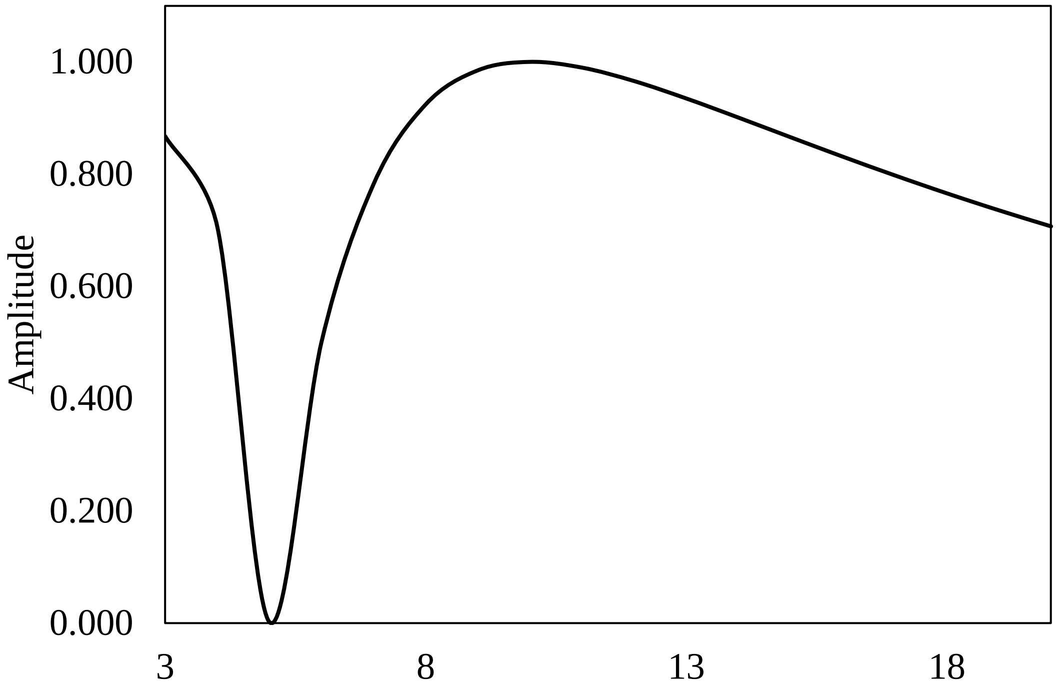

Figure 25 Amplitude of the intensity versus wavelength characteristic used in the design of the aperture of the field stop and the wavelength of the light source used in the experiments

3.3 *Verification experiment*

We performed experiments to verify our superimposing interferogram method using the multi-slit array and a one-shot Fourier spectroscopic imager. One-shot Fourier spectroscopy is based around the spatial-phase-shift interferometer and a simple optical system that includes only three lenses (an objective lens, a wedge and cuboid prism, and a cylindrical lens). The incident light emitted from the bright point on the field stop is collimated by the objective lens. A relatively inclined phase shifter, which is configured using the wedge glass and the cuboid glass, gives a continuous spatial phase difference between the upper and lower halves of the objective beams. The interferogram, which is focused along one direction (i.e., the horizontal direction) of the imaging plane by the cylindrical lens, can then be obtained spatially.

Figure 26 shows the optical system used for this verification experiment. A HeNe laser (GLG5360, NEC Corporation) was used as the light source and a complementary metal-oxide-semiconductor (CMOS) camera (STU-MBCM200U3V-NIR, OMRON Sentech Co., Ltd.) was used as a light-receiving device in the visible wavelength region. The pixel pitch was 5.5 μm and the number of pixels was 2,048 × 1,088 pixels. The focal length of the illumination lens was 60 mm, while that of the objective and imaging lenses was 50 mm. Using Eq. (11), the width of the field stop was calculated to be 15 μm when the optical magnification was the same size. In this experiment, the pinhole with a hole size of 15 μm was moved in 15-μm steps and the interferogram was sampled at each step to analyze the effect of the multi-slit array artificially. Figure 27 shows the results obtained using same optical system that was shown in Fig. 26 with a metal halide lamp (IMH-250, Sigma Koki Co., Ltd.) as a light source. At the corresponding blocked areas of the multi-slit array, the interferogram (gray graph) for which the phase is out by half a wavelength was compared with the interferogram (black graph) formed by the zero-point bright point, as shown in Fig. 26(a) and Fig.

27(a). Additionally, the interferograms at the corresponding aperture areas of the multi-slit array were formed at the same phase with the interferogram formed by the zero-point bright point, as shown in Fig. 26(b) and Fig. 27(b). The orange graphs were calculated by adding two interferograms at the corresponding aperture areas of the multi-slit array and the interferogram of the zero-point bright point. The green graphs were calculated by adding the interferogram at the corresponding aperture areas of the multi-slit array and the interferogram of the zero-point bright point. The blue graphs were formed using only the interferograms of the zero-point bright point. The interferograms of the green and orange graphs were obtained by using the neutral density filter to cut the light intensity by 50%. With increasing numbers of superimposed interferograms, sensitivities of 117, 243, and 324 and interference definitions of 128, 265, and 346 were obtained in Fig. 26. As shown in Fig. 27, with increasing numbers of superimposed interferograms, sensitivities of 81, 159, and 234 and interference definitions of 27, 48, and 60 were obtained. The dark current noise of the camera was present in these interferograms. The errors of the interference definition and the sensitivity between the predicted value and the measured value should be less than 100 when calculated using the mean squared error (MSE) method because the maximum amplitude of the dark current was 10. We then confirmed that every error in the sensitivity and the interference definition in the green graphs and the orange graphs in Fig. 26 and Fig 27 was less than 100. These errors were thus within the scope of the assumption. Therefore, for the added interferograms for which the phase differences are $m\lambda$ (where $\lambda$is the wavelength of the light source used; in the case of a white light source, λ is equal to λ_c), we confirmed increases in the sensitivity and the interference definition in Figs. 26(b) and 27(b) in accordance with the number of interferograms added at the corresponding aperture area of the multi-slit array, thereby verifying the multi-slit principle for both monochromatic and white light.

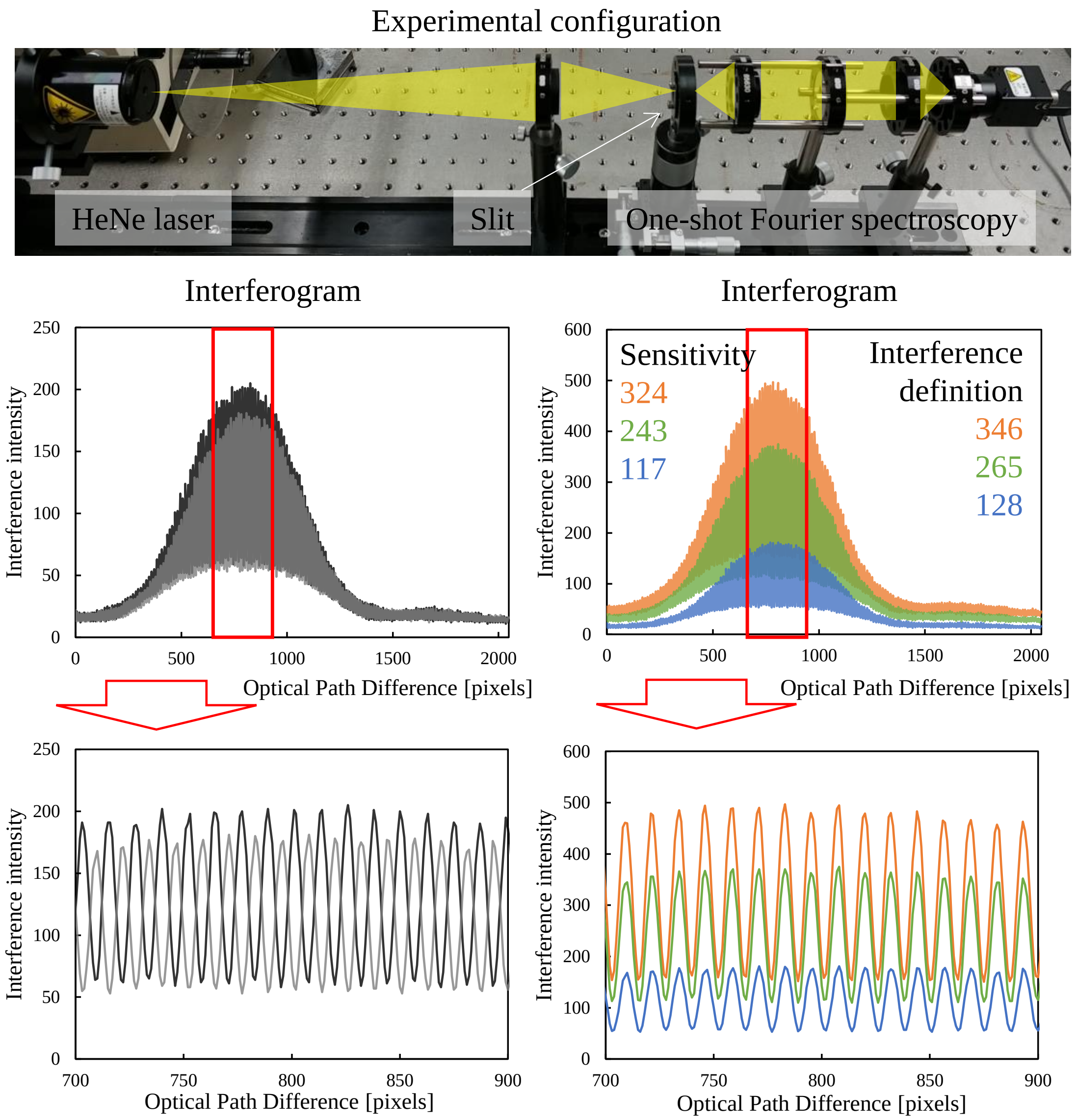

Experimental configuration

Interferogram

Interferogram

(a)

(b)

Figure 26 Verification of the principle of the superimposing interferogram method performed by moving the pinhole with monochromatic light

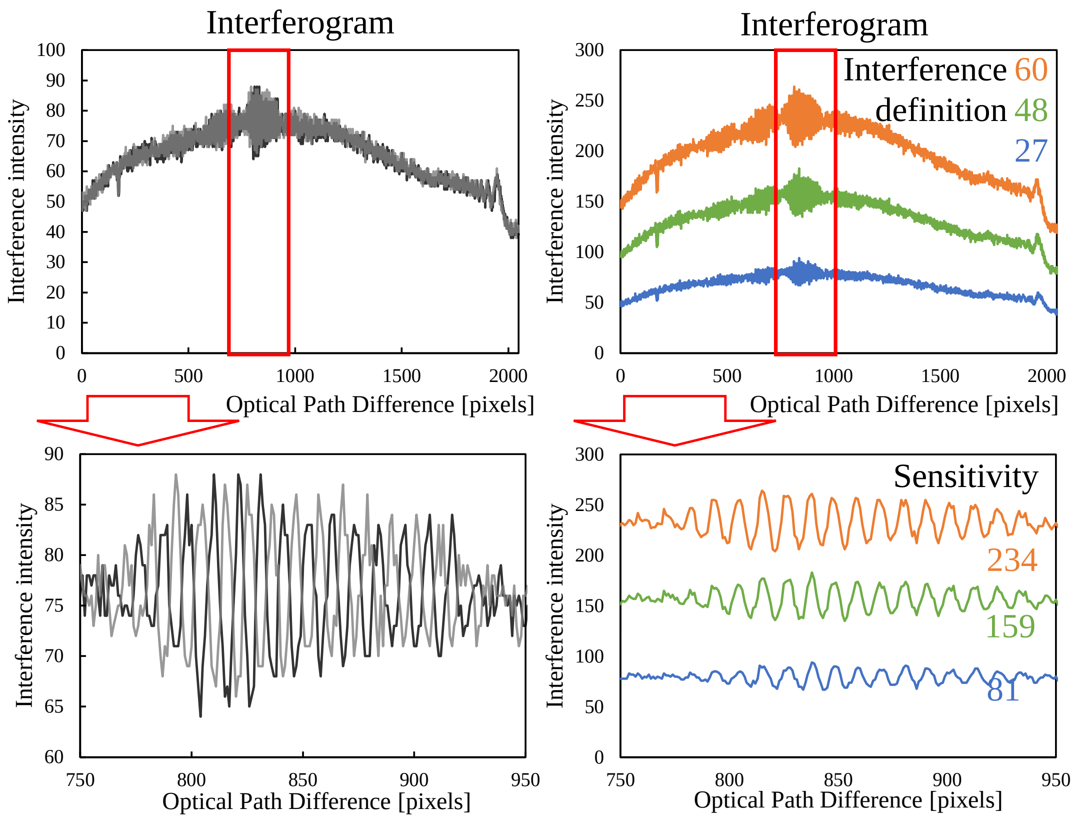

(a) (b)

Figure 27 Verification of the principle of the superimposing interferogram method performed by moving the pinhole with white light

3.4 Highly sensitive long-wavelength infrared Fourier spectroscopic imager

Using a prototype of the multi-slit array, we performed verification experiments for the superimposing interferogram method in the visible and mis-infrared regions.

In the experiment using visible wavelengths, the focal length of the illumination lens was 60 mm, whereas that of the objective and imaging lenses were 50 mm. The same CMOS camera and light source (the metal halide lamp) used in experiments to obtain Figs. 26 and 27 were used in the optical system to obtain Fig. 28. The width of the multi-slit array along the horizontal direction was 15 µm and the number of aperture areas along each line were set at one slit (blue plot), three slits (green plot), and five slits (orange plot); see center right diagrams of Fig. 28. The interferograms of the green and orange plots were obtained using the neutral density filter to reduce the light intensity by 50%. The width of each of the multi-slits in the vertical direction was calculated to be 5.5 µm using the optical superposition method. A multi-slit array was made from a Si wafer with a thickness of 300 µm. The apertures (15 × 5.5 µm) were fabricated by dry etching. From the expanded graph (see Fig. 28, center left), we obtained the coherent waveforms from the interferograms detected from the one-, three-, and five-aperture multi-slit arrays. Furthermore, when more apertures were used, greater improvements were obtained in the spectroscopic characteristics, the sensitivity, and the interference definition. With increasing number of apertures, sensitivities of 95, 142, and 184 and interference definitions of 17, 37, and 50 were obtained.

Additionally, we compared the full-width at half-maximum values in the spectroscopic characteristics of the one-shot Fourier spectroscopic imager and those of the wavelength dispersive spectrometer (PMA-11, Hamamatsu Photonics K.K.). The spectroscopic characteristics of the light source were obtained using the wavelength dispersive spectrometer (Fig. 28, top image). The spectral peaks of the metal halide lamp within the 400–500-nm range were not detected using the one-shot Fourier spectroscopic imager because of axial chromatic aberration. The full-width at half-maximum values at approximately 550 nm and 580 nm were 10.4 nm and 11.5 nm for the one-shot Fourier spectrometer and 5.27 nm and 9.02 nm for the dispersive spectrometer, respectively. The full-width at half-maximum values for the one-shot Fourier spectrometer were broader than those of the dispersive spectrometer because the wavelength resolution of the one-shot Fourier spectrometer was 8.3 nm. Increasing the angle of the inclined wedge prism improves the wavelength resolution.

In considering the error, processing the accuracy of the multi-slit arrays enables a quantitative evaluation of the experimental results. However, the aperture width has an error of approximately +1 μm, based on the Si etching rate when the multi-slits are produced. For example, when we used a multi-slit with an aperture width of 43 μm that was calculated assuming a central wavelength of 10 μm and a multi-slit having an error of +1 μm in its width from processing, light with a wavelength that was 2.3 % longer than 10 μm passed through the aperture and formed the interferogram, which was then superimposed on the other interferogram formed by the 10-μm wavelength light. Therefore, the interference definition and the sensitivity deteriorated by 12.7 % and 20.7 % given an error in processing accuracy of approximately +1 μm. And the interference definition deteriorated by 23 % given an error in the alignment of the multi-slit array on the optical system. The errors in sensitivity and interference definition of the experimental result (Fig. 28) were maximum 9 % and 34 %, respectively. We confirmed that these errors were less than assumed error and were therefore within the scope of the assumption. We also confirmed the proposed principle and demonstrated the effect of the multi-slit array when applying the superimposing interferogram method. Because the slit holder had some misalignments in terms of angle θ_y and the x axis with respect to the optical axis, the center aperture of the multi-slit array was not on the zero-point of the optical axis. Additionally, the error of half bandwidth will be improved by 20 % after the analytical procedure is improved. Therefore, the sensitivity and interference definition did not improve by exactly three-fold and five-fold, respectively, following increases in the number of aperture areas.

In experiments using long-wavelength infrared wavelengths, we performed spectroscopic measurements using a prototype of a bean-sized long-wavelength infrared spectroscopic imager based on the one-shot Fourier spectroscope, a prototype multi-slit array evaporated with Au to remove long-wavelength infrared light in the blocked area, a microbolometer camera (Quark2, FLIR Systems, Inc.), a Kanthal filament light source (EK3430, Helioworks Inc.), and a band-pass filter (BP-10500-780, Spectrogon). The number of pixels was 336 × 256 pixels and the pixel pitch was 17 μm. The focal length of the two illumination lenses was 25 mm whereas that of the objective and imaging lenses was 3.32 mm. We compared the sensitivity and the interference definition for the different aperture numbers for the multi-slit array. Figure 29 shows the optical system, the prototype long-wavelength infrared spectroscopic imager (Nalux Co., Ltd.), and the results of the experiments obtained by surveying a number of the 30 data points. We obtained the coherent waveform from the interferograms obtained with the three multi-slit arrays (Fig. 29). With increasing number of apertures, sensitivities of 98, 127, and 151 and interference definitions of 8, 21, and 23 were obtained. That is, we also confirmed improvements in both for the spatial-phase-shift interferometer when using our method for long-wavelength infrared wavelengths.

Additionally, we compared the full-width at half-maximum values of the spectroscopic characteristics of the one-shot Fourier spectroscopic imager with those given in the specification sheet of the band-pass filter. The values obtained from the three- and five-slits spectrometer were 1,262 nm and 1,193 nm, respectively, whereas that from the band-pass filter's specification sheet was 780 nm. The wavelength resolution of the prototype one-shot Fourier spectrometer was 511 nm. The full-width at half-maximum value of our spectrometer was broader than the value from the band-pass filter's specification sheet because the spectroscopic characteristics include camera noise arising from a lack in sensitivity. We obtained the same full-width at half-maximum value as that on the band-pass filter's specification sheet by installing a 17-slit multi-slit array in the spectrometer.

Thus, there is a need to consider not only every type of error caused by camera noise but also spherical aberrations and the processing accuracy of the multi-slit arrays to enable a quantitative evaluation of the experimental results. As described previously, if the five-slit multi-slit array had a processing accuracy error of approximately +1 μm, the errors in the sensitivity and interference definition would be 5.1 % and 11.8 % (see Fig. 29). This would be the case if we had used a five-slit multi-slit array with an aperture width of 43 μm and the objective lens had a guaranteed condensing property on a 1-mm × 0.3-mm area of the objective plane, corresponding to the multi-slit pattern area. However, the three- and five-slit patterns were located outside this guaranteed area. Therefore, the sensitivity and the interference definition did not attain the three- and five-fold increases in these interferograms because of spherical aberration effects. In addition, because the spectroscopic imager had six degrees of freedom and was set by hand, the plane of the pattern area on the multi-slit array and the plane of the light receiving device were not parallel. Moreover, because both the pattern axis of the multi-slit array and the optical axis were not vertical, the distribution of the light intensity was not equal on the light-receiving device. Additionally, the error of half bandwidth in the spectroscopic characteristics of band-pass filter is caused by the lack of image gradation. The half bandwidth will be improved by 17.8 % after the gradation is changed from 8-bit to 16-bit. Therefore, we did not attain the n-fold increases in sensitivity and interference intensity when we used the n-aperture multi-slit array.

From the spectroscopic characteristics (Fig. 29), the spectral peaks appeared to shift toward longer wavelengths as the number of apertures increased. The spectral band becomes narrower with increasing aperture number because the central wavelength, which determines the aperture width of the multi-slit array, is extracted more strongly from the incident light. In viewing the interferograms (Figs. 28 and 29), the interferogram from the five-slit array has a long waveform comprising light and dark variations similar for monochromatic light. Therefore, a strong spectrum peak at 10 μm (Fig. 9) was detected and the full width at half-maximum value was narrower because the multi-slit array was designed based on the central wavelength of 10 μm. The full width at half-maximum value of white light thus narrows and reaches the same value as that for monochromatic light. In future work, we intend to study this band narrowing using our method and then propose an optimal design method for the multi-slit arrays required for each interferometer, considering their different optical systems, to mitigate band narrowing and also to enhance the sensitivity and interference intensities of the spatial-phase-shift interferometers with broadband wavelengths.

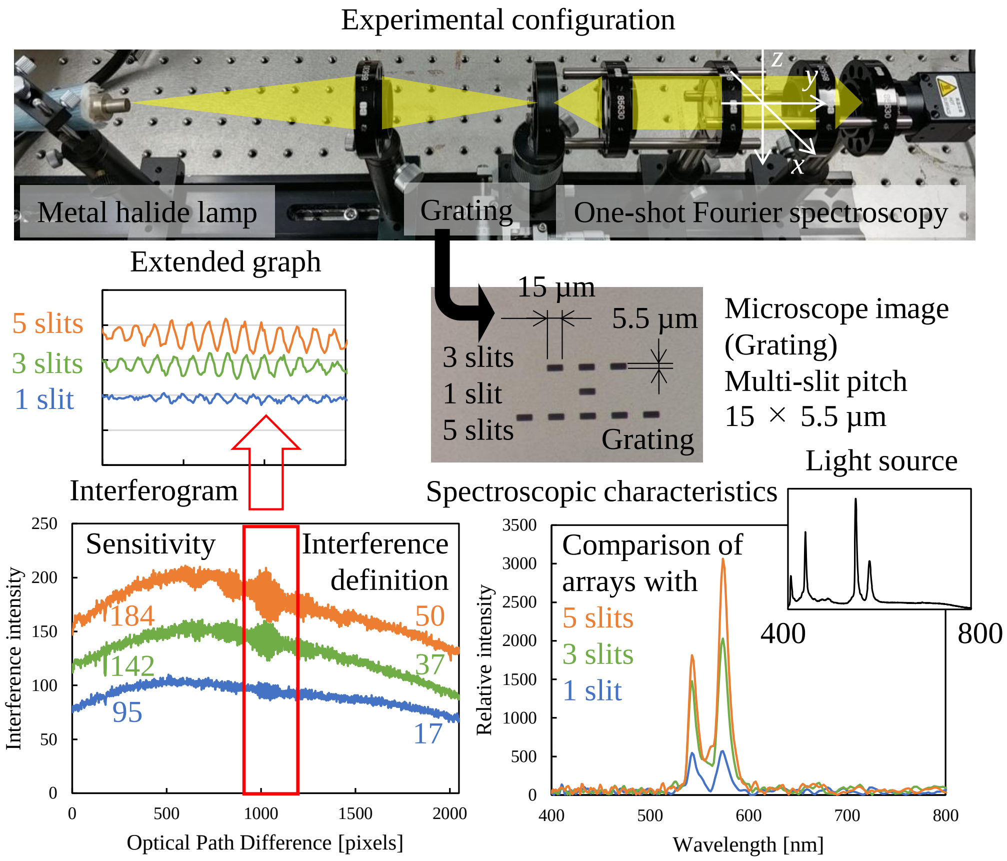

Figure 28 Verification of the principle of the superimposing interferogram method performed using a multi-slit array with white light

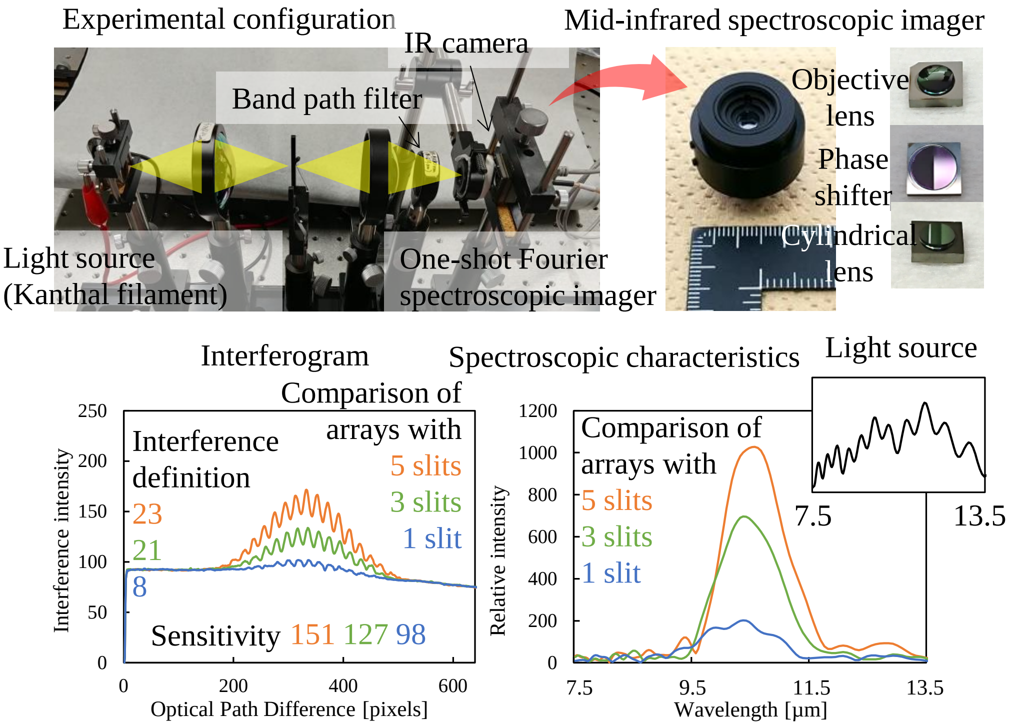

Figure 29 Demonstration of the feasibility of the superimposing interferogram method using a multi-slit array and a long-wavelength infrared spectrometer with a white light source

3.5 Band narrowing phenomenon

We found the widened coherence length on the interferogram and then discovered the band narrowing phenomenon by increasing the aperture of the multi-slit array in Fig. 29. As shown in Fig. 30, a light shielding plate was set on the multi-slit array on the basis of the superimposing interferogram method and we performed a verification experiment of this phenomenon with a light source (model: EK3430, manufacturer: Helioworks Inc.). The widths of the aperture area on the light shielding plate were 480, 960, and 1920 μm. These widths corresponded to apertures on the multi-slit; i.e., 5, 11, and 22. We confirmed that the band of spectral characteristics narrows as the aperture increases.

The band narrowing phenomenon is explained by the conceptual diagram of Fig. 31. When light having a wavelength λ_c passes through the green aperture, the green interferogram is produced. The multi-slit array is designed using λ_c. Then, when the light of wavelength λ_c passes through the blue and red apertures, the blue and red interferograms overlapping the green interferogram are produced. However, we use white light having multiple wavelengths. Therefore, if light having different wavelengths λ_1 passes through the aperture designed using λ_c, the phases are shifted by each aperture and reversed with respect to each other. Thus, only the wavelength used in the design of the aperture is extracted and the interferogram has a function like that of a band-pass filter. The wavelength λ_1 whose phase on the amount m of aperture is opposite the phase of the waveform from the central aperture can be calculated using Eq. (16). This wavelength λ_1 is on the full width at half maximum.

$$\frac{\lambda_1}{2} = m|\lambda_1 - \lambda_c| \tag{16}$$

When light with a wavelength λ passes through an aperture designed using the wavelength λ_c and the aperture is 1 on the multi-slit array, the interference intensity I_λ is calculated using Eq. (17).

$$\alpha = \frac{\lambda_c}{\lambda}$$

$$I_\lambda(\theta_\alpha) = 2A\sin\frac{\pi}{2}\sin\left(\theta_\alpha + \frac{\pi}{2}\right)\alpha + A\pi\alpha \tag{17}$$

When light with a wavelength λ passes through an aperture designed using the wavelength λ_c and the aperture is m on the multi-slit array, the interference intensity I_λ is calculated using Eq. (18). The amplitude A_λ of the interference intensity corresponds to Eq. (19).

$$mI_\lambda(\theta_\alpha) = 2A\sin\frac{\pi}{2}\alpha\frac{\sin(m\pi\alpha)\cos(\theta - m\pi\alpha)}{\sin(\pi\alpha)} + mA\pi\alpha \tag{18}$$

$$A_\lambda = 2A\sin\frac{\pi}{2}\alpha\frac{\sin(m\pi\alpha)}{\sin(\pi\alpha)} \tag{19}$$

When the incident light has the wavelength λ_c and the aperture is m, the amplitude A_{λ_c} is calculated using Eq. (20).

$$A_{\lambda_c} = 2mA \tag{20}$$

The ratio of the amplitude between A_λ and A_{λ_c} is thus calculated using Eq. (21).

$$\frac{A_\lambda}{A_{\lambda_c}} = \left|\frac{1}{m}\sin\frac{\pi}{2}\cdot\frac{\lambda_c}{\lambda}\cdot\frac{\sin m\pi\frac{\lambda_c}{\lambda}}{\sin\pi\frac{\lambda_c}{\lambda}}\right| \tag{21}$$

When this ratio of the amplitude is 0.5, the wavelength λ is on the full width at half maximum of the relative intensity from the multi-slit array designed using the wavelength λ_c.

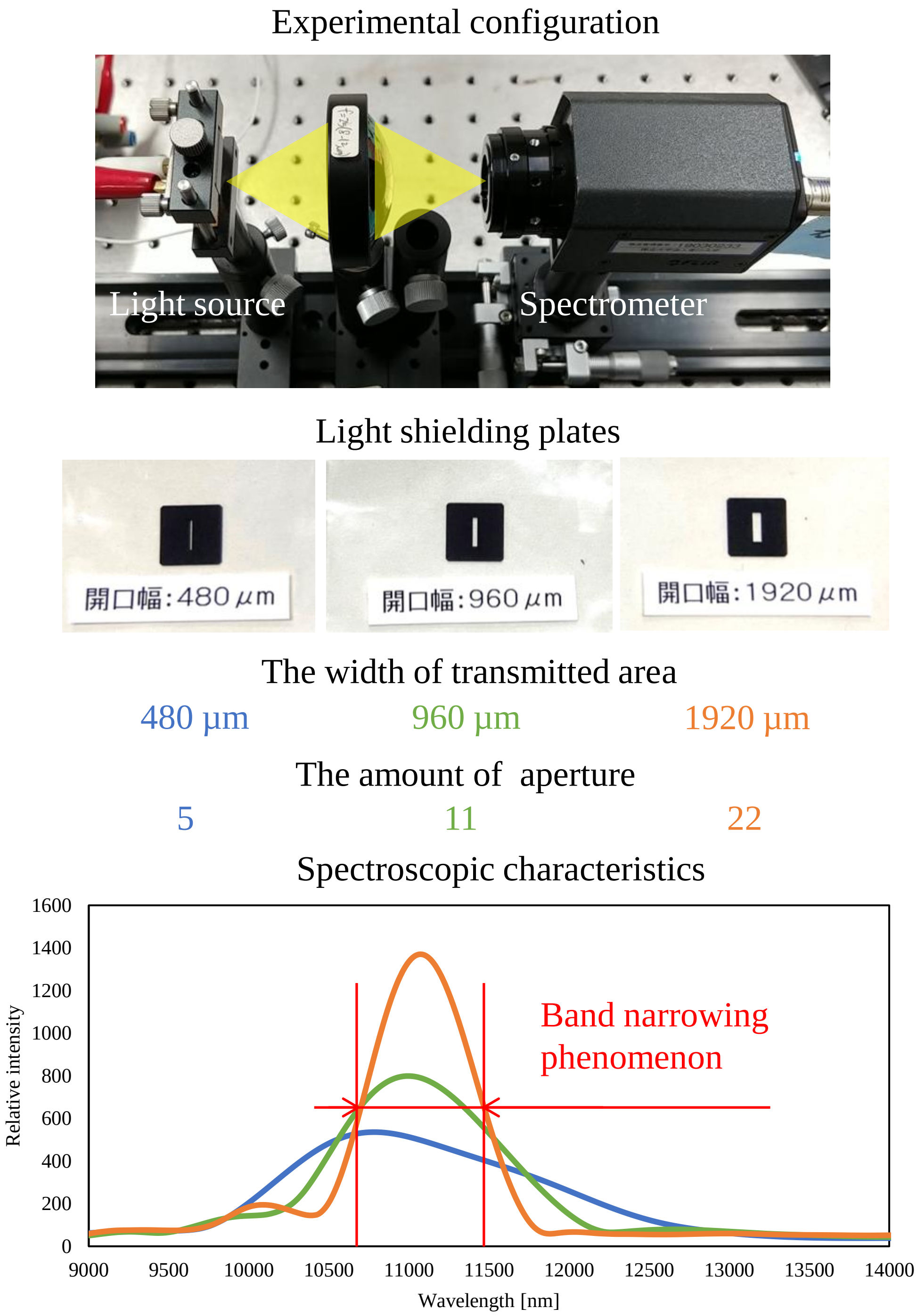

Figure 30 Verification experiment of the band narrowing phenomenon

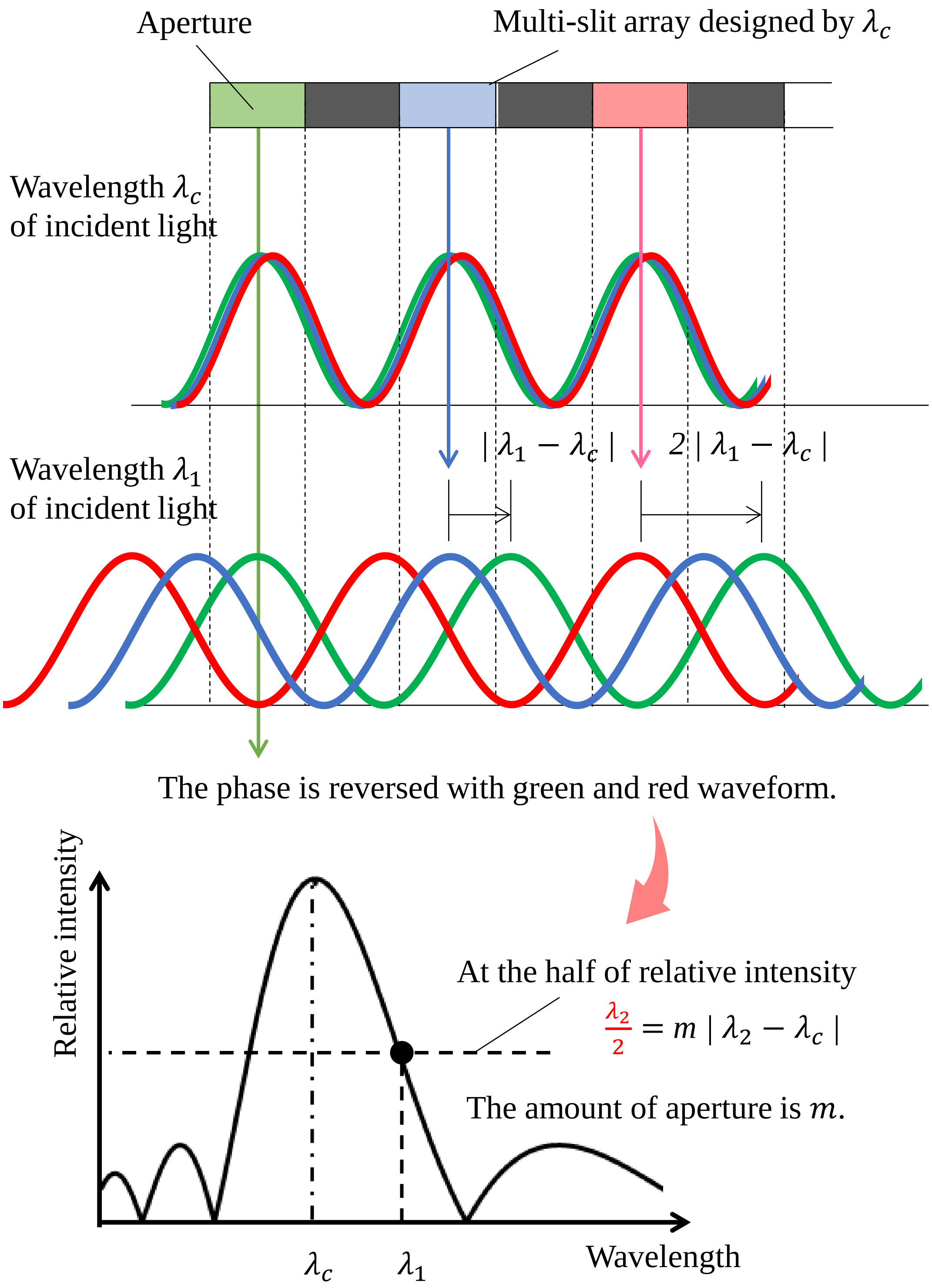

Figure 31 Conceptual diagram of the band narrowing phenomenon

3.6 Wavelength-splitting-type multi-slit array

We propose a wavelength-splitting-type multi-slit array that improves the light efficiency of only a desired wavelength using the band narrowing phenomenon and removing light at unnecessary wavelengths. This method improves the wavelength resolution of a spectrometer in a pseudo manner by intentionally narrowing the band at a specific wavelength and generating a plurality of steep spectral peaks. We then detect the spectral characteristics having a minute difference in peak wavelength and discriminate the component having a peak position at a close wavelength, such as a gas, as shown in Fig. 32.

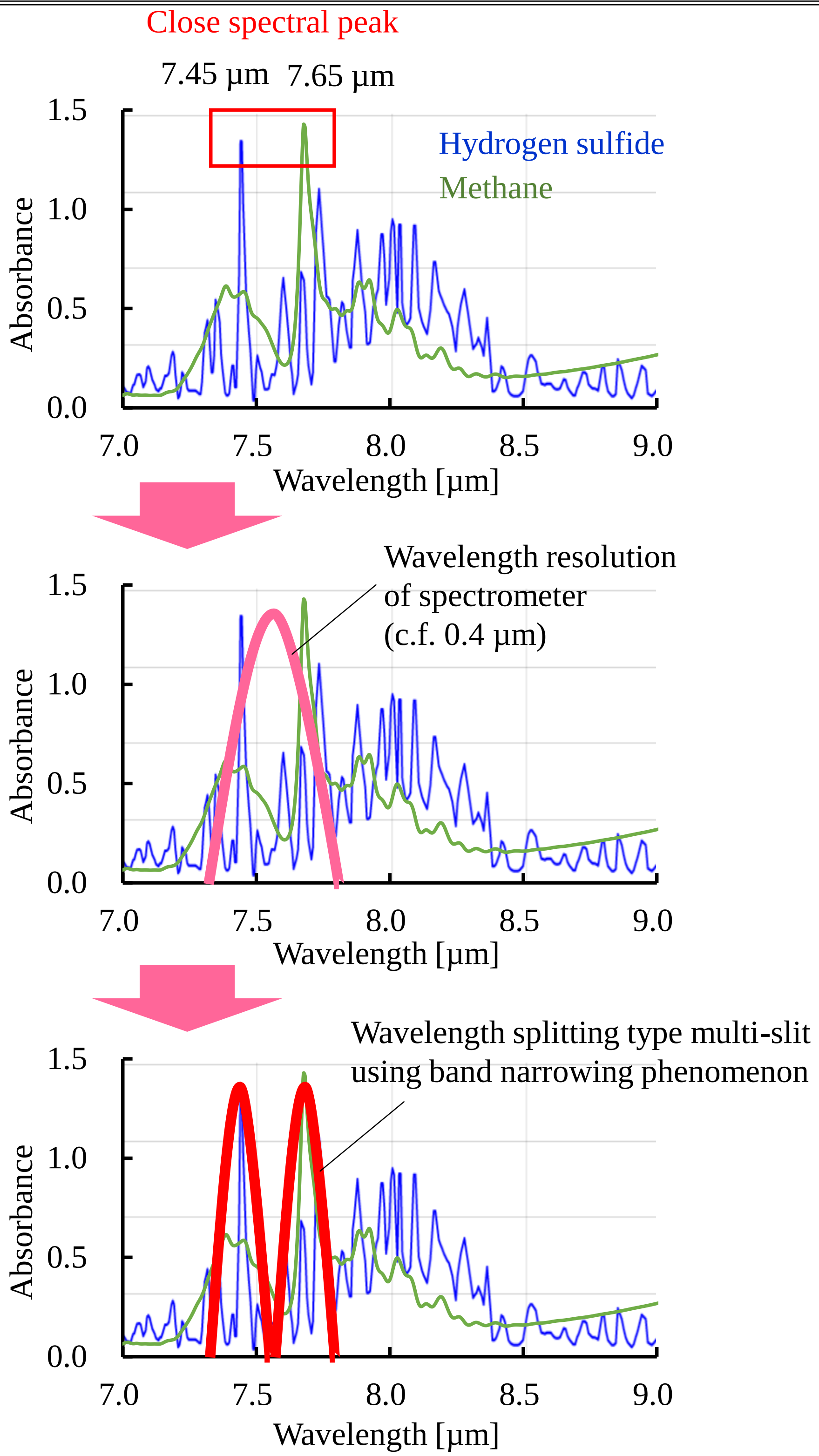

Figure 32 Conceptual diagram of the effect of the wavelength-splitting-type multi-slit array

3.7 Large-band-width multi-slit array

We produced a prototype of a large-bandwidth multi-slit array for solving the band narrowing phenomenon and measuring across a wide band. First, as shown in Fig. 33, we decided the desired measurement band from λ_1 to λ_m. One of the apertures was designed using λ_1. The next aperture was designed using λ_2, whose amplitude ratio with λ_1 is 0.5. We horizontally lined up m types of apertures to the end of the desired measuring band, which is λ_m. We then realized a large band of spectroscopic characteristics for spectral measurement.

Here, we set the wavelength band from 7 to 14 µm. The wavelength λ_1 used in calculating the width of the aperture was thus set to 7 µm. The next aperture was calculated using the wavelength λ_2, which had an amplitude ratio with λ_1 of 0.5, according to Eq. (22). We prepared eight aperture widths, namely 7, 7.8, 8.6, 9.6, 10.7, 11.9, 13.2, and 14.6 µm, as shown in Fig. 34.

$$\lambda_m = \frac{m\lambda_{m-1}}{m - 0.5} \tag{22}$$

The verification experiment conducted using the prototype of the large-bandwidth multi-slit array did not have relative intensity of 9.6 (Fig. 34(a)) and 10.7 (Fig. 34(b)) µm at the central aperture. The reason is probably that wavelengths on both sides deteriorated the wavelength of the central aperture because the ratios of the amplitudes on the two wavelength sides with the wavelength of the central aperture are 0.5 which is same definition with the calculation of coherence length [96]. We simulated the interferogram and the spectroscopic characteristics of the prototype large-bandwidth multi-slit array as shown in Fig. 35. We could confirm the edge waveform of the central aperture (wavelength: 10.6 µm) and waveforms of neighboring apertures (wavelength: 11.8 µm and 9.7 µm) are reversed and detect same phenomenon with result of verification experiment. Additionally, we simulated them after the central waveform is moved with $\frac{\lambda}{2}$ as shown in Fig. 36. We confirmed the waveform of central and neighboring apertures were reversed at the center of 10.6 μm waveform and detected the spectral peak at 9.7μm and 11.8 μm. Then, we simulated them after the waveform is moved by $\frac{\lambda}{4}$ as shown in Fig. 37. We confirmed the waveforms are fitted and detected large-bandwidth spectrum (10-12 μm). In the future work, we should clarify the phenomenon and optimize the large-bandwidth multi-slit array. Incidentally, when merging all horizontal 10 lines with aperture areas (Fig. 34(a) and Fig. 34(b)), we confirmed the large-band spectroscopic characteristics as shown in Fig. 38. The short and long wavelengths could not be detected because of the anti-reflection coating of the lenses in the range from 8 to 12 μm.

Finally, using this prototype of a large-bandwidth multi-slit array and one-shot Fourier spectrometer, the absorption peak of ethanol aqueous solution was obtained as shown in Fig. 38 with a light source (model: EK3430, manufacturer: Helioworks Inc.). The concentrations of ethanol aqueous solution were 2, 5, 25, and 50 mg/dl. The one-shot Fourier spectrometer had a wavelength resolution of 0.38 μm, optical path length (OPD) of 262 μm, and angle of the wedge prism of 1.4 deg. We obtained a high correlation coefficient in this experiment as shown in Fig. 39.

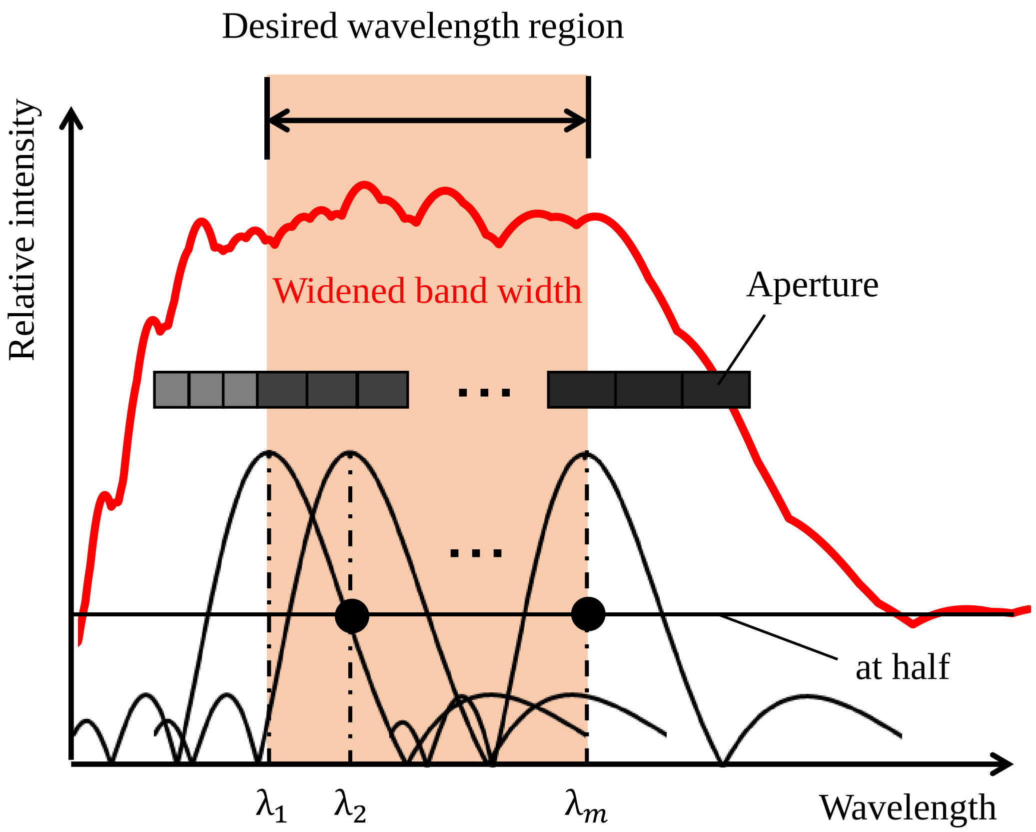

Figure 33 Conceptual diagram of the design guideline for a large-bandwidth multi-slit array

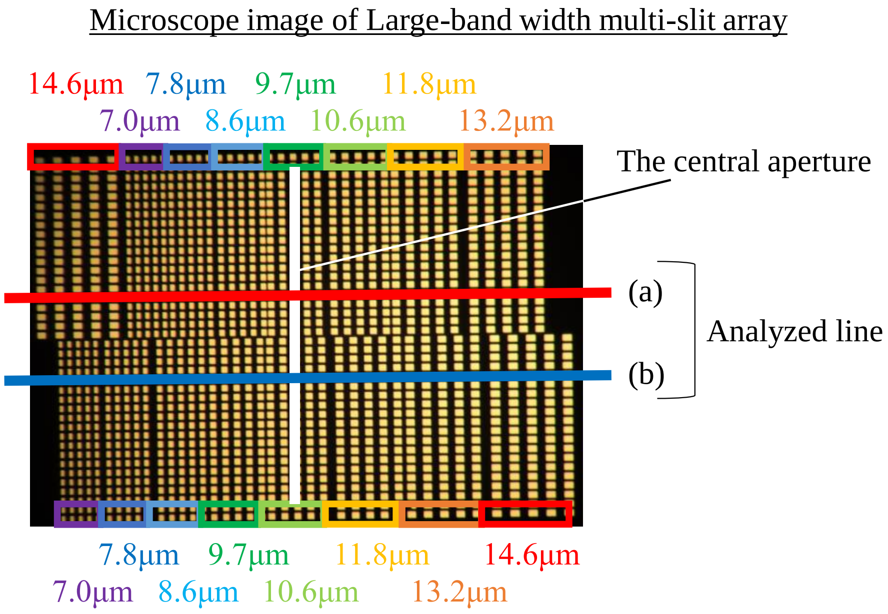

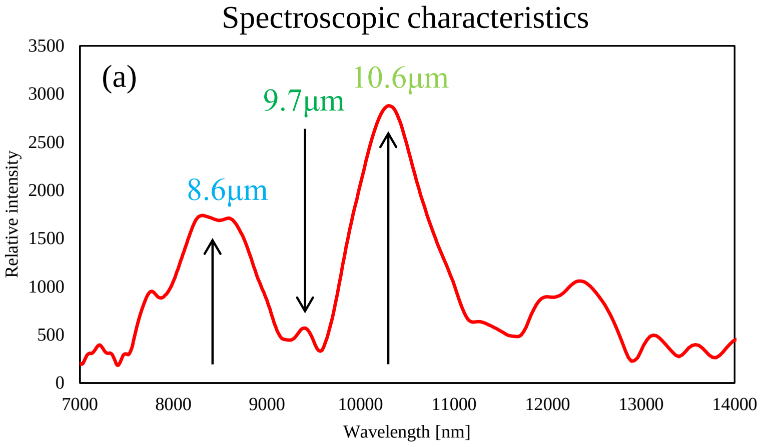

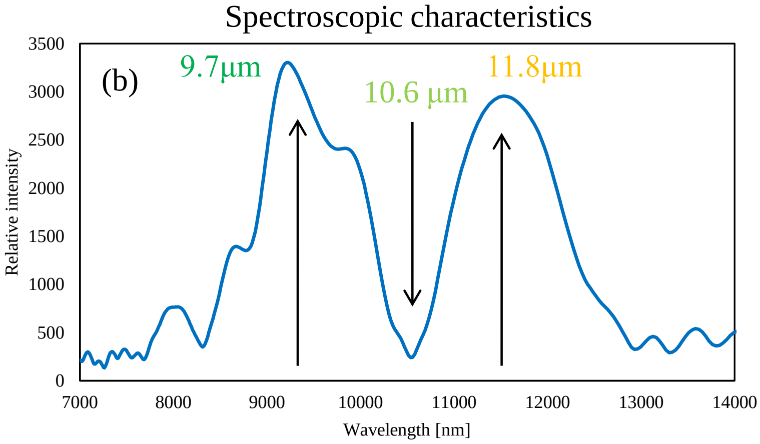

Figure 34 Result of the verification experiment of the prototype large-bandwidth multi-slit array

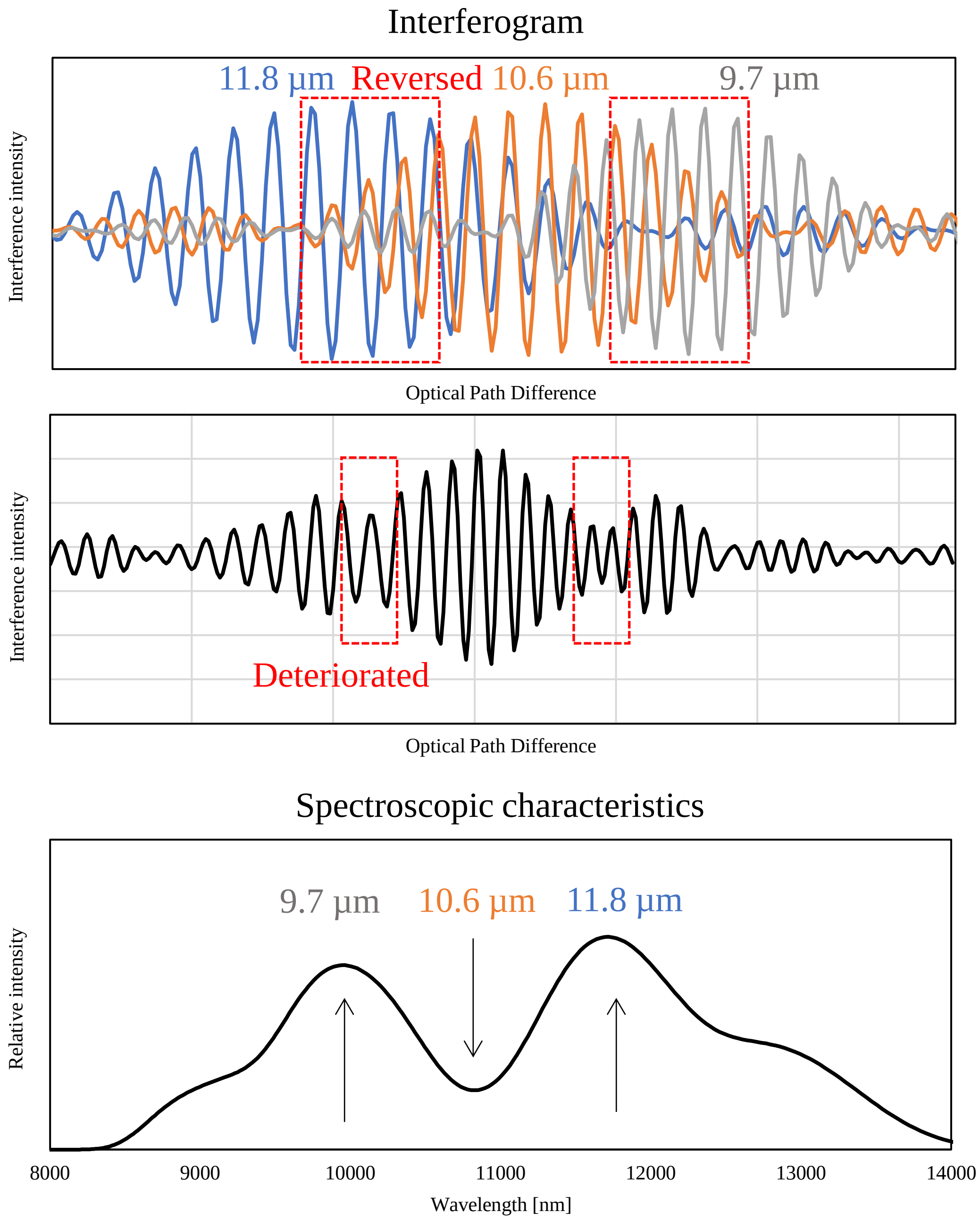

Figure 35 Simulation of interferogram and spectroscopic characteristics used the prototype large-bandwidth multi-slit array

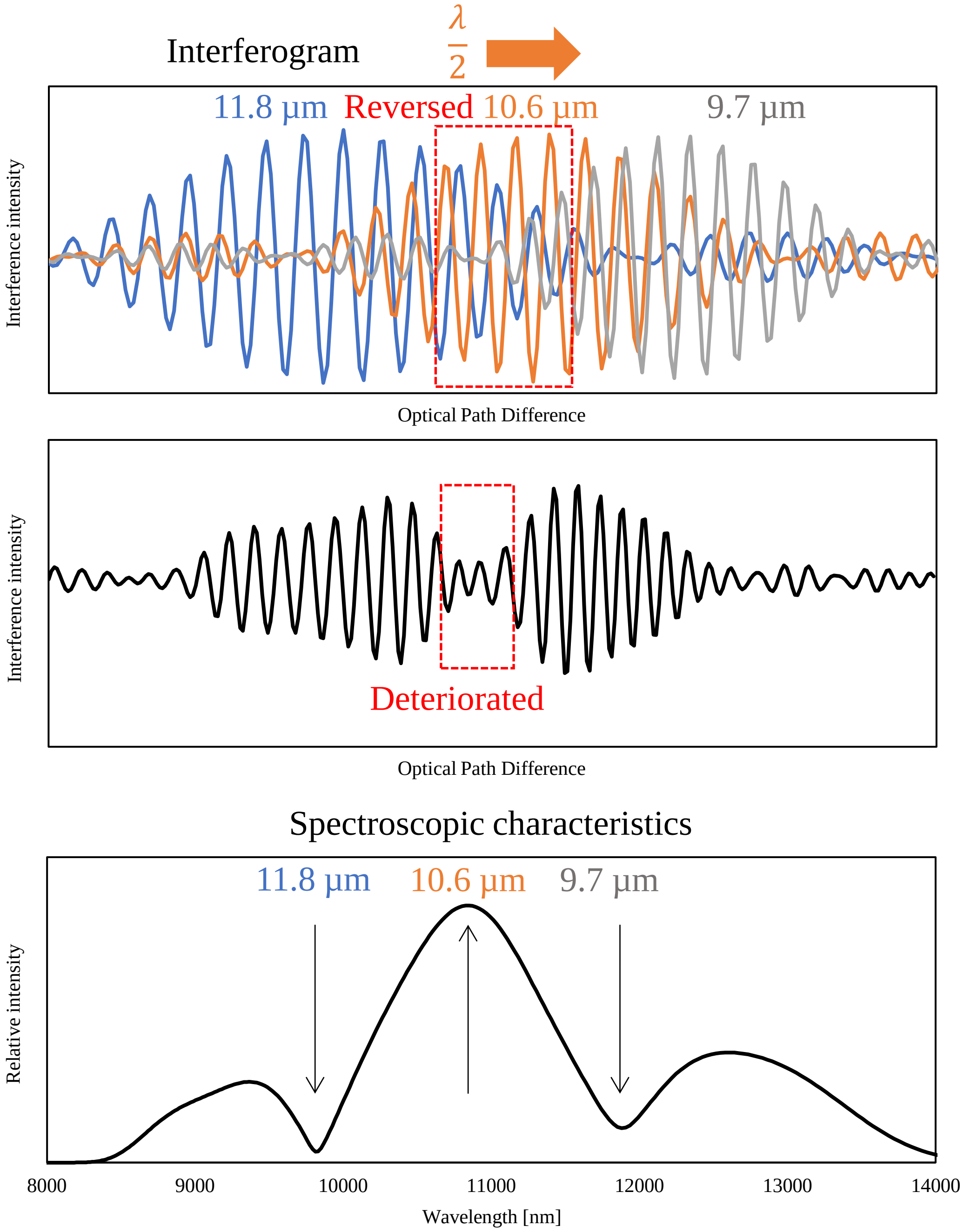

Figure 36 Simulation of interferogram and spectroscopic characteristics used the prototype large-bandwidth multi-slit array whose central apertures (wavelength: 10.9 μm) are moved with $\frac{\lambda}{2}$

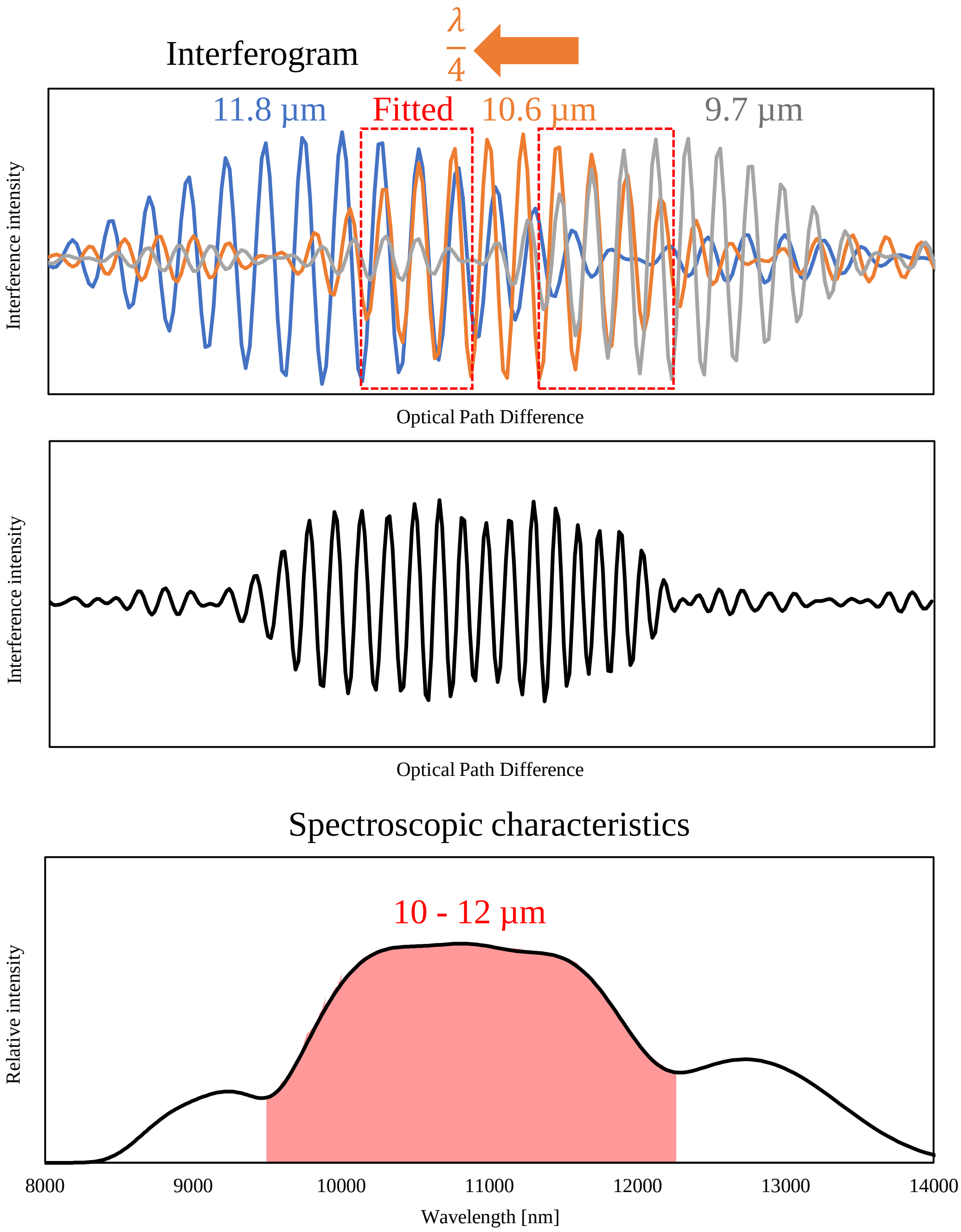

Figure 37 Simulation of interferogram and spectroscopic characteristics used the prototype large-bandwidth multi-slit array whose central apertures (wavelength: 10.9 µm) are moved with $\frac{\lambda}{4}$

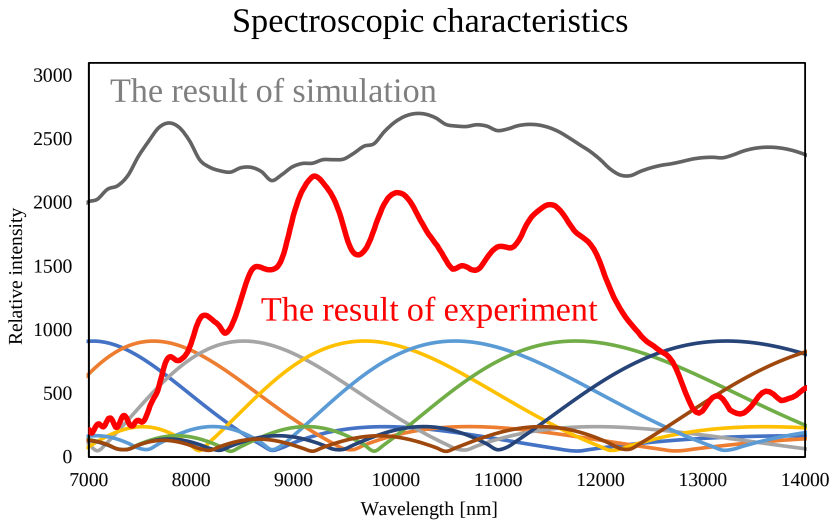

Figure 38 Result of merging lines

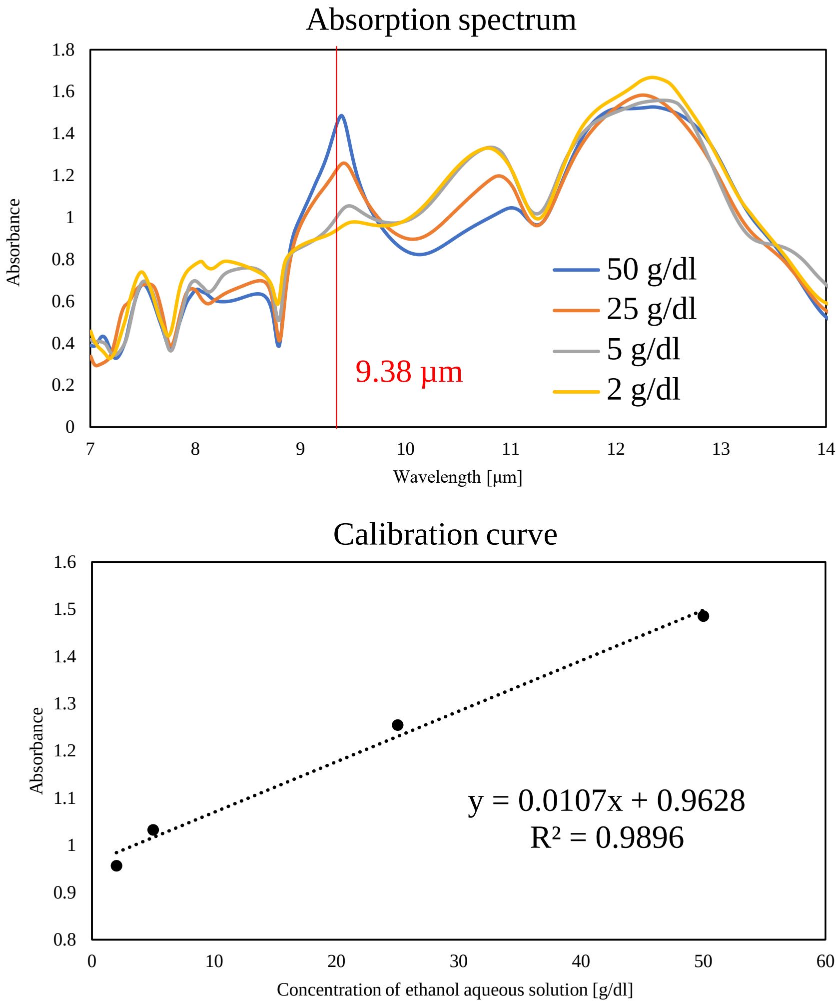

Figure 39 Result of component measurement (ethanol aqueous solution)

3.8 Summary

We proposed a superimposing interferogram method that features a redesign of the conventional field stop of a spatial-phase-shift interferometer, specifically involving the use of a multi-slit array with more than one aperture area periodically spaced along the horizontal axis. Using monochromatic and white light, a pinhole, and a prototype multi-slit array, we demonstrated the principle of our method in the visible-light regime. Furthermore, using a bean-sized long-wavelength infrared spectroscopic imager that incorporated the multi-slit array as a spatial-phase-shift interferometer and a band-pass filter, we confirmed improvements in sensitivity, interference intensity, and spectroscopic characteristics in the long-wavelength infrared regime. We discovered and clarified the band narrowing phenomenon and proposed the wavelength-splitting-type multi-slit array and large-bandwidth multi-slit array. We obtained the absorption peak and a high correlation coefficient for ethanol aqueous solution.

CHAPTER 4

Point-one-shot Fourier spectroscopy for improved wavelength resolution, price reduction, and miniaturization

4.1 Abstract

I propose point-one-shot Fourier spectroscopy (diameter: 6 mm, thickness: 5 mm) for ear-clip-type non-invasive blood glucose sensors, at a low cost (approximately 1000 EUR). Point-one-shot Fourier spectroscopy is conducted using one objective lens and a camera. The objective lens is a spherical lens at the front side and a dual-axis wedge prism inclined along horizontal and vertical axes. An objective beam is collimated by the objective lens, with a difference in the optical path length created by the wedge prism. This device can be used to obtain 2D spatial fringe patterns. Conventional one-shot Fourier spectroscopy produces one-dimensional fringe patterns in the horizontal direction of the array device. The maximum optical path length is thus limited by the number of pixels along the horizontal line of the array device. However, our proposed point-one-shot Fourier spectroscopy device produces an interferogram with a longer maximum optical path compared with conventional devices because horizontal lines of different rows are connected by the same phase pixel. Spectroscopic imaging devices can thus be produced at low cost because low-resolution (e.g., 80 × 80 pixels) cameras can be used for spectroscopy.

4.2 *Principle*

The proposed point-one-shot Fourier spectroscopy uses only one objective lens and a camera, as shown in Figure 40. The objective lens is spherical at the front and a dual-axis (horizontal and vertical axes) inclined prism at the back. The objective beam is collimated by the objective lens and a difference in the OPD is created by the wedge prism. This allows us to obtain a 2D fringe pattern on the array device, by connecting the horizontal line and one of the different rows with the same-phase pixel. We thus obtain a longer maximum optical path length with point-one-shot Fourier spectroscopy than with conventional one-shot Fourier spectroscopy. An approximate calculation of the OPD (m'_p) is made using Eq. (23). The horizontal OPD per pixel is denoted ΔL_H and the vertical OPD per pixel is denoted ΔL_v. The number of horizontal pixels is H and the number of vertical pixels is V.

$$m'_p = \Delta L_H \times H + \Delta L_V \times V \tag{23}$$

We calculate the angle (θ) of the fringe pattern on the imaging plane using Eq. (24).

$$\theta = \tan^{-1} \frac{\Delta L_H}{\Delta L_V} \tag{24}$$

Using Eqs. (25)–(27), the precise OPD (m_p) is calculated. V_1 denotes the number of pixels vertically between the vertical same-phase pixel of the bottom fringe pattern and the vertical same-phase pixel of the top fringe pattern at the first connected dark line of the fringe pattern. H_1 denotes the number of pixels horizontally between the horizontal same-phase pixel of the top fringe pattern at the second connected dark line and the horizontal end pixel of the light and dark change line.

If V_1 is equal to V,

$$m_p = 2H + \Delta L_H \tag{25}$$

If V_1 is less than V,

$$V_1 = H \tan\theta$$

$$H_1 = \frac{V - V_1}{\tan\theta}$$

$$m_p = (2H + H_1) \times \Delta L_H \tag{26}$$

If V_1 is more than V,

$$H_1 = \frac{V}{\tan\theta}$$

$$m_p = (H + H_1) \times \Delta L_H \tag{27}$$

By contrast, one-shot Fourier spectroscopy has a single-axis (the horizontal axis) inclined prism. Therefore, the OPD of one-shot Fourier spectroscopy (m_o) is decided by Eq. (28).

$$m_o = H \times \Delta L_H \tag{28}$$

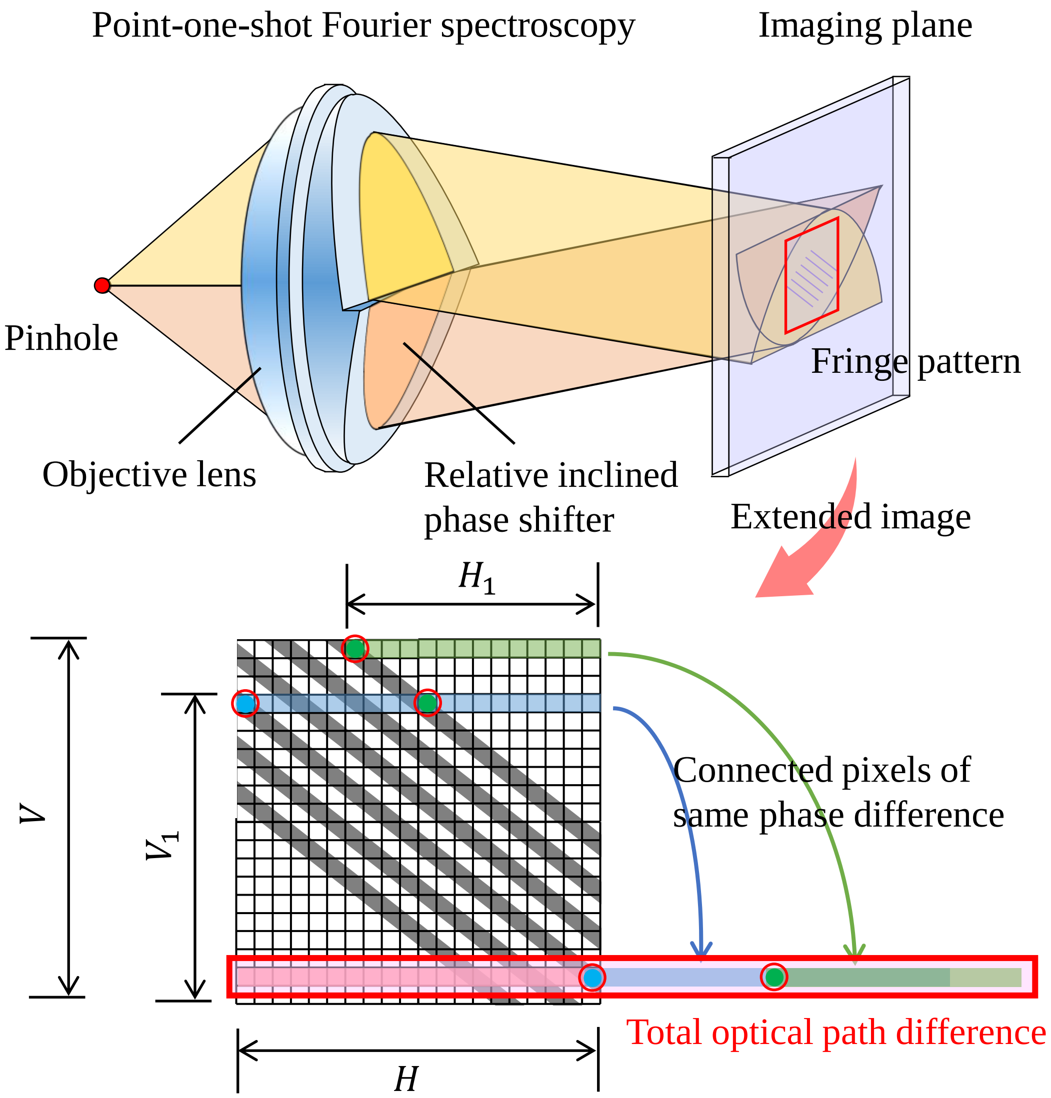

Figure 40 Schematic diagram of point-one-shot Fourier spectroscopy

4.3 Design guidelines

Point-one-shot Fourier spectroscopy is designed separately using horizontal and vertical angles of the phase-shift prism as shown in Fig. 41. The objective lens needs to be aspherical to prevent aberration.

First, the horizontal angle of the prism is calculated using Eq. (29). According to the horizontal angle θ_H of the wedge prism, the objective beam is inclined at the angle θ_i. The horizontal pixel pitch is denoted P_H. The refraction indices of the prism and air are denoted n_1 and n_2.

$$\Delta L_H = P_H \sin\theta_i$$

$$\theta_i = \sin^{-1}\frac{\Delta L_H}{P_H}$$

$$\theta_H = \tan^{-1}\frac{n_2 \sin\theta_i}{n_1 - n_2 \cos\theta_i} \tag{29}$$

Second, the vertical angle of the prism should be calculated separately using the OPDs per pixel of upper and lower sides. Because the vertical angle θ_H of the wedge prism is given to two planes to intersect objective beams of upper and lower sides each other on the imaging plane, the objective beams are inclined at angles θ_j and θ_k. The vertical OPD per pixel of the upper side's objective beam is ΔL_j and that of the lower side's objective beam is ΔL_k as expressed in Eq. (30). The vertical pixel pitch is denoted P_V.

$$\Delta L_j = P_V \sin\theta_j\,, \quad \Delta L_k = P_V \sin\theta_k \tag{30}$$

If the vertical angles on upper and lower sides of the wedge prism are the same, the total vertical OPD per pixel ΔL_V is calculated using

Eq. (31).

$$\Delta \mathrm{L}_V = \Delta \mathrm{L}_j + \Delta \mathrm{L}_k = P_V(\sin\theta_j + \sin\theta_k)$$

$$\Delta \mathrm{L}_V = 2P_V \sin\theta_j \quad (\theta_j = \theta_k) \tag{31}$$

We then calculate the vertical angle θ_j of the objective beam using Eq. (32).

$$\theta_j = \sin^{-1}\frac{\Delta \mathrm{L}_V}{2P_V} \tag{32}$$

Finally, using Eq. (33), the vertical angle of the wedge prism θ_V is calculated.

$$\theta_V = \tan^{-1}\frac{n_1 - n_2\cos\theta_j}{n_2\sin\theta_j} \tag{33}$$

Additionally, the length l from the wedge prism to the imaging plane is given by Eq. (34). The radius of the lens is denoted r.

$$l = \frac{r}{2\tan\theta_j} \tag{34}$$

The angle θ_f of the fringe pattern at the imaging plane is calculated using Eq. (35).

$$\theta_f = \frac{\Delta L_V}{\Delta L_H} \tag{35}$$

I made two prototypes of a point-one-shot Fourier spectroscopic imager as shown in Fig. 42 [97-107]. The prototype (germanium lens) (Pax Co.) in Fig. 42(a) has a wedge prism with a horizontal angle of 1.2 degrees and a vertical angle of 1.5 degrees, a wavelength resolution of 0.22 μm, and an OPD of 464 μm when a VIM-80G2 camera (Vision Sensing Co. Ltd.) is used. The prototype (Nalux Co., Ltd.) in Fig. 42(b) has a wedge prism with a horizontal angle of 2.2 degrees and vertical angle of 2.1 degrees, a wavelength resolution of 0.06 μm, and an OPD of 1613 μm when an A35 camera (FLIR Systems, Inc.) is used. We evaluated and confirmed the high interference intensity on the model in Fig. 42(a), which was analyzed using CODE V optical design software, as shown in Figure 43.

The field stop of point-one-shot Fourier spectroscopy is designed using Eq. (11). We separately calculate the horizontal and vertical widths of the aperture area using the OPD per pixel for each axis. As an example, the horizontal width of the aperture is 14 μm and the vertical width is 7 μm for the model in Fig. 42(b). If the width is too narrow and the diffraction angle is too great, the width can be widened by odd number times.

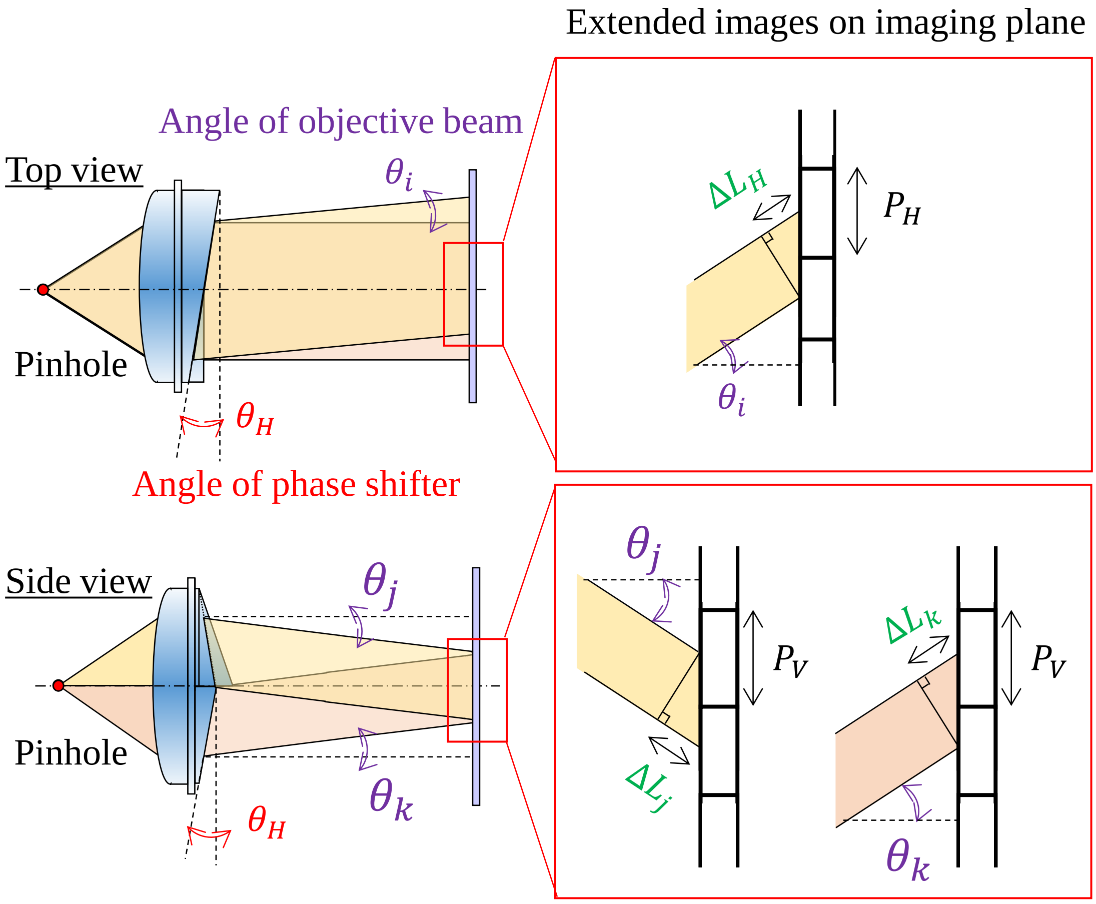

Figure 41 Top view and side view of point-one-shot Fourier spectroscopy

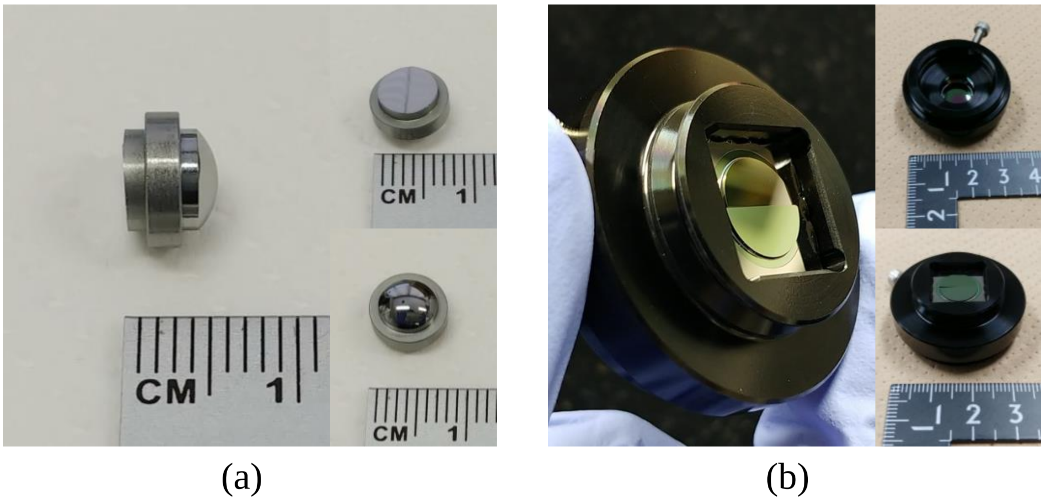

Figure 42 Prototypes of the point-one-shot Fourier spectrometer

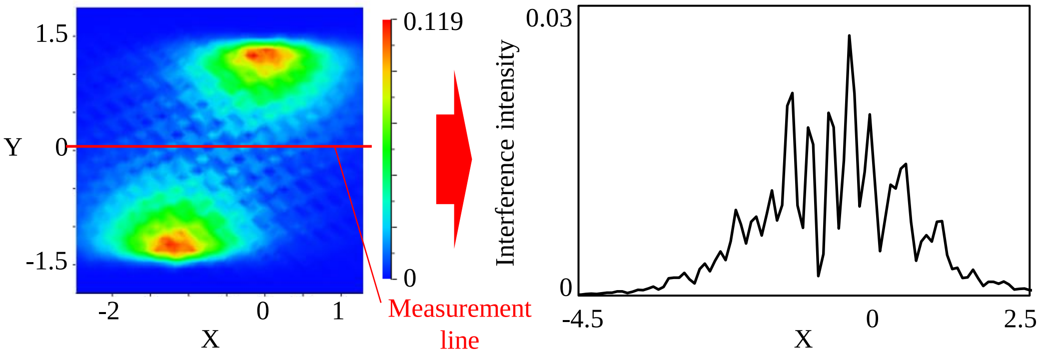

Figure 43 Result of optical design simulation using CODE V

4.4 Verification experiment

We performed verification experiments using a prototype (Fig. 39(b)) of the point-one-shot Fourier spectrometer. We used a camera (model: A35, manufacturer: FLIR Systems, Inc.), a 20-µm-diameter pinhole, and $\mathrm{CO_2}$ laser (model: L3SL, manufacturer: Access Laser). As shown in Fig. 44, we confirmed a fringe pattern inclined about 27.8 deg. on the imaging plane. This prototype has $\Delta L_H = 2$ µm and $\Delta L_V = 3.8$ µm. The number of pixels which is optical path difference was 320 pixels and the wavelength resolution was 0.15 µm. Then, we obtained the spectral peak of the $\mathrm{CO_2}$ laser at 10.5 µm as shown in Fig. 45. Additionally, after the same phase pixels were connected (the number of pixels was 430 pixels and the wavelength resolution was 0.12 µm) for improving the optical path difference, we could confirm the improvement of half-bandwidth in spectroscopic characteristics of CO2 laser as shown in Fig. 46. We therefore verified the principle of point-one-shot Fourier spectroscopy experimentally. However, because there is much stray light and a non-uniform distribution of the light intensity on the imaging plane, we need to improve the optical system and introduce a white-light source to confirm the theoretical improvement in the wavelength resolution experimentally in future work.

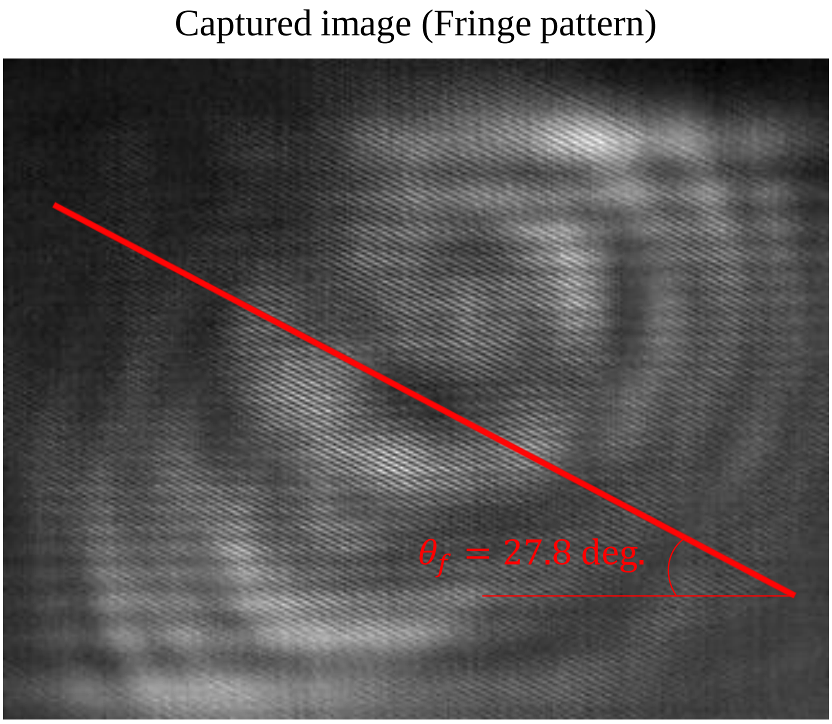

Figure 44 Image of a fringe pattern on the imaging plane

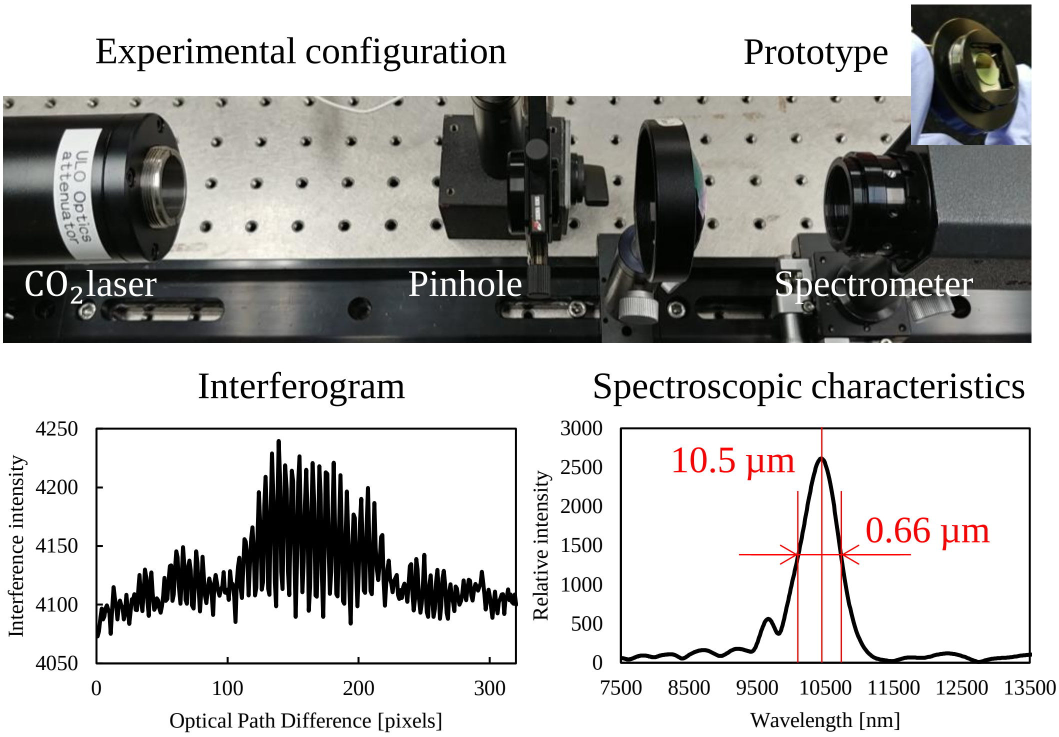

Figure 45 Experimental configuration and the result of the verification experiment

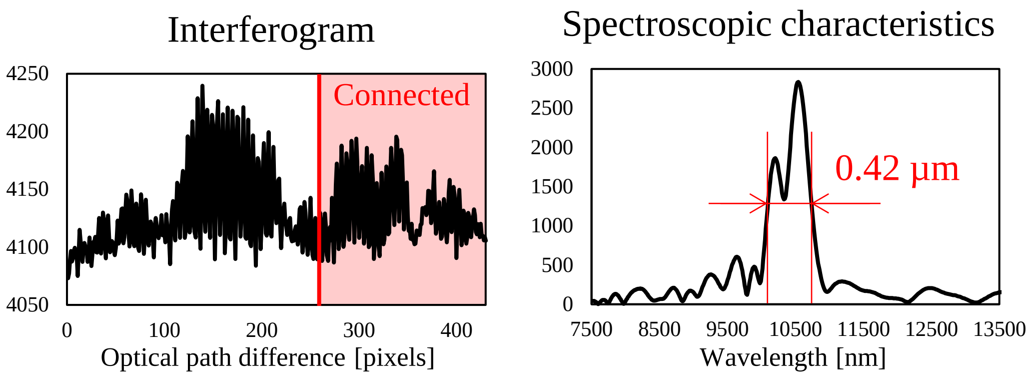

Figure 46 Experimental configuration and the result of the verification experiment after the pixels which have same phases are connected

4.5 Summary

I proposed point-one-shot Fourier spectroscopy for the improvement of wavelength resolution and realizing low-cost and bean-sized spectrometers that can be mounted on wearable terminals. We demonstrated the principle of our method in a verification experiment using a 20-µm-diameter pinhole and CO_2 laser. In future work, the spectrometer will be applied to a white-light source and the optical system improved for experimental confirmation of the theoretical wavelength resolution.

Thesis Summary

In recent years, IoT (Internet of Things) technology that enables automatic recognition, automatic control, and remote measurement by transmitting information, obtained from sensors, via the Internet has received attention globally. However, no spectroscopic imaging apparatus in the infrared region, particularly in the long-wavelength infrared region suitable for component analysis, has been installed or put into practical use. Thus, by establishing a small long-wavelength infrared spectrometer as a component sensor that can be mounted on wearable terminals, it is possible for casual daily-life data to contribute to social issues, such as achieving Sustainable Development Goals. I therefore proposed and demonstrated the feasibility of realizing ultra-miniature long-wavelength infrared Fourier spectroscopy with high wavelength resolution and high sensitivity for on-site component measurement.

First, I proposed the wide-field-stop and Beam-expansion method for improving the detected light intensity of spatial-phase-shift interferometers. The one-shot Fourier spectrometer is a spatial-phase-shift interferometer having low sensitivity, such that that only the spectral characteristics of light sources in the long-wavelength infrared region with direct illumination are obtained, because a single slit is used as a field stop. The use of a wider field stop slit increases the detected light intensity but narrows the diffraction angle. A narrower collimated objective beam diameter degrades the visibility of interferograms. Therefore, a plano-concave cylindrical lens was introduced between the objective plane and the single slit to expand the beam diameter. The sensitivity improvement achieved when using the wide-field-stop and beam-expansion method allows the spectral characteristics of hemoglobin to be obtained non-invasively from a human palm using a midget lamp.

Second, the proposed superimposing interferogram method uses a multi-slit array as a redesigned field stop for the spatial-phase-shift interferometer. The widths of the apertural and blocked areas correspond to half the wavelength of the fringe pattern on the imaging plane and determine the wavelength that improves the interference definition while eliminating those wavelengths that worsen it, thus improving the interference definition of the interferogram. Additionally, to improve the interferometer's sensitivity, several apertural areas were aligned to increase the amount of incident light. We performed spectroscopic measurements and confirmed improvements in both the sensitivity and interference definition using a prototype of a bean-sized long-wavelength infrared spectroscopic imager based on a one-shot Fourier spectroscope and a prototype multi-slit array.

Finally, I proposed point-one-shot Fourier spectroscopy, which uses only one lens and a camera and one spatial-phase-shift interferometer. The proposed method detects 2D fringe patterns using point-area information, and the spectroscopy achieves high wavelength resolution through the use of a low-cost low-pixel camera. We demonstrated the principle of our method in a verification experiment using a pinhole and CO_2 laser.

We intend to make three improvements to my proposed method in future work. First, a white-light source will be applied in point-one-shot Fourier spectroscopy in the long-wavelength infrared light region and the optical system improved in terms of obtaining a uniform light intensity on the image. Second, the feasibility of quantitatively measuring a component with a large-bandwidth multi-slit array and wavelength-splitting multi-slit array will be demonstrated and the arrays will be remade for fitting with point-one-shot Fourier spectroscopy. Third, point-one-shot Fourier spectroscopy, the wide-field-stop and beam-expansion method, and the superimposing interferogram method will be combined and verification experiments performed for on-site component measurement.

Publication List

Journal Papers (First author 2 papers)

1. Natsumi KAWASHIMA, Tomoya KITAZAKI, Kosuke NOGO, Akira NISHIYAMA, Kenji WADA, and Ichiro ISHIMARU, "Superimposing interferogram method using a multi-slit array to enhance sensitivity and interference definition of spatial-phase-shift interferometers", Optical Review, volume 27, issue 6, pages 530-541, October 2020
2. Kosuke NOGO, Kou IKEJIMA, Wei QI, Natsumi KAWASHIMA, Tomoya KITAZAKI, Satoru ADACHI, Kenji WADA, Akira NISHIYAMA, and Ichiro ISHIMARU, "Identification of black microplastics using long-wavelength infrared hyperspectral imaging with imaging-type two-dimensional Fourier spectroscopy", Analytical Methods, doi: 10.1039/D0AY01738H, January 2021
3. Tomoya KITAZAKI, Natsumi KAWASHIMA, Naoyuki YAMAMOTO, Hiroyuki NOMURA, Hanyue KANG, Akira NISHIYAMA, Kenji WADA, and Ichiro ISHIMARU, "Parametric standing wave generation of a shallow reflection plane in a nonrigid sample for use in a noninvasive blood glucose monitor", J. of Biomedical Optics, 24(3), 036003 (2019)
4. Shigeru Sugawara, Yoshihiko Nakayama, Yoshihiko Nakayama, Hideya Taniguchi, Natsumi KAWASHIMA, and Ichiro ISHIMARU, "Identification accuracy improvement of non-uniform paper samples", Infrared Physics & Technology, Volume 97, Pages 217-223, March 2019
5. Naoyuki YAMAMOTO, Natsumi KAWASHIMA, Tomoya KITAZAKI, Keita MORI, Hanyue KANG, Akira NISHIYAMA, Kenji WADA, and Ichiro ISHIMARU, "Ultrasonic standing wave preparation of a liquid cell for glucose measurements in urine by midinfrared spectroscopy and potential application to smart toilets", J. Biomed. Opt., 23(5), 050503 (2018)
6. Natsumi KAWASHIMA, Kosuke NOGO, Satsuki HOSONO, Akira NISHIYAMA, Kenji WADA, Ichiro ISHIMARU, "Sensitivity improvement of one-shot Fourier spectroscopic imager for realization of noninvasive blood glucose sensors in smartphones", Opt. Eng., 55(11) 110506, November 2016

7. Kosuke NOGO, Wei QI, Keita MORI, Satoshi OGAWA, Daichi Inohara, Satsuki HOSONO, Natsumi KAWASHIMA, Akira NISHIYAMA, Kenji WADA, and Ichiro ISHIMARU, “Ultrasonic Separation of a Suspension for In-situ Spectroscopic Imaging”, Optical Review, Volume 23, Issue 2, pp 360–363, April 2016
8. Shun SATO, Wei QI, Natsumi KAWASHIMA, Kosuke NOGO, Satsuki HOSONO, Akira NISHIYAMA, Kenji WADA, and Ichiro ISHIMARU, “Ultra-miniature one-shot Fourier-spectroscopic tomography”, Opt. Eng., 55(2), 025106, February 2016
9. Wei QI, Yo SUZUKI, Shun SATO, Masaru FUJIWARA, Natsumi KAWASHIMA, Satoru SUZUKI, Pradeep Abeygunawardhana, Kenji WADA, Akira NISHIYAMA, and Ichiro ISHIMARU, “Enhanced interference-pattern visibility using multislit optical superposition method for imaging-type two-dimensional Fourier spectroscopy”, Applied Optics, Vol. 54, Issue 20, pp. 6254-6259, July 2015
10. Yo SUZUKI, Wei QI, Shun SATO, Masaru FUJIWARA, Hiroyuki HIRAMATSU, Natsumi KAWASHIMA, Satoru SUZUKI, Pradeep Abeygunawardhana, Kenji WADA, Akira NISHIYAMA, Hiroaki Kobayashi, and Ichiro ISHIMARU, “Palm-size ultra-compact wide-field Fourier spectroscopic imaging technology”, The Review of Laser Engineering, 43, (4) 222–226, April 2015
11. Shigeru Sugawara, Masaru FUJIWARA, Yo SUZUKI, Natsumi KAWASHIMA, Yoshihiko Nakayama, Hideya Taniguchi, and Ichiro ISHIMARU, “The development of a wide-field infrared spectroscopic imaging apparatus using a bolometer camera and feasibiality test for forensic examination.”, Infrared Physics & Technology, 71 389-395, July 2015

International Conference Papers (First author 7 papers)

1. Ichiro ISHIMARU, Natsumi KAWASHIMA, "Beans-size mid-infrared (LWIR: Longwave Infrared) hyperspectral camera", Proc. of International symposium on imaging, sensing, and optical memory 2020 (ISOM'20), pp.77-78, Nov. 29 - Dec. 2, 2020
2. Natsumi KAWASHIMA, Satoru ADACHI, Tomoya KITAZAKI, Hanyue KANG, Akira NISHIYAMA, Kenji WADA, and Ichiro ISHIMARU, "Ultra-miniature (diameter: 6mm, thickness: 5mm) low-cost (price:1,000 EUR) point-one-shot mid-infrared Fourier spectroscopic imager for ear clip type non-invasive blood glucose sensors", European Conferences on Biomedical Optics, Clinical and Preclinical Optical Diagnostics II, 110730H, July 2019
3. Hanyue KANG, Natsumi KAWASHIMA, Sora MIZUTANI, Tomoya KITAZAKI, Satoru ADACHI, Junya IWAKI, Kotone YOKOYAMA, Ichiro ISHIMARU, "Palm-sized and tough two-dimensional spectroscopic imager: the so-called hyperspectral camera for visible and mid-infrared light. Proposal of plant-species identification regardless of zenith and azimuth angles based on only two types of basic spectroscopic data (near-surface and internal reflectance)", SPIE Optical Metrology 2019, Multimodal Sensing: Technologies and Applications, 110590K, Munich, Germany, Proc. SPIE 11059, July 2019
4. Ichiro ISHIMARU, Hanyue KANG, Natsumi KAWASHIMA, Tomoya KITAZAKI, Junya IWAKI, Satoru ADACHI, Sora MIZUTANI, and Kotone YOKOYAMA, "Palm-sized and tough two-dimensional spectroscopic imager: the so-called hyperspectral camera for visible and mid-infrared light (first report): trial applications of the proposed two-dimensional Fourier spectroscopic imager", Optics for Arts, Architecture, and Archaeology VII, Proc. SPIE 11058, July 2019
5. Junya IWAKI, Natsumi KAWASHIMA, Naoyuki YAMAMOTO, Tomoya KITAZAKI, Hanyue KANG, Satoru ADACHI, and Ichiro ISHIMARU, "Machine learning for rapid adaptation to individual optical differences for noninvasive blood glucose sensor using mid-infrared spectroscopy", OPTICS & PHOTONICS International Congress 2019, Proc. Of SPIE Vol. 11142 1114201-59 OPTM-5-03, 2019/4/24, Yokohama, Japan
6. Kotone YOKOYAMA, Natsumi KAWASHIMA, Tomoya KITAZAKI, Sora MIZUTANI, Hanyue KANG, and Ichiro ISHIMARU, "Light-source color correlation of wide-field spectroscopic imaging for the adaption to spatial and

temporal variations when using an unmanned aerial vehicle", OPTICS & PHOTONICS International Congress 2019, Proc. Of SPIE Vol. 11142 1114201-50 OPTM-4-03, 2019/4/24, Yokohama, Japan

7. Natsumi KAWASHIMA, Ichiro ISHIMARU, Tomoya KITAZAKI, Kosuke NOGO, Hanyue KANG, Akira NISHIYAMA, and Kenji WADA, "Ultrasonic-assisted point-one-shot mid-infrared Fourier spectroscopy for realization of ear-clip type non-invasive blood glucose sensors: ultra-miniature point-one-shot mid-infrared spectroscopic imager (diameter: 10 mm, thickness: 25 mm) configured of only 1 lens (1st report)", SPIE Photonics West BiOS 2019, 10885-32, 2019/02/05, USA
8. Natsumi KAWASHIMA, Ichiro ISHIMARU, Tomoya KITAZAKI, Kosuke NOGO, Hanyue KANG, Akira NISHIYAMA, and Kenji WADA, "Ultrasonic-assisted point-one-shot mid-infrared Fourier spectroscopy for realization of ear-clip type non-invasive blood glucose sensors: ultrasonic-assisted method for production of a reflection plane near the skin surface and detection of the blood glucose absorption peak in mice (2nd report)", SPIE Photonics West BiOS 2019, 10885-33, 2019/02/05, USA
9. Natsumi KAWASHIMA, Tomoya KITAZAKI, Hiroyuki NOMURA, Akira NISHIYAMA, Kenji WADA, and Ichiro ISHIMARU, "Detection of Blood Glucose Level in Mice using Ultrasonic-assisted Mid-infrared Fourier Spectroscopy for realizing Earring-type Non-invasive Blood Glucose Sensors", OSA Imaging and Applied Optics 2018, JM4A.2, 2018/06/25-28, USA
10. Hiroyuki NOMURA, Keita MORI, Natsumi KAWASHIMA, Tomoya KITAZAKI, Akira NISHIYAMA, Kenji WADA, and Ichiro ISHIMARU, "Ultrasonic-Assisted Blood Glucose Monitoring using Mid-Infrared Spectroscopy", OSA Imaging and Applied Optics 2018, JM4A.9, 2018/06/25-28, USA
11. Tomoya KITAZAKI, Natsumi KAWASHIMA, Naoyuki YAMAMOTO, Hiroyuki NOMURA, Akira NISHIYAMA, Kenji WADA, and Ichiro ISHIMARU, "Measurement of glucose concentrations inside agar using parametric standing wave to realize non-invasive blood glucose sensor", OSA Imaging and Applied Optics 2018, JTu4A.18, 2018/06/25-28, USA
12. Hanyue KANG, Natsumi KAWASHIMA, Tomoya KITAZAKI, Sora MIZUTANI, and Ichiro ISHIMARU, "Plant-species identification from only near-surface and internal reflectance spectroscopic data regardless of zenith and azimuth angle", Light, Energy and the Environment Congress 2018, HM2C.4, 2018/11/05-08, Singapore
13. Ichiro ISHIMARU, Natsumi KAWASHIMA, Hanyue KANG, Tomoya KITAZAKI, Kosuke NOGO, and Wei QI, "Extremely compact hyperspectral cameras of visible

and infrared lights for environmental measurements”, Hyperspectral Imaging and Sounding of the Environment 2018, Light, Energy and the Environment 2018 (E2, FTS, HISE, SOLAR, SSL) OSA Technical Digest (Optical Society of America, 2018), paper HM3C.1, 5–8 November 2018, Singapore

14. Tomoya KITAZAKI, Keita MORI, Naoyuki YAMAMOTO, Congtao WANG, Natsumi KAWASHIMA, and Ichiro ISHIMARU, “Proposal of ultrasonic-assisted mid-infrared spectroscopy for incorporating into daily life like smart-toilet and non-invasive blood glucose sensor”, European Conferences on Biomedical Optics 2017, Vol. 10412 pp. 1041204-1041204-4, 2017/6/28, Germany
15. Sora MIZUTANI, Shuu INOUE, Tsubasa Saito, Natsumi KAWASHIMA, and Ichiro ISHIMARU, “PALM-SIZE HYPERSPECTRAL CAMERA (TOTAL WEIGHT: 1.7[KG], WAVELENGTH: VIS, NIR AND LWIR) FOR UAV AND NANOSATELLITE”, International Symposium on Remote Sensing 2017, P-66, 2017.04., Japan
16. Natsumi KAWASHIMA, Satsuki HOSONO, and Ichiro ISHIMARU, “Built-in hyperspectral camera for smartphone in visible, near-infrared and middle-infrared lights region: Sensitivity improvement of Fourier spectroscopic imaging to detect diffuse reflection lights from internal human tissues for healthcare sensors”, SPIE Commercial + Scientific Sensing and Imaging, 985505, 18 April 2016 • 9:10 - 9:30 AM, USA
17. Satsuki HOSONO, Natsumi KAWASHIMA, and Ichiro ISHIMARU, “Built-in hyperspectral camera for smartphone in visible, near-infrared and middle-infrared lights region: Spectroscopic imaging for broad-area and real-time componential analysis system against local unexpected terrorism and disasters”, SPIE Commercial + Scientific Sensing and Imaging, 985506, 18 April 2016 • 9:30 - 9:50 AM, USA
18. Ichiro ISHIMARU, Natsumi KAWASHIMA, and Satsuki HOSONO, “Built-in hyperspectral camera for smartphone in visible, near-infrared and middle-infrared lights region: Trial products of beans-size Fourier-spectroscopic line-imager and feasibility experimental results of middle infrared spectroscopic imaging”, SPIE Commercial + Scientific Sensing and Imaging, 985504, 18 April 2016 • 8:50 - 9:10 AM, USA
19. Kosuke NOGO, Keita MORI, Wei QI, Satsuki HOSONO, Natsumi KAWASHIMA, Akira NISHIYAMA, Kenji WADA, and Ichiro ISHIMARU, “Thumb-size ultrasonic-assisted spectroscopic imager for in-situ glucose monitoring as optional sensor of conventional dialyzers”, SPIE BiOS, 96990N, 13 February 2016 • 4:20 - 4:40 PM, USA

20. Satsuki HOSONO, Kengo AIZAWA, Tsubasa SAITO, Mizuho OKADA, Kosuke NOGO, Natsumi KAWASHIMA, and Ichiro ISHIMARU, "Quantitative Evaluation of the Object Color without Influence from the Light Source Color under Unstructured Environment -A Background Correction Method Using Polarization Properties-", Optical Society of America, 2016 in Hyperspectral Imaging and Sounding of the Environment, paper JW4A.22, 2016/11/14-17, Germany
21. Natsumi KAWASHIMA, Shun SATO, Akane ISHIDA, Daichi INOHARA, Naotaka TANAKA, Kenji WADA, Akira NISHIYAMA, Masaru FUJIWARA, and Ichiro ISHIMARU, "Proposal of snapshot line-imaging Fourier spectroscopy for smartphone", Proc. SPIE Optics and Biophotonics in Low-Resource Settings, Proc. SPIE 9314, 93140P, 2015/3/12, USA
22. Natsumi KAWASHIMA, Yo SUZUKI, Wei QI, Satsuki HOSONO, Tsubasa SAITO, Satoshi OGAWA, Shun SATO, Masaru FUJIWARA, Akira NISHIYAMA, Kenji WADA, Naotaka TANAKA, and Ichiro ISHIMARU, "Palm-size wide-field Fourier spectroscopic imager with uncooled infrared microbolometer arrays for smartphone", Proc. SPIE 9314, Optics and Biophotonics in Low-Resource Settings, 93140Q, 2015/3/12, USA

Domestic Conference Papers (First author 13 papers)

1. 川嶋なつみ、北崎友哉、足立智、野郷孝介、西山成、和田健司、石丸伊知郎、“インターフェログラム重畳法を用いた広帯域多重スリットによる高感度中赤外フーリエ分光器”、Optics & Photonics Japan 2020、16pD4、2020/11/14-17
2. 足立智、岩城順也、斉威、川嶋なつみ、北崎友哉、和田健司、石丸伊知郎、“結像型 2 次元フーリエ分光装置による屋外環境におけるガス種の弁別イメージング”、Optics & Photonics Japan 2020、16aC1、2020/11/14-18
3. 川嶋なつみ、北崎友哉、野郷孝介、石丸伊知郎、“インターフェログラム重畳法によるマルチスリット搭載型高感度中赤外ワンショットフーリエ分光器”、2020 年度精密工学会秋季大会学術講演会、D0112、2020/09/01-07
4. 足立智、岩城順也、水谷空、川嶋なつみ、北崎友哉、康瀚月、石丸伊知郎、“手のひらサイズユニットの温度制御による中赤外パッシブ分光イメージング”、2020 年度精密工学会春季大会学術講演会、K11、2020/3/17
5. 北崎友哉、川嶋なつみ、石丸伊知郎、“ワンショット中赤外分光イメージング高感度化のインターフェログラム重畳法”、2020 年度精密工学会春季大会学術講演会、K09、2020/3/17
6. 岩城順也、川嶋なつみ、北崎友哉、足立智、横山琴音、石丸伊知郎、“文化財染料同定を目指した手の平サイズ熱放射分光イメージング”、Optics & Photonics Japan 2019、2aD2、2019/12/2
7. 川嶋なつみ、北崎友哉、西山成、和田健司、石丸伊知郎、“マルチスリット搭載型高感度中赤外ワンショットフーリエ分光器”、Optics & Photonics Japan 2019、PDP3、2019/12/5
8. 川嶋なつみ、北崎友哉、西山成、和田健司、石丸伊知郎、“イヤリング型非侵襲血糖値センサーを目指した皮膚表層近傍における微弱な反射光検出が可能な高感度中赤外分光法”、第 4 回黒潮カンファレンス、P37、2019/11/15
9. 川嶋なつみ、北崎友哉、西山成、和田健司、石丸伊知郎、“イヤリング型非侵襲血糖値センサーを目指した超音波アシスト中赤外フーリエ分光法”、2019 年度精密工学会秋季大会学術講演会、L46、2019/9/5
10. 足立智、山本直幸、川嶋なつみ、北崎友哉、康瀚月、西山成、石丸伊知郎、“スマートトイレを目指した超音波アシスト中赤外分光イメージング”、2019 年度精密工学会春季大会学術講演会、C78、2019/3/15, 東京
11. 岩城順也、逢澤健吾、尾畑克哉、岡野滉平、川嶋なつみ、北崎友哉、康瀚月、石丸伊知郎、“文化財の On-site 色材計測を目指した手のひらサイズ高感度中

赤外分光イメージング装置の開発”、2019 年度精密工学会春季大会学術講演会、C73、2019/3/15, 東京

12. 横山琴音、康瀚月、川嶋なつみ、北崎友哉、水谷空、石丸伊知郎、“観察角度に依存しない植物同定を目指した遠隔分光計測における反射補正式の検証”、2019 年度精密工学会春季大会学術講演会、C77、2019/3/15, 東京
13. 乃村宏幸、野郷孝介、川嶋なつみ、北崎友哉、康瀚月、西山成、石丸伊知郎、“豆粒大中赤外分光ユニットによる透析装置の in-situ 血糖値モニタリング”、2018 年度精密工学会秋季大会学術講演会、D01-4, 1A(T)54、2018/9/5, 北海道
14. 康瀚月、川嶋なつみ、北崎友哉、水谷空、石丸伊知郎、“植物のクロロフィル分光計測による光合成活性度評価”、2018 年度精密工学会秋季大会学術講演会、D01-3, 1A(T)53、2018/9/5, 北海道
15. 井原豪太、山本直幸、川嶋なつみ、北崎友哉、康瀚月、石丸伊知郎、“On-site 中赤外分光成分計測を目指した超音波液体セルの高安定性形状”、2018 年度精密工学会秋季大会学術講演会、D01-2, 1A(T)52、2018/9/5, 北海道
16. 川嶋なつみ、王从涛、西山成、和田健司、石丸伊知郎、“イヤリング型非侵襲血糖値センサーを目指した超音波アシスト中赤外ポイントワンショット分光法の提案”、第 3 回黒潮カンファレンス、P-02、2018/10/13-14, 島根
17. 川嶋なつみ、王从涛、北崎友哉、康瀚月、野郷孝介、石丸伊知郎、“イヤリング型非侵襲血糖値センサーを目指した超音波アシスト中赤外ポイント分光システムの提案～感度及び SN 比の改善を目的とした高開口数ポイントワンショット中赤外分光法～”、Optics & Photonics Japan 2018、31aB3、2018/10/31, 東京
18. 天谷貴、川嶋なつみ、北崎友哉、康瀚月、野郷孝介、石丸伊知郎、“イヤリング型非侵襲血糖値センサーを目指した超音波アシスト中赤外ポイント分光システムの提案～少数の教師データにより個人差に適応する高効率機械学習法～”、Optics & Photonics Japan 2018、31aB2、2018/10/31, 東京
19. 北崎友哉、川嶋なつみ、乃村宏幸、康瀚月、西山成、和田健司、石丸伊知郎、“超音波アシスト中赤外分光イメージングを用いた生体内外における血糖値モニタリング―サンプル表層近傍からのパラメトリック定在波を用いた内部反射光検出―”、電気学会バイオメディカル研究会、講演番号 2-2、2018/3/5, 東京
20. 乃村宏幸、川嶋なつみ、北崎友哉、西山成、和田健司、石丸伊知郎、“超音波アシスト中赤外分光イメージングを用いた生体内外における血糖値モニタリング―透析装置への搭載を目指した超音波液体セルユニットの提案―”、電気学会バイオメディカル研究会、講演番号 2-1、2018/3/5, 東京
21. 川嶋なつみ、北崎友哉、乃村宏幸、西山成、和田健司、石丸伊知郎、“超音波

アシスト中赤外分光イメージングを用いた生体内外における血糖値モニタリング—非侵襲血糖値センサーの計測領域選定を目的としたマウス耳内部のグルコース検出—”、電気学会バイオメディカル研究会、講演番号 2-3、2018/3/5, 東京

22. 岡野滉平、井上志優、水谷空、森敬太、川嶋なつみ、多田邦尚、石丸伊知郎、“ドローンを用いた 1 万平米の海域における分光画像構築による葉緑素定量計測”、2018 年度精密工学会春季大会学術講演会、F69、2018/03/15-20, 東京
23. 乃村宏幸、森敬太、川嶋なつみ、北崎友哉、西山成、和田健司、石丸伊知郎、“超音波アシスト中赤外分光法による透析時の血糖値モニタリングを目的とした液体セルの提案”、2018 年度精密工学会春季大会学術講演会、O32、2018/03/15-19, 東京
24. 康瀚月、北崎友哉、川嶋なつみ、西山成、和田健司、石丸伊知郎、“非侵襲血糖値センサーを目指したパラメトリック定在波による生体膜内部における反射面生成手法”、2018 年度精密工学会春季大会学術講演会、O33、2018/03/15-18, 東京
25. 尾畑克哉、井原豪太、森敬太、山本直幸、川嶋なつみ、王从涛、北崎友哉、西山成、和田健司、石丸伊知郎、“中赤外分光法によるスマートトイレの実現を目指した超音波液体セルの提案”、2018 年度精密工学会春季大会学術講演会、O39、2018/03/15-17, 東京
26. 川嶋なつみ、北崎友哉、西山成、和田健司、石丸伊知郎、“非侵襲血糖値センサーを目指し超音波アシスト中赤外分光イメージング”、レーザー学会 中国・四国支部、関西支部連合 若手学術交流研究会、E-2、2017/12/02, 香川
27. 川嶋なつみ、北崎友哉、西山成、和田健司、石丸伊知郎、“非侵襲血糖値センサーを目指した超音波アシストフーリエ分光法によるマウスのグルコース成分計測”、第 2 回黒潮カンファレンス、P-34、2017/10/28, 高知
28. 水谷空、天谷貴、逢澤健吾、川嶋なつみ、石丸伊知郎、“光源色に依存しない立体形状物に対する広視野での色彩計測”、日本色彩学会誌、JCSAJ Vol.41 No.3 p. 5-6、2017.06 東京
29. 北崎友哉、川嶋なつみ、山本直幸、井原豪太、西山成、和田健司、石丸伊知郎、“非侵襲血糖値センサー実現を目指した超音波アシスト中赤外光分光イメージング—パラメトリック定在波による皮膚表層近傍からの中赤外反射光の検出—”、Optics & Photonics Japan 2017、31aB3、2017/10/16, 東京
30. 川嶋なつみ、北崎友哉、森敬太、山本直幸、西山成、和田健司、石丸伊知郎、“皮膚表層近傍の分光吸収係数トモグラフィ計測を目指した中赤外帯域におけるマウスの血中グルコース検出”、Optics & Photonics Japan 2017、PDP1、

2017/10/16, 東京

31. 王从涛、山本直幸、川嶋なつみ、吉田光宏、谷口秀哉、林宏樹、楠原果奈、斉威、石丸伊知郎、“スマートフォン内蔵を目指した中赤外ワンショット分光イメージング実現への挑戦―感度改善を目的とした反射光学系による実証実験―”、Optics & Photonics Japan 2017、2aA9、2017/10/16, 東京
32. 井上志優、水谷空、森敬太、川嶋なつみ、多田邦尚、石丸伊知郎、“海中栄養塩量の異常を早期発見する広域分光イメージング―屋外環境の変化を考慮した光源色補正による植物プランクトンの計測―”、Optics & Photonics Japan 2017、1aB8、2017/10/16, 東京
33. 井原豪太、森敬太、山本直幸、川嶋なつみ、王从涛、北崎友哉、西山成、和田健司、石丸伊知郎、“日常生活空間での尿糖・尿蛋白モニタリングを目指した超音波アシスト分光イメージング―超音波液体セルの高安定性形状―”、Optics & Photonics Japan 2017、31aB2、2017/10/16, 東京
34. 山本直幸、西藤翼、小川哲、岡田瑞穂、川嶋なつみ、多田邦尚、石丸伊知郎、“ドローンへ搭載可能な超小型ハイパースペクトルカメラの試作および災害対策実証実験”、2016年度精密工学会秋季大会学術講演会、B64、2016/09/06-08, 茨城
35. 山本直幸、藤原大、猪原大地、野郷孝介、吉田光宏、森敬太、川嶋なつみ、西山成、石丸伊知郎、“高感度分光イメージングによる液体セルや生体試料内部における全血の計測”、2016 年度精密工学会春季大会学術講演会、T75、2016/03/15-17, 東京
36. 岡田瑞穂、西藤翼、川嶋なつみ、森敬太、多田邦尚、石丸伊知郎、“屋外環境下での広域分光イメージングによる光源色補正法―瀬戸内海におけるクロロフィルの定量計測―”、Optics & Photonics Japan 2016、2pC6、2016/10/15, 東京
37. 山本直幸、野郷孝介、森敬太、片山喬志、細野皐月、川嶋なつみ、西山成、和田健司、石丸伊知郎、“日常生活空間におけるグルコースセンサーの提案―尿糖・尿蛋白の中赤外分光計測―”、Optics & Photonics Japan 2016、1aA8、2016/10/15, 東京
38. 川嶋なつみ、平松裕行、藤原大、西山成、和田健司、石丸伊知郎、“スマートフォン内蔵型ヘルスケアセンサを目指したワンショットフーリエ分光イメージング”、第 13 回医用分光学研究会、JAMS-22、2015.12.03-04.東京
39. 西藤翼、小川哲、川嶋なつみ、斉、Pradeep Abeygunawardhana、石丸伊知郎、“ドローンに搭載可能な超小型（73[mm]×102[mm]×66[mm]）軽量（540[g]）中赤外フーリエ分光イメージングユニット”、Optics & Photonics Japan 2015、30pB3、2015/10/15, 東京

40. 川嶋なつみ、平松裕行、藤原大、細野皐月、西山成、和田健司、Pradeep Abeygunawardhana、石丸伊知郎、“スマートフォン搭載ヘルスケアセンサーを目指したワンショットフーリエ分光イメージング装置の高感度化”、Optics & Photonics Japan 2015、29pA10、2015/10/15, 東京

Record of Awards

1. 第13回医用分光学研究会、若手優秀研究者賞、2015.12.04
   川嶋なつみ、平松裕行、藤原大、西山成、和田健司、石丸伊知郎、“スマートフォン内蔵型ヘルスケアセンサを目指したワンショットフーリエ分光イメージング”、第13回医用分光学研究会、JAMS-22、2015.12.03-04.東京
2. レーザー学会 中国・四国支部・関西支部連合 若手学術交流研究会、優秀発表賞、2017.12.03
   川嶋なつみ、北崎友哉、西山成、和田健司、石丸伊知郎、“非侵襲血糖値センサーを目指し超音波アシスト中赤外分光イメージング”、レーザー学会 中国・四国支部、関西支部連合 若手学術交流研究会、E-2、2017/12/02, 香川
3. 2017年度日本機械学会、三浦賞、2018.03.24
4. 第3回黒潮カンファレンス、最優秀ポスター賞、2018.10.14
   川嶋なつみ、王从涛、西山成、和田健司、石丸伊知郎、“イヤリング型非侵襲血糖値センサーを目指した超音波アシスト中赤外ポイントワンショット分光法の提案”、第3回黒潮カンファレンス、P-02、2018/10/13-14, 島根
5. 2019年精密工学会メカノフォトニクス専門委員会、吉澤奨励賞、2019.09.05
   Natsumi KAWASHIMA, Kosuke NOGO, Satsuki HOSONO, Akira NISHIYAMA, Kenji WADA, Ichiro ISHIMARU, “Sensitivity improvement of one-shot Fourier spectroscopic imager for realization of noninvasive blood glucose sensors in smartphones”, Opt. Eng., 55(11) 110506, November 2016
6. 2019年度精密工学会秋季大会学術講演会、Best Presentation賞、2019.09.05
   川嶋なつみ、北崎友哉、西山成、和田健司、石丸伊知郎、“イヤリング型非侵襲血糖値センサーを目指した超音波アシスト中赤外フーリエ分光法”、2019年度精密工学会秋季大会学術講演会、L46、2019/9/6
7. 2020年度精密工学会秋季大会学術講演会、アドバンスト・ベストプレゼンテーション賞、2020.09.14
   川嶋なつみ、北崎友哉、野郷孝介、石丸伊知郎、“インターフェログラム重畳法によるマルチスリット搭載型高感度中赤外ワンショットフーリエ分光器”、D0112、pp. 332-333

References

[1] H. Ullah, G. Gilanie, F. Hussain, E. Ahmad, “Autocorrelation optical coherence tomography for glucose quantification in blood”, Laser Physics Letters, Vol. 12 (12), 125602, (2015).

[2] K. Larin, M. Motamedi, T. Ashitkov and R. Esenaliev, “Specificity of noninvasive blood glucose sensing using optical coherence tomography technique: a pilot study”, Physics in Medicine and Biology, Vol. 48 (10), 1371, (2003).

[3] R. Esenaliev, K. Larin, I. Larina, and M. Motamedi, “Noninvasive monitoring of glucose concentration with optical coherence tomography”, Optics Letters, Vol. 26 (13), 992, (2001).

[4] Silje S. Fuglerud, Karolina Milenko, Reinold Ellingsen, Astrid Aksnes, Dag R. Hjelme, “Feasibility of supercontinuum sources for use in glucose sensing by absorption spectroscopy”, European Conferences on Biomedical Optics, Proceedings Volume 11073, Clinical and Preclinical Optical Diagnostics II; 110730E, 2019, Munich, Germany

[5] Katsuhiro Maruo and Yukio Yamada, “Near-infrared noninvasive blood glucose prediction without using multivariate analyses: introduction of imaginary spectra due to scattering change in the skin”, Journal of Biomedical Optics, 20 (4), 047003, April 2015

[6] Jyoti Yadav, et al., “Prospects and limitations of noninvasive blood glucose monitoring using near-infrared spectroscopy”, Biomedical Signal Processing and Control, 18, pp. 214-227, 2015

[7] Yasuhiro Uwadaira, et al., “Identification of informative bands in the short-wavelength NIR region for non-invasive blood glucose measurement”, Biomedical Optics Express, vol. 7, no. 7, July 2016

[8] Takero Uemura, et al., “Non-invasive blood glucose measurement by Fourier transform infrared spectroscopic analysis through the mucous membrane of the lip: application of a chalcogenide optical fiber system”, Med. Biol. Engng., vol. 9, no. 2, pp. 137-153, 1999

[9] FrinGOe: A Spectrometer-On-the-Go, white paper, ver. 2.0, https://fringoe.com/

[10]尾崎幸洋，“分光学への招待”，産業図書株式会社（1997）

[11] 尾崎幸洋, ”日本分光学会測定法シリーズ 32 近赤外分光法”, 日本分光学会、講談社 （1996）

[12] 阿久津秀雄、嶋田一夫、鈴木榮一郎、西村善文、“NMR 分光法”、講談社、2016 年

[13] 増谷浩二、“フーリエ分光の現状”、光学、第 21 巻、第 6 号、1992 年 6 月

[14] 分析機器年表、一般社団法人日本分析機器工業会

[15] 荒井康夫、安江任、“実験固体化学入門(X) 7 赤外吸収スペクトル(1)”、Gypsum & Lime No. 187、1983 年

[16] 赤尾賢一、“赤外分光法”、J. Jpn. Soc. Colour Mater., 78 (10), 480-488 (2005)

[17] 玉戀敬悦、“フーリエ変換式赤外分光光度計”、分光研究、第 27 巻、第 6 号、1978 年

[18] 諸隈肇、“光波干渉計測原論”、光学、第 12 巻、第 1 号、1983 年

[19] 左貝潤一，”光学の基礎”，株式会社コロナ社 （1997）

[20] 渋谷眞人，”回折と結像の光学”，朝倉書店 (2005)

[21] 小池裕幸，“分光測定の基礎”，低温科学 vol. 67，pp. 431-447 (2009).

[22] 谷田貝富彦，“例題で学ぶ光学入門”，森北出版株式会社 (2010)

[23] 久保田広、“光学”、岩波オンデマンドブックス、2012 年

[24] 久保田広、“波動光学”、岩波オンデマンドブックス、2014 年

[25] 永田信一，” 図解 レンズがわかる本”，日本実業出版 (2008)

[26] (社)応用物理学会日本光学会光設計研究グループ，”回折光学素子入門”，オプトロニクス社 (1997)

[27] 石黒浩三，”基礎物理学選書 23 光学”，株式会社裳華房 （1982）

[28] 伊藤敏雄，”な～るほど！の波と光”，学術図書出版 （2007）

[29] 山崎正彦之，若木守明，陳軍，”波動光学入門”，実教出版株式会社 （2006）

[30] 古川行夫、“赤外分光法”、講談社、2018 年

[31] “振動分光学”、学会出版センター

[32] 宮尾亘、“光センシング工学”、日本理工出版会

[33] 山崎昶、“赤外分光 30 講”、朝倉書店、2016 年

[34] Joseph W. Goodman, ”フーリエ光学”，森北出版株式会社 (2012)

[35] 田中誠之，寺前紀夫，”赤外分光法”，共立出版株式会社 (1993)

[36] 谷田貝富彦，”現代人の物理 5 光とフーリエ変換”，朝倉書店 （1992）

[37] Tanja M. Greve, et al., “Penetration mechanism of dimethyl sulfoxide in human and pig ear skin: An ATR-FTIR and near-FT Raman spectroscopic in vivo and in vitro study”, Spectroscopy, 22, pp. 405-417, 2008

[38] Diana L. Garcia-Rubio, “Analysis of platelets in hypertensive and normotensive individuals using Raman and Fourier transform infrared-attenuated total reflectance

spectroscopies”, Journal of Raman spectroscopy, 50, pp. 509-521, 2019

[39] Y. Inoue, I. Ishimaru, et al, “Variable phase-contrast fluorescence spectrometry for fluorescently stained cells”, Applied Physics Letters, 89, 121103 (2006)

[40] Qi Wei，原田伯城，浦木智央，河尻武士，矢野川果奈，宅間崇史，藪下真司，乾明日香，石丸伊知郎，” 可搬型フーリエ分光イメージング手法の物体光揺らぎへのロバスト性評価”, 2010 年度精密工学会春季大会学術講演会論文集，p.L45 (2010)

[41] Qi Wei，河尻武士，浦木智央，矢野川果奈，宅間崇史，鈴木孝明，西山成，高橋悟, 石丸伊知郎, ”中赤外フーリエ分光イメージングの実現可能性実証”, 日本工学会年年次学術講演会 Optics & Photonics Japan 2010 予稿集，pp.82-83(2010)

[42] Shun Sato, Wei Qi, Natsumi Kawashima, Kosuke Nogo, Satsuki Hosono, Akira Nishiyama, Kenji Wada, and Ichiro Ishimaru, “Ultra-miniature one-shot Fourier-spectroscopic tomography,” Optical Engineering, 55(2), 025106 (2016). doi:10.1117/1.OE.55.2.025106

[43] Yamamoto, N., Kawashima, N., Kitazaki, T., Mori, K., Kang, H., Nishiyama, A., Wada, K., Ishimaru, I.: Ultrasonic standing wave preparation of a liquid cell for glucose measurements in urine by midinfrared spectroscopy and potential application to smart toilets. J. Biomed. Opt. 23, 050503 (2018)

[44] 中村僖良ら（2001）『超音波』（日本音響学会編　音響工学講座⑧）コロナ社 pp. 14-15.

[45] 根岸勝雄，高木堅志郎（1984）『超音波技術』東京大学出版会，pp. 151-164.

[46] 山越芳樹，“小特集―力としての超音波―微小粒子への放射圧を利用した測定技術”，日本音響学会誌 52 巻 3 号，pp. 210-216 (1996).

[47] 山越芳樹，尾家康訓，“周期的に変化する超音波定在波中での微小粒子の運動軌跡観察による超音波放射音圧の測定法”，日本音響学会誌 52 巻 1 号，pp. 3-9 (1996).

[48] 山越芳樹，小林正樹，“超音波の移動定在波を用いた微小粒子の粒径計測”，日本音響学会誌 50 巻 3 号，pp. 198-204 (1994)

[49] T. Kitazaki, K. Mori, N. Yamamoto, C. Wang, N. Kawashima and I. Ishimaru, “Proposal of ultrasonic-assisted mid-infrared spectroscopy for incorporating into daily life like smart-toilet and non-invasive blood glucose sensor”, SPIE Proceedings (Optical Society of America, 2017), paper 1041204

[50] Natsumi KAWASHIMA, Tomoya KITAZAKI, Hiroyuki NOMURA, Akira NISHIYAMA, Kenji WADA, and Ichiro ISHIMARU, “Detection of Blood Glucose Level in Mice using Ultrasonic-assisted Mid-infrared Fourier Spectroscopy for

realizing Earring-type Non-invasive Blood Glucose Sensors", OSA Imaging and Applied Optics 2018, JM4A.2, 2018/06/25-28, USA

[51] H. Ullah, G. Gilanie, F. Hussain, E. Ahmad, "Autocorrelation optical coherence tomography for glucose quantification in blood", Laser Physics Letters, Vol. 12 (12), 125602, (2015).

[52] K. Larin, M. Motamedi, T. Ashitkov and R. Esenaliev, "Specificity of noninvasive blood glucose sensing using optical coherence tomography technique: a pilot study", Physics in Medicine and Biology, Vol. 48 (10), 1371, (2003).

[53] R. Esenaliev, K. Larin, I. Larina, and M. Motamedi, "Noninvasive monitoring of glucose concentration with optical coherence tomography", Optics Letters, Vol. 26 (13), 992, (2001).

[54] Y. C. Shen, et al., "The use of Fourier-transform infrared spectroscopy for the quantitative determination of glucose concentration in whole blood", Phys. Med. Biol., 48, pp. 2023-2032, 2003

[55] Ranjit Kumar Sahu, et al., "Continuous monitoring of WBC (biochemistry) in an adult leulemia patient using advanced FTIR-spectroscopy", Leukemia Research, vol. 30, issue 6, pp. 687-693, June 2006

[56] 田隅三生、"赤外分光測定法—基礎と最新手法　第 I 部基礎編　第 1 回 1.赤外吸収に関する基礎的事項"、分光研究、第 59 巻、第 1 号、2010 年

[57] 坂本章、"赤外分光測定法—基礎と最新手法　第 I 部基礎編　第 1 回 2.基本的な試料取扱法"、分光研究、第 59 巻、第 1 号、2010 年

[58] 落合周吉、"赤外分光測定法—基礎と最新手法　第 I 部基礎編　第 1 回 3.定量分析の基礎"、分光研究、第 59 巻、第 1 号、2010 年

[59] 増谷浩二、落合周吉、"赤外分光測定法—基礎と最新手法　第 I 部基礎編　第 3 回 5.FT-IR 分光計のハードとソフト"、分光研究、第 59 巻、第 3 号、2010 年

[60] 長谷川健，"スペクトル定量分析"，株式会社講談社サイエンティフィック（2005）

[61] Khalil, D., Sabry, Y., Omran, H., Medhat, M., Hafez, A., Saadany, B.: Characterization of MEMS FTIR spectrometer. In: Proc. SPIE 7930, MOEMS and Miniaturized Systems X, 79300J (2011)

[62] Ni, M., Feller, G., Irwin, J.W., Mason, J., Mudge, J.: High spectral resolution Fourier transform imaging spectroscopy in a Michelson interferometer with homodyne laser metrology control. In: Proc. SPIE 7457, Imaging Spectrometry XIV, Shen, S.S., Lewis, P.E. (eds), 74570L (2009)

[63] M. Servin, M. Cywiak, D. Malacara-Hernandez, J. C. Estrada, and J. A. Quiroga、"

Spatial carrier interferometry from M temporal phase shifted interferograms: Squeezing Interferometry” , Optics Express, vol. 16, issue 13, pp. 9276-0283, 2008

[64] J. H. Bruning, D. R. Herriott, J. E. Gallagher, D. P. Rosenfeld, A. D. White, and D. J. Brangaccio, “Digital Wavefront Measuring Interferometer for Testing Optical Surfaces and Lenses”, Applied Optics, vol. 13, issue 11, pp. 2693-2703, 1974

[65] Toshiki Yasokawa, Ichiro Ishimaru, et al., “A method for measuring the three-dimentional refractive-index distribution of single cells using proxomal two-beam optical tweezers and a phase-shifting mach-zehnder interferometer”, Optical Review, vol. 14, No. 4, pp. 161-164, 2007

[66] Barnes, T.H.: Photodiode array Fourier transform spectrometer with improved dynamic range. Appl. Opt. 24, 3702–3706 (1985)

[67] Padgett, M.J., Harvey, A.R.: A static Fourier-transform spectrometer based on Wollaston prisms. Rev. Sci. Instrum. 66, 2807–2811 (1995)

[68] Schardt, M., Murr, P.J., Rauscher, M.S., Tremmel, A.J., Wiesent, B.R., Koch, A.W.: Static Fourier transform infrared spectrometer. Opt. Express 24, 7767–7776 (2016)

[69] Köhler, M.H., Naßl, S.S., Kienle, P., Dong, X-c., Koch, A.W.: Broadband static Fourier transform midinfrared spectrometer. Appl. Opt. 58, 3393–3400 (2019)

[70] Köhler, M.H., et al.: Hyperspectral imager for the midinfrared spectral range using a single-mirror interferometer and a windowing method. OSA Continuum 2, 3212–3222 (2019)

[71] Ferrec, Y., Primot, J.: Spaceborne hyperspectral imaging with a static Fourier transform spectrometer. SPIE Newsroom (2013)

[72] M. Servin et al., “A novel technique for spatial phase-shifting interferometry,” J. Mod. Opt. 42, 1853 (1995).

[73] 佐藤貴則、富川望、陳軍、“ウォラストンプリズムを用いた小型共通光路位相シフト干渉顕微鏡”、Optics & Photonics Japan 2014, 6pP12, 2014 年 10 月

[74] Michael W. Kudenov and Eustace L. Dereniak, “Compact real-time birefringent imaging spectrometer”, Optics Express, Vol. 20, No. 16, July 2012

[75] S. Nakadate et al., “Real-time vibration measurement by a spatial phase-shifting technique with a tilted holographic interferogram”, Appl. Opt. 36, 281 (1997).

[76] S. Murata et al., “Spatial phase-shifting digital holography for three-dimensional particle tracking velocimetry,” Jpn. J. Appl. Phys. 48, 09LB01 (2009).

[77] Zhang, C, Bin, X., Zhao, B.: Static polarization interference imaging spectrometer (SPIIS). In: Proc. SPIE 4087, Applications of Photonic Technology 4, 957–961 (2000)

[78] Natsumi KAWASHIMA, Kosuke NOGO, Satsuki HOSONO, Akira NISHIYAMA,

Kenji WADA, Ichiro ISHIMARU, "Sensitivity improvement of one-shot Fourier spectroscopic imager for realization of noninvasive blood glucose sensors in smartphones", Opt. Eng., 55(11) 110506, November 2016

[79] Natsumi KAWASHIMA, Tomoya KITAZAKI, Kosuke NOGO, Akira NISHIYAMA, Kenji WADA, and Ichiro ISHIMARU, "Superimposing interferogram method using a multi-slit array to enhance sensitivity and interference definition of spatial-phase-shift interferometers", Optical Review, volume 27, issue 6, pages 530-541, October 2020

[80] Natsumi KAWASHIMA, Satoru ADACHI, Tomoya KITAZAKI, Hanyue KANG, Akira NISHIYAMA, Kenji WADA, and Ichiro ISHIMARU, "Ultra-miniature (diameter: 6mm, thickness: 5mm) low-cost (price:1,000 EUR) point-one-shot mid-infrared Fourier spectroscopic imager for ear clip type non-invasive blood glucose sensors", European Conferences on Biomedical Optics, Clinical and Preclinical Optical Diagnostics II, 110730H, July 2019

[81] Ross D. Shonat, et al., "Near-Simultaneous Hemoglobin Saturation and Oxygen Tension Maps in Mouse Brain Using an AOTF Microscope", Biophysical Journal, vol. 73, pp. 1223-1231, September 1997

[82] S. E. Harris and R. W. Wallace, "Acousto-optic tunable filter," J. Opt. Soc. Am. 59, 744–747 (1969).

[83] J. Katrašnik et al., "Spectral characterization and calibration of AOTF spectrometers and hyper-spectral imaging system," Chemometr. Intell. Lab. 101, 23–29 (2010).

[84] Shaw, G.A., Burke, H.K.: Spectral imaging for remote sensing. Lincoln Laboratory Journal 14, 3–28 (2003)

[85] Lu, G., Fei, B.: Medical hyperspectral imaging: a review. J. Biomed. Opt. 19, 10901 (2014)

[86] Willoughby, C.T., Folkman, M.A., Figueroa, M.A.: Application of hyperspectral-imaging spectrometer systems to industrial inspection. In: Three-Dimensional and Unconventional Imaging for Industrial Inspection and Metrology 2599, 264–272 (1996)

[87] J. Szlachetko et al., "Wavelength-dispersive spectrometer for X-ray microfluorescence analysis at the X-ray microscopy beamline ID21 (ESRF)," J. Synchrotron Radiat. 17, 400–408 (2010).

[88] Y. Yasuno et al., "One-shot-phase-shifting Fourier domain optical coherence tomography by reference wavefront tilting," Opt. Express 12, 6184, (2004).

[89] シグマ光機株式会社、"主な光の公式と関係式"

[90] https://www.global-optosigma.com/jp/category/opt_d/opt_d08.html

[91] Edmund Optics、“ビームエキスパンダー”

[92] https://www.edmundoptics.jp/knowledge-center/application-notes/lasers/beam-expanders/

[93] Smith, Warren J. Modern Optical Engineering. 3rd ed. New York, NY: McGraw-Hill Education, 2000.

[94] Wei Qi, Yo Suzuki, Shun Sato, Masaru Fujiwara, Natsumi Kawashima, Satoru Suzuki, Pradeep Abeygunawardhana, Kenji Wada, Akira Nishiyama, and Ichiro Ishimaru, “Enhanced interference-pattern visibility using multislit optical superposition method for imaging-type two-dimensional Fourier spectroscopy,” Applied Optics, Vol. 54, Issue 20, pp. 6254-6259, July 2015, doi: 10.1364/AO.54.006254

[95] Melissa C. Skala, et al. “Comparison of a physical model and principal component analysis for the diagnosis of epithelial neoplasias in vivo using diffuse reflectance spectroscopy”, Optics Express, vol. 15, no. 12, June 2007

[96] 堀内敏行，“光技術入門”，東京電機大学出版局 (2005)

[97] 松井吉哉，“収差論”，一般社団法人オプトメカトロニクス協会 (1989)

[98] 中村荘一, 藤江大二郎, “基礎からわかる光学部品”, オプトロニクス社 (2006)

[99] 牛山善太，“シッカリ学べる！光学設計の基礎知識”，日刊工業 (2017)

[100] エミール・ウォルフ，“光のコヒーレンスと偏光理論”，京都大学学術出版会
(2009)

[101] 牛山善太，“波動光学エンジニアリングの基礎”，オプトロニクス社 (2005)

[102] 河合滋，“光学設計のための基礎知識”，オプトロニクス社 (2006)

[103] 吉田正太郎，“反射望遠鏡光学入門”，誠文堂新光社 (2005)

[104] 桑嶋幹，“イチバンやさしい理工系「レンズ」のキホン”，Softbank Creative (2010)

[105] 河田聡，“超解像の光学”，学会出版センター (1999)

[106] 松井吉哉，“結像光学入門～光学系取扱いの基礎～”，一般社団法人日本オプトメカトロニクス協会 (1988)

[107] 中島洋，“Excel でできる光学設計～レーザー光学系の実用計算～”，アドコム・メディア株式会社 (2004)

Ethics of Animal Experimentation

In cultured cells, animal experiments, and clinical research, from the perspective of bioethics and safety measures, we carried out research appropriately in compliance with necessary procedures of “Rules of Animal Experiment in Kagawa University (香川大学動物実験規則)”, which is a rule of Kagawa University. I attended “Education and Training on Animal Experiment (動物実験に関する教育訓練)” in preparation to carry out animal experiments with small animals, such as mice. The protocol of this study was approved by the Animal Care and Use Committee for Kagawa University.

Acknowledgement

I extend my heartfelt thanks to a host of people without whose assistance the accomplishment of this thesis would have been impossible.

First and foremost, I am deeply indebted to my supervisor, Professor Ichiro Ishimaru, for his invaluable guidance and constant encouragement during my studies from undergraduate to doctorate level. I appreciate not only his advice on my research but also his great help from day to day.

I am also grateful to Professor Hideyuki Takao, Professor Kyohei Terao, Professor Akira Nishiyama, Professor Kenji Wada, and many instructors, whose valuable instruction has benefited me a great deal.

I received great help and fruitful advice from Professor Akira Nishiyama, Professor Kenji Wada and Mr. Yoshihide Fujisawa when performing animal experiments at Miki-cho Campus.

I sincerely appreciate coaching and cooperation in producing optical components from Mr. Hisao Higa, Ms. Chiemi Nakata, Ms. Satoko Shoji, Mr. Tetsuya Kondo, and Mr. Katsuyori Suzuki at the Nano-Micro Structure Device Integrated Research Center of Kagawa University.

I also extend my heartfelt thanks to many people at Technische Universität München. When I conducted research at the university during a period of 5 months, Professor Martin Buss and Professor Dirk Wollherr gave me invaluable mentorship and advice. Additionally, Mr. Stefan Friedrich and many friends gave me constant encouragement during my stay in Munich.

This research was supported by a Grant-in-Aid for Japan Society for the Promotion of Science Fellows (JSPS) (18J22468). I greatly appreciate this support from the JSPS.

I am grateful to all laboratory members. I could not have conducted this research without their kind help, fruitful advice, and encouragement.

Last but not least, I thank my parents and family; they have given me much encouragement and support during my 9 years of study at Kagawa University.